Title

Catalytic Active Site Structure for Soft Oxidant-Assisted Methane Coupling

Author

Filardi, Leah Rachel

Publication Date

2023

Peer reviewed|Thesis/dissertation

Catalytic Active Site Structure for Soft Oxidant-Assisted Methane Coupling

By

LEAH R. FILARDI
DISSERTATION

Submitted in partial satisfaction of the requirements for the degree of

DOCTOR OF PHILOSOPHY

in

Chemical Engineering

in the

OFFICE OF GRADUATE STUDIES

of the

UNIVERSITY OF CALIFORNIA

DAVIS

Approved:

Coleman X. Kronawitter, Co-Chair

Ron C. Runnebaum, Co-Chair

Ambarish Kulkarni

Committee in Charge

2023

TABLE OF CONTENTS

Abstract

Global climate change is a major motivation for the mitigation of greenhouse gas emissions. The most significant greenhouse gases contributing to US emissions, reported by the EPA, are carbon dioxide, methane, and nitrous oxide – all products of oil production and combustion. Catalytic co-conversion of these gases via CO_2- or N_2O-assisted methane coupling to high-value commodity chemicals, such as ethylene, has been demonstrated to be a highly selective process over some metal oxide catalysts. The research in this dissertation focused on identifying physical and electronic properties of selective metal oxide catalysts to develop structure-activity relationships between this class of catalysts and this class of oxidative coupling reactions.

To study this reaction system, a series of CaO/ZnO catalysts were developed as a platform to study the mechanistic cooperation of binary metal oxide catalyst systems. Calcium oxide, a highly basic metal oxide, was deposited on zinc oxide, a reducible oxide. CaO/ZnO binary metal oxide catalyst is comprised of cheaply abundant materials and has been demonstrated to be highly selective toward C_2 products during CO_2-assisted methane coupling (CO_2-OCM). A series of Ca/ZnO catalysts with varying Ca composition were characterized by microscopy (TEM), X-ray spectroscopies (L-edge XANES, XPS), and CO_2 adsorption infrared spectroscopy-temperature programmed desorption (IR-TPD). Catalysts with less than 2 mol% Ca contained highly disperse Ca sites that had lower Lewis basicity compared to bulk CaO. The CO_2-OCM performance of these catalysts with low-Ca-loading exhibited a strong dependence on Ca loading, where minor additions of Ca drastically increased C_2 product selectivity. These results coupled with further catalytic tests report the medium strength basicity of the interface between dispersed Ca and ZnO present in low-Ca-loading catalysts is optimal for C_2 product selectivity.

X-ray absorption spectroscopy (XAS) and complementary theoretical simulations characterized the extent of Ca dispersion in the low-Ca-loading Ca/ZnO catalysts. For catalysts with less than 2 mol% Ca, the Ca most probably exists as linear one-dimensional and planar two-dimensional CaO clusters roughly 7 to 26 Å in length. A pre-edge feature of the XANES spectra unique to the low-Ca-loading catalysts was

attributed to the presence of some under-coordinated Ca surface atoms by analysis of the local densities of states. The N_2O-OCM performance of these catalysts was evaluated. The presence of the CaO clusters and under-coordinated surface atoms corresponded to higher C_{2-4} product selectivities than over high-Ca-loading catalysts. These Ca sites are highly dispersed on ZnO, creating many selective Ca/ZnO interfacial sites, which can lead to enhanced methane coupling performance.

Additional experiments comparing kinetic and mechanistic information across various oxidants during methane coupling reveal a strong effect of oxidant partial pressure on reactivity. Co-feeding oxidants at varying partial pressures should be further explored as a route of optimizing product yields. To optimize this system for ethylene production, catalytic oxidant-assisted ethane dehydrogenation should also be further investigated. Preliminary results suggest that Ca/ZnO can effectively catalyze ethane dehydrogenation on the catalyst surface during CO_2-OCM. Various morphologies of ZnO were tested with Ca impregnation for their CO_2-OCM performance. Surface-area-normalized C_2 product yields did show preliminary morphology-dependence, where rod-like structures with a dominant (100) facet had poorer product yields than a commercial ZnO.

Acknowledgements

This dissertation is in thanks to those that have supported me on this journey:

Labmates, for making work both fun and easier with your help.

Advisors, for always believing in me and inspiring my sense of independence.

Friends, who inspire relentless joy and assurance that I'm never alone through a tough time.

Parents, for their endless love and support that serves as my daily motivation.

My partner, for your ability to bring peace to my chaos. You are my rock, you are my home.

Chapter 1. Introduction

Greenhouse gases are directly produced from oil production and combustion, where the largest impact comes from carbon dioxide, nitrous oxide, and methane.[1] During oil extraction in remote areas, the transport of natural gas becomes too costly, leading to methane combustion to CO_2 for release, where approximately 10% of the methane is not combusted and simply released to the atmosphere.[2] Since the shale gas revolution, methane, the majority species in both natural and shale gas, has become a widely used fuel and is now specifically sought after.[3] Its abundance has made methane a very cheap energy source, where its primary function is combustion to CO_2 for heat.[4] Developing technologies for on-site conversion of methane and other greenhouse gases into energy-dense, valuable products could reduce combustion and emissions as well as present an alternative cost- and environmentally-efficient route to commodity chemicals.

Oxidative methane coupling (OCM) has been widely studied as a potential avenue of methane upgrading to ethylene.[5–7] During OCM, one C-H bond of methane is heterolytically cleaved to create methyl radicals that can couple in the gas phase to form ethane, which can further dehydrogenate to ethylene.[8] However, sequential C-H bond breakage of methane or hydrocarbon products can lead to excessive oxidation and CO_x formation. Use of a less-oxidizing oxidant in place of O_2 that are also emitted greenhouse gases, like CO_2 and N_2O, can achieve much higher C_2 product selectivities while converting greenhouse gases into value-added products. The plentiful research of OCM can also be applied to the soft oxidant-assisted methane coupling reactions. Metal oxide-based catalysts have achieved the highest C_2 product yields[9] and are the most studied CO_2-OCM catalysts.[10,11] Optimal OCM performance is achieved over metal oxide catalysts that have medium-levels of reducibility[12] and basicity[13–15]. Similar effects have been observed for CO_2- and N_2O-assisted methane coupling.[16,17] Binary metal oxide catalysts that have basic metal oxide and reducible metal oxide components can achieve higher C_2 product selectivities than a single component.[18,19] The origin of this cooperative mechanism as well as potential active site structures were not well-understood. The work described in this dissertation focuses on characterizing a binary metal oxide

catalyst system to correlate potential active site structures to catalytic performance and gain fundamental knowledge of the mechanisms of the CO_2- and N_2O-assisted methane coupling reactions.

In Chapter 2, calcium-impregnated ZnO catalysts of varying compositions were investigated as CO_2-assisted methane coupling (CO_2-OCM) catalysts. Geometric and electronic properties of the calcium sites, as determined by electron microscopy, X-ray spectroscopies, and a newly established method of quantitative infrared spectroscopy–temperature programmed desorption (IR-TPD), explained later in further detail, were correlated to their catalytic performance. Catalysts with less than 2 mol% Ca exhibited unique physical properties that correlated to enhanced catalytic properties compared to bulk CaO or Ca/ZnO catalysts with a high concentration of Ca. The thorough characterization aims to aid future catalyst design principles for methane coupling.

Chapter 3 further studies the Ca site structure in Ca/ZnO catalysts with experimental and theoretical X-ray absorption spectroscopy to determine a more precise degree of Ca dispersion in the low-Ca-loading catalysts. Ca was found to exist as one- or two-dimensional CaO clusters 7 to 26 Å in length on the ZnO surface for catalysts with less than 2 mol% Ca. The catalytic activity of these Ca/ZnO catalysts was evaluated for N_2O-assisted methane coupling (N_2O-OCM). Similar conclusions were found to those in Chapter 2, where the CaO cluster catalysts exhibited higher C_2 product selectivity than those with large CaO nanoparticles.

Chapter 4 reports results of additional experiments that compliment those in Chapters 2 and 3 but did not fit within the scope of these chapters. The results include catalytic evaluation of Ca/ZnO and similar materials varying reaction parameters of N_2O-OCM, CO_2-OCM, and OCM to understand their impact on reaction kinetics and product distribution. The results may serve to identify areas of interest for future experimental exploration.

Method Development

Unique challenges to characterize the low-Ca-loading catalysts arose during the development of Chapter 2. The quantity of CO_2 adsorbed on ~20 mg of catalyst during the temperature-programmed desorption of

CO_2 was too low for desorption to be detected by thermogravimetric analysis and mass spectrometry (TGA-MS), preventing characterization of the basic sites. With diffuse reflectance infrared Fourier transform spectroscopy (DRIFTS), the formation of surface calcium carbonate by CO_2 adsorption could be selectively observed and quantified. *Operando* DRIFTS enabled the study of CO_2 desorption profiles.

The experimental method was adapted from similar methods of CO adsorption and desorption[20] and is described in more detail in Chapter 2. Briefly, ~15 mg of catalyst was treated *in situ* in air to 850 °C to ensure full desorption of any water and carbonate species that formed during air-exposure. While cooling from 850 °C in inert gas, spectra of the catalyst with no adsorbates were collected. CO_2 was introduced to the catalyst at room temperature to adsorb. After, all gaseous CO_2 was removed from the cell and gas lines, and the sample cell was heated in inert gas at a fixed rate collecting spectra at designated temperatures during the ramp to build the TPD profile.

All spectra were collected and plotted as log(1/R). The relative intensity of the region of interest after versus before CO_2 adsorption is significantly greater than 0.6, a threshold where the Kubelka-Munk function is no longer linearly proportional to absorbance and log(1/R) is a better approximation.[21] Spectra of the bare catalyst surface taken during the cooling step were subtracted from the spectra taken during the CO_2 TPD temperature ramp, each at the corresponding temperature. The spectra of the bare catalyst serve as background spectra to eliminate changes in the background due to temperature and thermal radiation. Concentration is directly proportional to absorbance, according to Beer's Law. Integrating the total carbonate absorbance signal at each temperature measured provides a relative concentration of CO_2 on the surface. The relationship between carbonate area and temperature will closely fit a sigmoidal decay, as desorption occurs and coverage approaches 0. The inflection point of the curve is the temperature where the maximum rate of CO_2 desorption occurs. This temperature can be used as a metric for catalyst basicity, where the temperature of the maximum rate of desorption over a more strongly basic catalyst would be higher. The IR-TPD technique is a surface-sensitive method that allows for quantitative analysis of adsorption and desorption profiles in dilute catalysts.

References

(1) US EPA. Overview of Greenhouse Gases. https://www.epa.gov/ghgemissions/overview-greenhouse-gases (accessed 2023-09-17).

(2) Plant, G.; Kort, E. A.; Brandt, A. R.; Chen, Y.; Fordice, G.; Gorchov Negron, A. M.; Schwietzke, S.; Smith, M.; Zavala-Araiza, D. Inefficient and Unlit Natural Gas Flares Both Emit Large Quantities of Methane. Science (1979) 2022, 377 (6614), 1566–1571.

(3) Wang, Q.; Chen, X.; Jha, A. N.; Rogers, H. Natural Gas from Shale Formation – The Evolution, Evidences and Challenges of Shale Gas Revolution in United States. Renewable and Sustainable Energy Reviews 2014, 30, 1–28.

(4) US Energy Information Administration (EIA). Use of natural gas. https://www.eia.gov/energyexplained/natural-gas/use-of-natural-gas.php (accessed 2023-09-17).

(5) Lunsford, J. H. The Catalytic Oxidative Coupling of Methane. Angewandte Chemie International Edition 1995, 34 (9), 970–980.

(6) Ortiz-Bravo, C. A.; Chagas, C. A.; Toniolo, F. S. Oxidative Coupling of Methane (OCM): An Overview of the Challenges and Opportunities for Developing New Technologies. J Nat Gas Sci Eng 2021, 96, 104254.

(7) Hutchings, G. J.; Scurrell, M. S.; Woodhouse, J. R. Oxidative Coupling of Methane Using Oxide Catalysts. Chem. Soc. Rev. 1989, 18, 251–283.

(8) Driscoll, D. J.; Mártir, W.; Wang, J.-X.; Lunsford, J. H. Formation of Gas-Phase Methyl Radicals over MgO. J. Am. Chem. Soc 1985, 107, 58–63.

(9) Asami, K.; Fujita, T.; Kusakabe, K.-I.; Nishiyama, Y.; Ohtsuka, Y. Conversion of Methane with Carbon Dioxide into C_2 Hydrocarbons over Metal Oxides. Appl. Catal. A: General 1995, 126 (2), 245–255.

(10) Cai, X.; Hu, Y. H. Advances in Catalytic Conversion of Methane and Carbon Dioxide to Highly Valuable Products. Energy Sci. Eng. 2019, 7 (1), 4–29.

(11) He, Y.; Yang, B.; Cheng, G. On the Oxidative Coupling of Methane with Carbon Dioxide over CeO_2/ZnO Nanocatalysts. Catal. Today 2004, 98 (4), 595–600.

(12) Kumar, G.; Lau, S. L. J.; Krcha, M. D.; Janik, M. J. Correlation of Methane Activation and Oxide Catalyst Reducibility and Its Implications for Oxidative Coupling. ACS Catal. 2016, 6 (3), 1812–1821.

(13) Wang, H.; Schmack, R.; Sokolov, S.; Kondratenko, E. V.; Mazheika, A.; Kraehnert, R. Oxide-Supported Carbonates Reveal a Unique Descriptor for Catalytic Performance in the Oxidative Coupling of Methane (OCM). ACS Catal. 2022, 12, 9325–9338.

(14) Zhang, Z.; Gong, Y.; Xu, J.; Zhang, Y.; Xiao, Q.; Xi, R.; Xu, X.; Fang, X.; Wang, X. Dissecting $La_2Ce_2O_7$ Catalyst to Unravel the Origin of the Surface Active Sites Devoting to Its Performance for Oxidative Coupling of Methane (OCM). Catal. Today 2021, 400–401, 73–82.

(15) Siakavelas, G. I.; Charisiou, N. D.; AlKhoori, A.; Gaber, S.; Sebastian, V.; Hinder, S. J.; Baker, M. A.; Yentekakis, I. V.; Polychronopoulou, K.; Goula, M. A. Oxidative Coupling of Methane on Li/CeO_2 Based Catalysts: Investigation of the Effect of Mg- and La-Doping of the CeO_2 Support. Mol. Catal. 2022, 520, 112157.

(16) Filardi, L. R.; Yang, F.; Guo, J.; Kronawitter, C. X.; Runnebaum, R. C. Surface Basicity Controls C–C Coupling Rates during Carbon Dioxide-Assisted Methane Coupling over Bifunctional Ca/ZnO Catalysts. Physical Chemistry Chemical Physics 2023, 25 (14), 9859–9867.

(17) Ferreira, A. C.; Gasche, T. A.; Leal, J. P.; Branco, J. B. Methane Activation with Nitrous Oxide over Bimetallic Oxide Ca-Lanthanide Nanocatalysts. Molecular Catalysis 2017, 443, 155–164.

(18) Wang, Y.; Ohtsuka, Y. CaO-ZnO Catalyst for Selective Conversion of Methane to C_2 Hydrocarbons Using Carbon Dioxide as the Oxidant. J. Catal. 2000, 192 (1), 252–255.

(19) Chen, C.; Xu, Y.; Li, G.; Guo, X. Oxidative Coupling of Methane by Carbon Dioxide: A Highly C_2 Selective La_2O_3/ZnO Catalyst. Catal. Lett. 1996, 42 (3–4), 149–153.

(20) Thang, H. V.; Pacchioni, G.; DeRita, L.; Christopher, P. Nature of Stable Single Atom Pt Catalysts Dispersed on Anatase TiO_2. J. Catal. 2018, 367, 104–114.

(21) Sirita, J.; Phanichphant, S.; Meunier, F. C. Quantitative Analysis of Adsorbate Concentrations by Diffuse Reflectance FT-IR. Anal Chem 2007, 79 (10), 3912–3918.

Chapter 2. Surface Basicity Controls C–C Coupling Rates during Carbon Dioxide-Assisted Methane Coupling over Bifunctional Ca/ZnO Catalysts

Adapted from publication in *Physical Chemistry Chemical Physics* with permission:

L. R. Filardi, F. Yang, J. Guo, C. X. Kronawitter, R. C. Runnebaum**,** *Phys. Chem. Chem. Phys.*, 2023, 25, 9859-9867. DOI: 10.1039/D3CP00332A

2.1 Abstract

Carbon dioxide-assisted coupling of methane offers an approach to chemically upgrade two greenhouse gases and components of natural gas to produce ethylene and syngas. Prior research on this reaction has concentrated efforts on catalyst discovery, which has indicated that composites comprised of both reducible and basic oxides are especially promising. There is a need for detailed characterization of these bifunctional oxide systems to provide a more fundamental understanding of the active sites and their roles in the reaction. We studied the dependence of physical and electronic properties of Ca-modified ZnO materials on Ca content *via* X-ray photoelectron and absorption spectroscopies, electron microscopy, and infrared spectroscopic temperature-programmed desorption (IRTPD). It was found that introduction of only 0.6 mol% Ca onto a ZnO surface is necessary to induce significant improvement in the catalytic production of C_2 species: C_2 selectivity increases from 5% on unmodified ZnO to 58%, at similar conversions. Evidence presented shows that this selectivity increase results from the formation of an interface between the basic CaO and reducible ZnO phases. The basicity of these interface sites correlates directly with catalytic activity over a wide composition range, and this relationship indicates that moderate CO_2 adsorption strength is optimal for CH_4 coupling. These results demonstrate, for the first time to our knowledge, a volcano-type relationship between CO_2-assisted CH_4 coupling activity and catalyst surface basicity, which can inform further catalyst development.

2.2 Introduction

Methane is the dominant constituent of natural gas, biogas, and shale gas, and due to advances in extraction and production technologies, it is an abundant resource.[1] However, the lack of technology to chemically utilize this resource efficiently leads to the practice of methane flaring and, thus, greenhouse gas emissions. There is a resurgent interest in pursuing the oxidative coupling of methane (OCM) as a viable avenue for methane upgrading into larger hydrocarbons.[2] However, when O_2 is used as an oxidant, product selectivity is hindered by overoxidation of methane and C_2 products to CO_x, which limits overall C_2 yield.[3] It has been demonstrated that carbon dioxide is an effective soft oxidant, facilitating the conversion of primary greenhouse gases into both valuable C_2 products and syngas.[4,5]

In 1988, carbon dioxide was first introduced during oxidative coupling of methane with oxygen.[6] A promotional effect of CO_2 on C_2 yield, as well as the formation of C_2 products from reaction of methane and CO_2 in the absence of O_2 was observed. Since then, it has been shown for many metal oxide catalyst systems[7] that the presence of CO_2 alone in methane reactor feeds (that is, in the absence of O_2) facilitates C–C coupling (CO_2-assisted oxidative methane coupling or CO_2-OCM). Enhanced activity and selectivity have been demonstrated with binary metal oxide composites, specifically those comprised of a basic oxide and a reducible oxide, including CaO/CeO_2,[8] Sr/MnO,[9] and Ca/CrO_2.[10] It is proposed that the basic oxide promotes CO_2 adsorption, which undergoes dissociation at a site associated with the reducible oxide to form an active surface oxygen species.[11] This species can facilitate methane activation to generate methyl radicals, which are known to couple in the gas phase to form ethane and ethylene.[12]

The synergy between basic and reducible oxides was demonstrated by Wang and Ohtsuka using CaO/ZnO.[13] Pure CaO catalyzes CO_2-OCM with moderate selectivity but very low yield, while pure ZnO preferentially forms syngas *via* methane reforming. When compared to the pure oxide components, the composite materials yield enhanced activity and selectivity, reaching 80% selectivity to C_2 products. However, it was shown that varying Ca composition from 10 to 50 mol% results in very similar catalyst performances, implying there is little change in the active site structure over this wide composition range.[13]

The absence of significant influence of composition on catalyst performance has been reported for several other binary oxides containing either CaO[10,14] or ZnO.[11,15] For CO_2-OCM, there has been a dominant focus on catalyst discovery, which has precluded a much-needed detailed investigation of these promising bifunctional oxide systems. Thus, a fundamental understanding of the active sites and their roles in the reaction is lacking.

In the present work, we combine a suite of complementary characterization techniques, including most notably infrared spectroscopic temperature programmed desorption (IR-TPD), to understand the composition dependence of properties of a model binary Ca/ZnO catalyst at Ca levels much lower than those previously reported. Studying catalysts with very low concentrations of the basic oxide reveals information on the formation of the sites responsible for the promoted coupling activity. We herein demonstrate that the interface sites between the two metal oxides are critical to methane activation and selective coupling, which is attributable to their optimal moderate basicity. We use the notation Ca/ZnO to refer to Ca-surface-loaded ZnO catalyst samples, but surface Ca–O species are described as oxides for convenience, since Ca is oxidized in all conditions examined.

2.3 Experimental Methods

Catalyst synthesis

Ca/ZnO catalysts were prepared *via* a wet impregnation synthesis published previously by Wang and Ohtsuka.[13] The calculated amount of calcium nitrate tetrahydrate (99% ACS Reagent, MP Biomedicals) to provide the desired Ca/(Ca + Zn) composition (indicated as mol% in this chapter) was dissolved in MilliQ (18 Mohm) water (5 mL g^{-1} ZnO). Zinc oxide (99.9% metal basis, Alfa Aesar) was added, and the resulting slurry was sonicated to maximize ZnO dispersion in the solution. The mixture was partially covered and stirred at room temperature overnight until the water evaporated. The resulting white solids were then dried in an oven at 120 °C for 24 hours before calcining in 50 mL min^{-1} air (zero air, Praxair) at 850 °C (ramp 5 °C min^{-1}) for 4 h. Calcium oxide was synthesized by heating 100 mL of a 0.25 M calcium nitrate solution in an oil bath to 80 °C.[16] Under vigorous stirring, a 50 mL solution of 1 M NaOH was added dropwise,

resulting in a cloudy solution of white precipitate. The solids were vacuum filtered, washed with MilliQ water, and dried overnight at 120 °C before calcination (see above).

Catalytic activity measurements

CO_2-OCM was conducted in a quartz down-flow, packed-bed reactor with 4 mm ID. A sample mass of 100 mg was loaded into the tube, supported by quartz wool (Acros Organics). The reactor was heated in a tubular furnace at 8 °C min^{-1} to 850 °C under 13.3 mL min^{-1} nitrogen (99.999%, Praxair). Flow was then switched to bypass the reactor and adjusted to 3.3 mL min^{-1} methane (≥ 99.999%, Airgas), 6.7 mL min^{-1} carbon dioxide (pure clean grade, Airgas), and 3.3 mL min^{-1} nitrogen prior to flow through the reactor. Reaction products were measured by an online Agilent 7890A gas chromatograph (GC) with a FID and TCD. Empty reactors were used to determine conversion in the absence of catalyst prior to each experiment. This conversion was subtracted from the catalysis results. Relevant reaction parameters are defined as follows:

$$C_2\ Selectivity\ \% = \frac{2\dot{n}_{C_2H_x}}{\dot{n}_{C,prod}} \times 100\%$$

$$Conversion\ \% = \frac{2\dot{n}_{C_2H_x} + \dot{n}_{CO,reform}}{\dot{n}_{i,react}} \times 100\%$$

where $\dot{n}_{C_2H_x}$ is the molar flowrate of C_2 products, $\dot{n}_{C,prod}$ is the molar flowrate of all carbon atoms in products, $\dot{n}_{i,react}$ is the initial molar flowrate of the reactant of interest, and $\dot{n}_{CO,reform}$ is the molar flowrate of CO originating from CH_4 in the reforming of CH_4, calculated by[7]

$$\frac{-\dot{n}_{C_2H_6} - \dot{n}_{C_2H_4} + \dot{n}_{H_2} + \dot{n}_{CO}}{4}$$

C_2 yield is defined as the total molar flowrate of ethane and ethylene as measured by GC.

Materials characterization

Calcium loading was quantified by inductively coupled plasma mass spectrometry (ICP-MS) after acid digestion with an Agilent quadrupole mass spectrometer 7500. Nitrogen physisorption isotherms were measured using a Micromeritics 3Flex physisorption/chemisorption instrument. Physisorption measurements were made at -196 °C. Samples were degassed at 300 °C for 3 hours under vacuum prior to

analysis. Surface areas were determined by the BET method. Scanning electron microscopy (SEM) was performed on a Thermo Fisher Scientific Quattro ESEM. Samples were pressed onto carbon tape on a sample stub. Images were acquired under vacuum using a spot size of 3 and an accelerating voltage of 5 kV. X-ray diffraction (XRD) patterns were recorded on a Bruker D8 Advanced Diffractometer with Cu Kα radiation. Powder samples were sieved through a 304 stainless steel wire cloth disc with a mesh size of 200 to ensure a random distribution of exposed facets. They were adhered to silica sample holders with Dow Corning high vacuum grease. For scanning transmission electron microscopy (STEM) analysis by a JEOL-JEM 2500SE electron microscope, dilute suspensions of samples were drop-cast on copper-supported lacey carbon grids and dried overnight. Energy dispersive X-ray spectroscopy (EDS) was performed using a Thermo Corporation EDS spectrometer attached to the JEOL JEM 2500SE. X-ray photoelectron spectroscopy (XPS) was performed using a Kratos AXIS Supra spectrometer equipped with a monochromatic Al Kα anode (1486.6 eV).16 Air-exposed powder samples were adhered to carbon tape and loaded into a flexi-lock. The flexi-lock was pumped down to 10^{-7} torr before transfer of the samples to the analysis chamber. Binding energies were charge-corrected by aligning the Zn $2p_{3/2}$ peak to 1021.9 eV.[17] The data were processed and analyzed using Kratos ESCApe software. Synchrotron X-ray absorption spectroscopy (XAS) experiments of the Ca and Zn L-edge regions were conducted at beamline 7.3.1 of the Advanced Light Source (ALS), Lawrence Berkeley National Laboratory. Spectra of total electron yield (TEY) were collected and charge-corrected by referencing a standard of the metal oxide to known values.[18,19] Diffuse reflectance infrared Fourier transform spectroscopy (DRIFTS) was performed with a Bruker Tensor II FTIR Spectrometer equipped with a Pike Technologies DiffusIR MidIR Accessory. Spectra were collected with 128 scans at a resolution of 2 cm^{-1}. *In situ* calcinations were performed by heating the sample 10 °C min^{-1} to 850 °C for 30 minutes under 20 mL min^{-1} of dry air flow. Background spectra were collected at each temperature of interest under N_2 flow during the cooling ramp following the calcination. The cell was held at the target temperature for 5 minutes prior to collecting the background spectra. At room temperature (below 30 °C), CO_2 was introduced by flowing 2.5 mL min^{-1} of CO_2 with 47.5 mL min^{-1} of N_2 for 1 minute. Carbon dioxide was purged from the cell by cycling the cell between

vacuum and N_2 refill 3 times followed by 20 mL min^{-1} N_2 flow for 1 hour. Temperature-programmed carbonate desorption was measured by heating the sample 1 °C min^{-1} to 800 °C under 20 mL min^{-1} of dry air flow and collecting spectra every 50 °C.

2.4 Results and Discussion

Catalysis results

Ca/ZnO catalysts with various Ca surface loadings were synthesized *via* wet impregnation and evaluated for their CO_2-OCM performance (Fig. 2.1). At low loadings, introduction of Ca onto the ZnO surface drastically shifts the product distribution from syngas to C_2 hydrocarbon products. Increasing Ca loading increases C_2 selectivities until a maximum of 70.6% is reached. Most notably, increasing the Ca loading from 0.4 mol% to 0.6 mol% results in a 4-fold increase in C_2 selectivity and a 2- fold increase in the yield. Additions of Ca beyond 0.6% do not further improve the methane coupling yield, and at the highest loadings examined, addition of Ca decreases yields. Consistent with previous studies, pure ZnO preferentially generates syngas via methane dry reforming,[20] while pure CaO has little activity to both syngas and C_2 products. The low CaO activity has been attributed to low concentrations of defect sites,[21] which are understood to be essential to activation of methane. Ethane production is nearly double that of ethylene over all catalysts (Table S2.1 provides the measured product compositions for CO_2-OCM with all catalysts). While these results are consistent with early reports of enhanced coupling performance for binary metal oxides,[13] the impact of small amounts of added Ca (< 1 mol%) in these experiments highlights its role in promoting CO_2 adsorption during reaction.

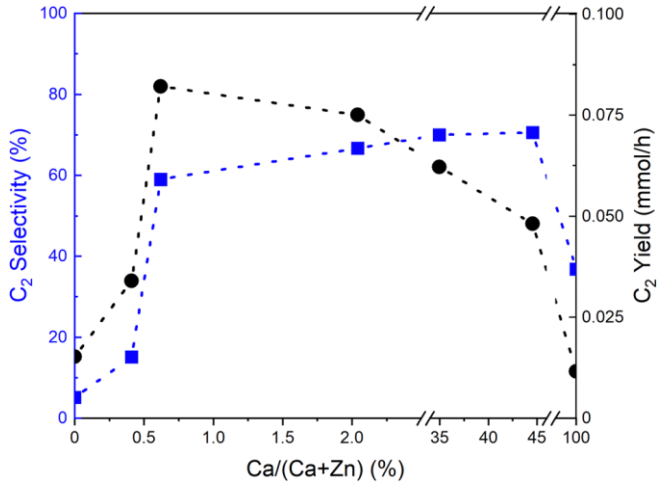

Figure 2.1 Effects of Ca loading on C_2 selectivity (■) and C_2 yield (●). Reaction conditions: 850 °C; 100 mg catalyst; 13.3 mL min^{-1} total gas flow rate with P_{CH_4} = 0.25 atm, P_{CO_2} = 0.5 atm, P_{N_2} = 0.25 atm; 4 h on stream. Methane conversion was less than 7% (Table S2.1). All Ca loadings are reported in molar concentration of metal cations, as determined by ICP-MS (Table S2.2). Lines are included to guide the eye.

Motivated by work demonstrating a bifunctional mechanism for composite catalysts,[8–10] catalysis experiments with physical mixtures of pure CaO with ZnO were performed to investigate the role of the interface between Ca (or CaO) and ZnO in CH_4 coupling. Experiments in which the CaO was physically separated from ZnO by quartz wool, shown in Fig. 2.2, yield a product distribution almost identical to that from pure ZnO. This is consistent with the relative inactivity of pure CaO for CO_2-OCM catalysis. Physically mixing CaO with ZnO favors CH_4 reforming at short times-on-stream, but C–C coupling activity increases with longer times-on-stream. This outcome could be due to the sintering of the two oxides under the reaction temperature of 850 °C to form the relevant Ca/ZnO interface. To explore this hypothesis further, a mixture of the two oxides were calcined in air at 850 °C before being loaded into the reactor; this configuration yielded results nearly identical to those from the non-calcined mixture. This result indicates that the active sites for selective CH_4 coupling are not formed by temperature-induced sintering in a highly oxidative environment (here, pure O_2 at elevated temperature). Therefore, the more reductive environment of the reaction mixture is likely the primary origin of modifications to catalyst surfaces with time on stream. Zinc oxide is known to easily form local oxygen vacancies under reducing conditions at high temperatures.[22–25] Under significantly reducing conditions, pure ZnO may also become partially reduced

with metallic domains that can vaporize at reaction temperature, leading to some restructuring of the catalyst surface.[26] It is unlikely that CaO would also be reduced to any significant degree in these conditions. However, the CO_2 and water present under reaction conditions could promote CaO sintering.[27] Thus, the increased C_2 yield with longer time on stream is likely due to further interface formation, associated with oxygen vacancy generation as well as CaO sintering. Vacancies on ZnO are capable of dissociating CO_2,[28] and we propose in this report that those exposed to adsorbed CO_2 at neighboring Ca-containing sites are active for this reaction. The drastic differences in yields in reactor studies between Ca impregnation onto ZnO and physical mixtures of the constituent oxides suggest that the Ca–ZnO interface is critical for coupling to occur. The catalysts were further characterized to explain the trends in activity with Ca loading and to understand the role of the interface.

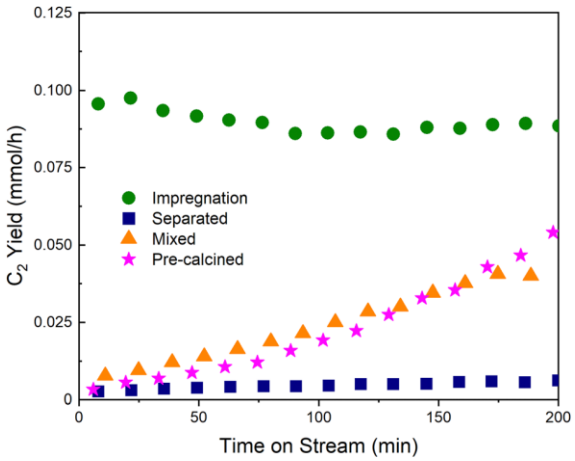

Figure 2.2 Contrasting C_2 product yields associated with various methods of loading 0.6% Ca + ZnO into reactor on C_2 yield. Impregnation: ZnO impregnated with Ca salt (●); mixed: well-mixed physical mixture of CaO and ZnO (▲); pre-calcined: physical mixture of CaO and ZnO that was calcined to 850 °C in air prior to reaction (★); separated: loading that isolates upstream CaO from downstream ZnO with quartz wool (■). Reaction conditions: 850 °C; WHSV = 8.0 L h^{-1} g_{cat}^{-1} with P_{CH_4} = 0.25 atm, P_{CO_2} = 0.5 atm, P_{N_2} = 0.25 atm

Catalyst characterization

BET measurements (Table S2.2) reveal that pure CaO has ~14 times higher surface area than pure ZnO. Surface areas of all Ca/ZnO samples are similar to those of pure ZnO. SEM images (Fig. S2.1) indicate that

there were no changes in ZnO bulk structure or morphology with increasing Ca concentration. Therefore, differences in activity are not correlated to surface area or morphology.

X-ray diffractograms, shown in Fig. 2.3a, reveal only the hexagonal ZnO phase (JCPDS 36-1451) and lack observable peaks corresponding to Ca species in samples with 0.6% Ca or less. No calcium zincate or complex oxide phase was observed. Within the resolution of our measurements, there is no indication in the diffractograms of modification to the ZnO lattice parameters. Increasing Ca concentration above 0.6% yields distinct bulk CaO phases. The sample with 2% Ca is characterized by minor peaks at 32.2°, 37.4°, and 53.9° (Fig. S2.2), which are the dominant diffraction peaks for CaO. Long-range ordered CaO phases are only observed in samples with 2% and higher Ca content. The STEM image and EDX maps of the 35% Ca/ZnO sample in Fig. 2.3b–e show the existence of large CaO crystallites with length dimensions of hundreds of nanometers on the surface of ZnO particles. By contrast, STEM images of the 0.6% Ca/ZnO sample do not show any visible CaO clusters (Fig. S2.3). Lack of visible Ca species in these images is due to the low Z-contrast and high dispersion of Ca species at low loadings.

X-ray photoelectron spectra (XPS) of the Ca 2p region are shown in Fig. 2.3f. To account for binding energy changes due to charging, the energy scale was corrected using the Zn 2p peaks (Fig. S2.4c) from the support; Ca loading is unlikely to modify the electronic structure of the support over the ~10 nm probe depth of photoelectrons. The validity of this correction is confirmed by the consistency of the C 1s peak, which is commonly used for energy calibration (Fig. S2.4d). The lack of influence of Ca on ZnO electronic structure is also confirmed for the high Ca-loading samples by Zn L_{23}-edge XANES (Fig. S2.5). For these high Ca-loading samples, the Ca $2p_{3/2}$ and $2p_{1/2}$ peaks are observed at 347.6 and 351.2 eV, respectively.[17] The peaks shift to 348.0 and 351.6 eV for all samples with $\leq$ 2% Ca. The similar peak binding energies in the low-loading samples suggest that they contain similar Ca sites that are distinctly different from those in the high Ca-loading samples. The shift to higher binding energy for the low Ca-loading samples is consistent with support effects observed for supported metal oxide nanoparticles.[29,30] As CaO particle size grows, the Ca 2p binding energy approaches that of bulk CaO. Quantification of the fitted XPS peaks yields Ca concentrations well above the bulk concentrations as determined by ICP-MS (Table S2.2).

Given the surface sensitivity of XPS, it is clear that the Ca species are segregated at the surface of the ZnO particles, as illustrated by EDX mapping, rather than doped within the ZnO lattice. This is confirmed by the decrease in Ca intensity and corresponding increase in Zn intensity after argon etching the catalyst surface (Fig. S2.6).

A trend across compositions is also observed in XANES spectra at the Ca L-edge, which is sensitive to the oxidation states and local environments of metals.[31] In these spectra, the peaks correspond to transitions from Ca 2p to primarily unoccupied Ca d states. Peaks in data from the low Ca-loading samples are shifted to a higher energy compared to those in the high Ca-loading samples (Fig. 2.3g), which is consistent with the XPS results. Taken together, the results from these characterization methods all support the conclusion that the Ca sites present in low concentrations are similar to each other, but distinct from those present in high concentrations, which is associated with large CaO crystallites.

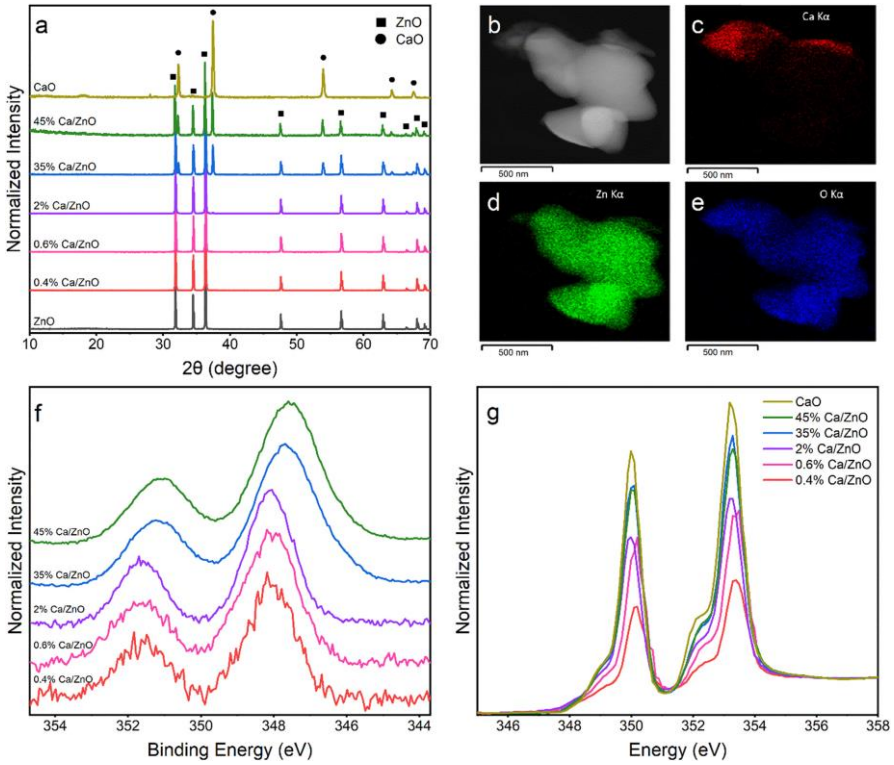

Figure 2.3 Physical and electronic characterization of the Ca/ZnO materials: (a) XRD patterns of calcined pure metal oxides and binary metal oxides with varied concentrations. (b) HAADF-STEM image of 35% Ca/ZnO, (c–e) EDX elemental mapping of Ca, Zn, and O, respectively. (f) XPS and (g) XANES spectra of Ca 2p region, which shows shifts to higher binding energies at lower Ca levels.

The lack of long-range-ordered CaO phases in low-loading samples suggests the presence of a more dispersed state of Ca ions, and therefore a relative increase in the amount of interface sites containing Ca–O–Zn interactions. Fig. 2.2 illustrates the importance of the interface sites in CH_4 coupling, which we propose to be the most active sites for CO_2 and CH_4 dissociation. The effectiveness of each Ca atom in producing C_2 products is constant over low Ca concentrations (Fig. S2.7), which suggests that the active site does not change with incremental addition of small amounts of Ca. The Ca-normalized C_2 product yield drastically declines from 167 to 75 mmol h^{-1} gCa^{-1} as loading is increased to 2% Ca, a state in which the CaO bulk phase forms. It further decreases to 0.23 mmol h^{-1} gCa^{-1} for pure CaO. Therefore, the sharp increase in C_2 selectivity and yield with a very small increase in Ca concentration in Fig. 2.1 can be explained by an increase in the number of Ca atoms in close contact with the ZnO surface, creating interfacial active sites. The synergy between oxygen vacancy concentration and active site dispersion was reported to control oxygen abstraction rates in a mixed metal oxide catalyst,[32] emphasizing the role of interfaces in catalyst reactivity. We propose a similar mechanism of cooperation between oxygen vacancies and Ca-containing surface species. Thus, as Ca loading increases and dispersion decreases, C_2 product yield also decreases. The reaction data also suggest that Ca addition increasingly blocks or to some extent modifies ZnO sites responsible for methane reforming. Oxygen vacancies formed from reducible metal oxides can facilitate methane reforming.[33,34] However, neighboring Ca atoms may modify the structure and activity of these sites. Thus, the dominant reaction pathway transitions from CH_4 reforming on the bare ZnO surface to coupling at the interfacial sites when surface Ca is introduced. Further addition of Ca leads to further enhancement of CH_4 coupling over reforming. The selective formation of ethylene *via* CO_2-OCM instead of CO *via* CH_4 dry reforming is highly dependent on whether CH_x species remain bound too strongly on the surface and undergo subsequent hydrogen abstraction.[35] More reducible catalyst surfaces adsorb CH_x species more strongly.[36] This explains the preferences for CH_4 dry reforming over ZnO catalysts. Loading another oxide onto the surface can suppress CH_4 reforming by decreasing the overall reducibility at the interface.[37]

To better understand the interaction of CO_2 with these material surfaces, CO_2 adsorption was studied with *in situ* DRIFTS experiments. After exposure to CO_2 at room temperature, prominent peaks are present around 1390–1560 cm^{-1}, 1630 cm^{-1}, 1772 cm^{-1}, and 2540 cm^{-1}, corresponding to unidentate carbonate, bicarbonate, bridging carbonate, and linearly adsorbed CO_2 (Fig. 2.4), respectively.[38,39] Consistent peak positions are present in all Ca-containing samples and differ from those from CO_2 adsorption on pure ZnO (Fig. S2.8). Even with low concentrations of Ca present, CO_2-surface interactions are limited to Ca-containing sites. Zinc oxide is known to poorly adsorb CO_2;[40] carbonate formation on ZnO is considered negligible. Unidentate carbonate is the most preferable mode of carbonate in all measured Ca-containing samples. The formation of bridging carbonates, shown in the insets of Fig. 2.4, requires at least two adjacent Ca atoms, and therefore the intensity of these peaks relates to the lack of Ca dispersion. Its presence in high Ca-loading samples with large CaO clusters is unsurprising. Bridging carbonate peaks are also present in the 0.4% Ca/ZnO, but with much lower intensity relative to the total carbonate concentration. This evidence supports the conclusion that most of the Ca-containing species are highly dispersed, likely existing as a mixture of mononuclear sites and nano-sized clusters. However, it is not possible to accurately identify either of these species without a measurement that is extremely sensitive to the location coordination environment of Ca, such as extended X-ray absorption fine structure (EXAFS).

After adsorption, the temperature-programmed desorption of the carbonate species in inert nitrogen atmosphere reveals that the catalysts with 2% or lower Ca content desorb carbonate at very low temperatures (less than 200 °C). The data also show that carbonate is stable on the higher-Ca-loading samples up to 400 °C (Fig. S2.9a); the carbonate stability on samples with CaO particles is consistent with the behavior of pure CaO.[38,41]

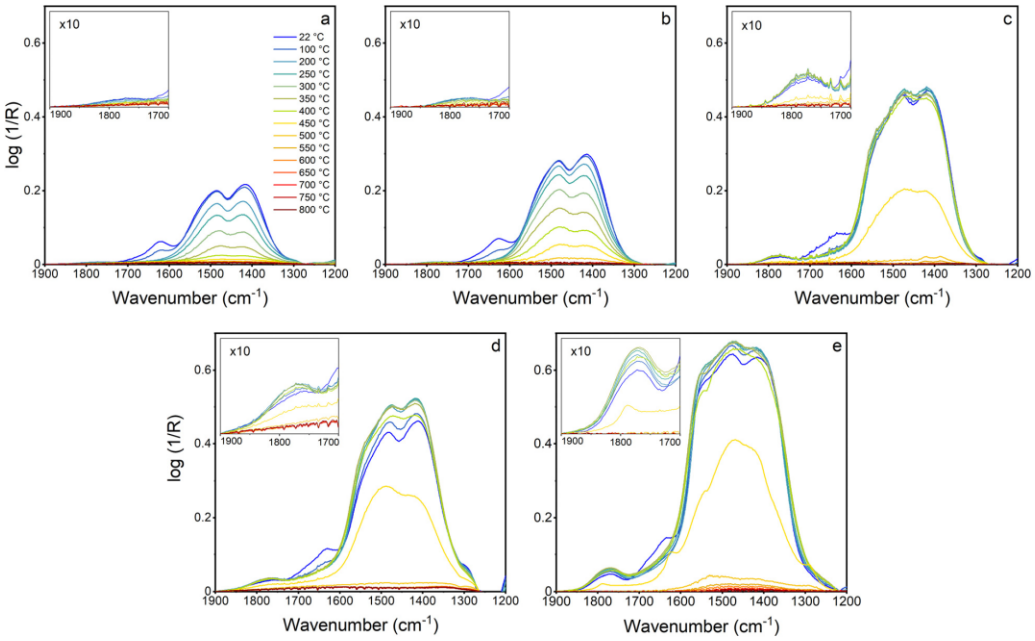

Figure 2.4 DRIFTS temperature-programmed desorption of carbonate on (a) 0.4% Ca/ZnO, (b) 2% Ca/ZnO, (c) 35% Ca/ZnO, (d) 45% Ca/ZnO, and (e) CaO after adsorption of CO_2 at room temperature, with temperature ramping in N_2 at rate 1 °C min^{-1}. Spectra have been subtracted by those of sample at corresponding temperature prior to carbonate adsorption. Desorption spectra for pure ZnO are shown in Fig. S2.8.

The desorption temperature of carbonates is a measure of oxide surface Brønsted basicity. In this system, evaluation of surface basicity informs not only on the nucleophilicity of the surface oxygen species but also how strongly CO_2, a reactant here, adsorbs and interacts with the catalyst surface. The rate-determining step of CO_2-OCM is thought to include CO_2 because of the reported relationship of C_2 product formation rate with the partial pressure of CO_2.[13,42,43] The rate of carbonate desorption can be approximated as a function of temperature.[44] The temperature at which the maximum rate of carbonate desorption is observed for each catalyst has been plotted against its activity (Fig. S2.9b), which indicates a volcano-type relationship exists. This desorption temperature approximately tracks with Ca loading and therefore the activity trends with CO_2 desorption temperature shown in Fig. 2.5 closely resemble those in Fig. 2.1.

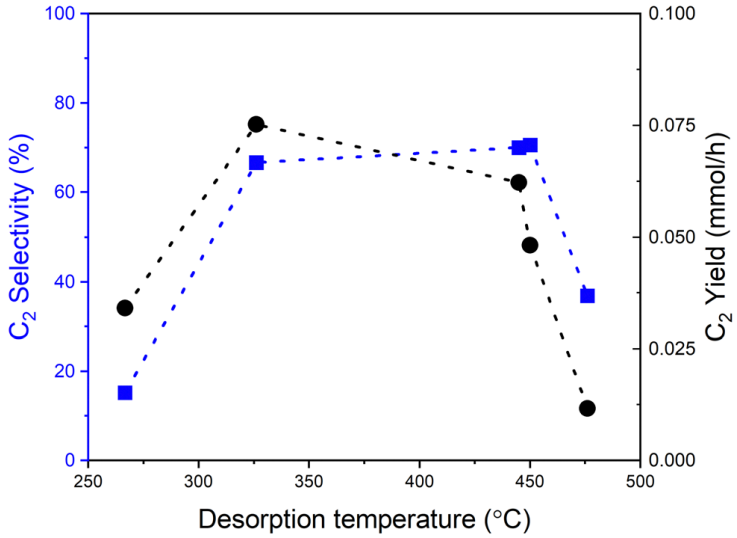

Figure 2.5 Volcano relationship between catalyst performance and CO_2 desorption temperature indicating moderate basicity enhances C–C coupling performance. Lines are included to guide the eye.

It is well-established that for a variety of reactions, including OCM,[45–47] CO_2 methanation,[48–50] methane dry reforming,[51–53] methanol carbonation,[54] and CO_2-assisted alkane dehydrogenation,[55] catalysts with medium-strength basic surface oxygen sites are optimized to increase activity. Strongly basic sites adsorb CO_2 strongly, which prevents turnover, and weakly basic sites are unable to efficiently adsorb and activate CO_2; medium-strength sites provide a balance between these contrasting behaviors. For example, a prior study of OCM showed that a mixed metal oxide catalyst results in a defective structure with greater amounts of O_{vac} and medium-strength basic sites compared to both pure oxides.[46] The presence of these two sites in a single catalyst structure yields OCM activity greater than in the constituent pure oxides.

The basicity trends of the above examples likely result from the common involvement of the elementary step of oxygen dissociation from CO_2 in their mechanisms. Because the same trend can be observed here, we can infer a similar mechanism, which depends on the coexistence of O_{vac} and medium-strength basic sites, is operable for CO_2-OCM with this composite catalyst. Catalysts with primarily strong surface basic sites adsorb significant quantities of CO_2, which is associated with more stable carbonate under reaction conditions. These surface carbonates have been demonstrated to reduce yields of C_2 products with CaO catalysts because they block active sites.[21] Previous reports examining CO_2-OCM have shown that, when coupled with reducible oxide such as a ZnO or CeO_2, oxides more strongly basic than CaO such

as SrO and BaO yield decreased CH_4 conversion and C_2 selectivity, with decreases associated with increasing basicity of the oxides.[9,14] Additional IR experiments performed in the presence of CO_2 show that in this condition carbonates remain on the catalyst surface at reaction temperature (Fig. S2.10). In contrast, high concentrations of weakly basic sites both reduce the total amount of CO_2 on the catalyst surface and the rate of CO_2 dissociation, which is required to form reactive surface oxygen species. Istadi and Amin computationally determined that in a CaO-MnO/CeO_2 catalyst, increasing CaO concentration up to 8.2 wt% enhances CO_2 adsorption and improves C_2 selectivity.[56] Calcium oxide is strongly basic and zinc oxide is weakly basic,[15,42] which is consistent with observations here on the low CH_4 coupling activity for both pure metal oxides. Using basicity as a tunable parameter to influence yield allows for flexibility in composition for catalyst design. In summary, the construction of a composite catalyst comprised of a strongly basic oxide and weakly basic reducible oxide produces interfacial sites associated with moderate basicity, which enables C_2 product yields from CO_2-OCM greater than possible with the constituent oxides alone.

2.5 Conclusions

This work describes an investigation into the effects of Ca loading and associated electronic and physical properties to understand observed enhancements of CO_2-assisted CH_4 coupling with Ca/ZnO catalysts. Addition of a small amount – 0.6 mol% – of Ca to a ZnO catalyst surface was observed to result in a significant increase in both C_2 product selectivity and yield. Comparative reactor studies with physical mixtures of CaO and ZnO show that the presence of the interface between these oxides is essential for high coupling activity. The catalysts were characterized to understand this promotional effect and the role of the interface. XRD, XPS, and XANES results indicate that samples with less than 2 mol% Ca possessed characteristics distinct from those with greater amounts. IR-TPD was used to study surface basicity. Correlating these data with activity yields a volcano-type relationship between CO_2 adsorption strength on the catalyst surface and its performance as a catalyst for CO_2-assisted CH_4 coupling. Moderately basic sites are optimal for CH_4 coupling, which is consistent with results that have been reported for OCM with O_2 as the oxidant. All composite catalysts studied were associated with weaker CO_2 adsorption than pure CaO.

Taken together, results from these characterization methods suggest that CH_4 coupling activity is controlled by the interaction of CO_2 at the interfacial sites between CaO and ZnO. The next steps of investigation of this system should involve work to characterize the interfacial sites using probes that are sensitive to the local chemical environment around metal centers, such as Ca and Zn K-edge EXAFS. These findings show that catalysts for CO_2-OCM can be designed to facilitate high C_2 product yields through optimization of basicity and concentration of sites that form at the interfaces between dissimilar metal oxides.

2.6 Acknowledgements

L. R. F., C. X. K., and R. C. R. acknowledge NSF CBET-2034647 for support of technique development and the investigation of the role of carbon dioxide in this system. L. R. F. and C. X. K. acknowledge DOE BES DE-SC0020320 for support of experiment development related to methane coupling. Part of this study was carried out at the Advanced Materials Characterization and Testing laboratory (AMCaT) at UC Davis. We thank the National Science Foundation Division of Materials Research for funding the acquisition of the XPS used in this work (award no. MRI-182838) as well as the SEM (MRI-1725618). This research used resources of the Advanced Light Source, which is a DOE Office of Science User Facility under contract no. DE-AC02- 05CH11231.

2.7 References

(1) Hu, D.; Ordomsky, V. v.; Khodakov, A. Y. Major Routes in the Photocatalytic Methane Conversion into Chemicals and Fuels under Mild Conditions. Appl. Catal. B 2021, 286, 119913.

(2) Horn, R.; Schlögl, R. Methane Activation by Heterogeneous Catalysis. Catal. Lett. 2015, 145 (1), 23–39.

(3) Lee, J. S.; Oyama, S. T. Oxidative Coupling of Methane to Higher Hydrocarbons. Catal. Rev. Sci. Eng. 1988, 30 (2), 249–280.

(4) Arinaga, A. M.; Ziegelski, M. C.; Marks, T. J. Alternative Oxidants for the Catalytic Oxidative Coupling of Methane. Angew. Chem. Int. Ed. 2021, 60 (19), 10502–10515.

(5) Cai, X.; Hu, Y. H. Advances in Catalytic Conversion of Methane and Carbon Dioxide to Highly Valuable Products. Energy Sci. Eng. 2019, 7 (1), 4–29.

(6) Aika, K. I.; Nishiyama, T. Utilisation of CO_2 in the Oxidative Coupling of Methane over PbO-MgO and PbO-CaO. J. Chem. Soc., Chem. Commun. 1988, No. 1, 70–71.

(7) Asami, K.; Fujita, T.; Kusakabe, K.-I.; Nishiyama, Y.; Ohtsuka, Y. Conversion of Methane with Carbon Dioxide into C_2 Hydrocarbons over Metal Oxides. Appl. Catal. A: General 1995, 126 (2), 245–255.

(8) Wang, Y.; Takahashi, Y.; Ohtsuka, Y. Carbon Dioxide-Induced Selective Conversion of Methane to C_2 Hydrocarbons on CeO_2 Modified with CaO. Appl. Catal. A 1998, 172 (2), L203–L206.

(9) Wang, Y.; Ohtsuka, Y. Mn-Based Binary Oxides as Catalysts for the Conversion of Methane to C_2 Hydrocarbons with Carbon Dioxide as Oxidant. Appl. Catal. A 2001, 219 (1–2), 183–193.

(10) Wang, Y.; Takahashi, Y.; Ohtsuka, Y. Effective Catalysts for Conversion of Methane to Ethane and Ethylene Using Carbon Dioxide. Chem. Lett. 1998, 12, 1209–1210.

(11) Chen, C.; Xu, Y.; Li, G.; Guo, X. Oxidative Coupling of Methane by Carbon Dioxide: A Highly C_2 Selective La_2O3/ZnO Catalyst. Catal. Lett. 1996, 42 (3–4), 149–153.

(12) Driscoll, D. J.; Martir, W.; Wang, J. X.; Lunsford, J. H. Formation of Gas-Phase Methyl Radicals Over MgO. J. Am. Chem. Soc. 1985, 107 (1), 58–63.

(13) Wang, Y.; Ohtsuka, Y. CaO-ZnO Catalyst for Selective Conversion of Methane to C_2 Hydrocarbons Using Carbon Dioxide as the Oxidant. J. Catal. 2000, 192 (1), 252–255.

(14) Wang, Y.; Takahashi, Y.; Ohtsuka, Y. Carbon Dioxide as Oxidant for the Conversion of Methane to Ethane and Ethylene Using Modified CeO_2 Catalysts. J. Catal. 1999, 186 (1), 160–168.

(15) He, Y.; Yang, B.; Cheng, G. On the Oxidative Coupling of Methane with Carbon Dioxide over CeO_2/ZnO Nanocatalysts. Catal. Today 2004, 98 (4), 595–600.

(16) Mirghiasi, Z.; Bakhtiari, F.; Darezereshki, E.; Esmaeilzadeh, E. Preparation and Characterization of CaO Nanoparticles from $Ca(OH)_2$ by Direct Thermal Decomposition Method. J. Ind. Eng. Chem. 2014, 20 (1), 113–117.

(17) Moulder, J. F.; Stickle, W. F.; Sobol, P. E.; Bomben, K. D. Handbook of X-Ray Photoelectron Spectroscopy, 2nd ed.; Chastain, J., Ed.; Perkin-Elmer Corporation: Eden Prairie, MN, 1992.

(18) Patel, M.; Aswath, P. B. Morphology, Structure and Chemistry of Extracted Diesel Soot: Part II: X-Ray Absorption near Edge Structure (XANES) Spectroscopy and High Resolution Transmission Electron Microscopy. Tribol. Int. 2012, 52, 17–28.

(19) Yuste, M.; Escobar Galindo, R.; Caretti, I.; Torres, R.; Sánchez, O. Influence of the Oxygen Partial Pressure and Post-Deposition Annealing on the Structure and Optical Properties of ZnO Films Grown by Dc Magnetron Sputtering at Room Temperature. J. Phys. D 2012, 45 (2), 025303–025314.

(20) Steinfeld, A.; Frei, A.; Kuhn, P.; Wuillemin, D. Solar Thermal Production of Zinc and Syngas via Combined ZnO-Reduction and CH_4-Reforming Processes. Int. J. Hydrog. Energy 1995, 20 (10), 793–804.

(21) Thum, L.; Rudolph, M.; Schomäcker, R.; Wang, Y.; Tarasov, A.; Trunschke, A.; Schlögl, R. Oxygen Activation in Oxidative Coupling of Methane on Calcium Oxide. J. Phys. Chem. C 2019, 123 (13), 8018–8026.

(22) Pöppl, A.; Völkel, G. ESR Investigation of the Oxygen Vacancy in Pure and Bi_2O_3-doped Zno Ceramics. Phys. Stat. Sol. (a) 1989, 115 (1), 247–255.

(23) Chen, R.; Wang, J.; Luo, S.; Xiang, L.; Li, W.; Xie, D. Unraveling Photoexcited Electron Transfer Pathway of Oxygen Vacancy-Enriched ZnO/Pd Hybrid toward Visible Light-Enhanced Methane Detection at a Relatively Low Temperature. Appl. Catal. B 2020, 264, 118554.

(24) Fu, X.; Li, J.; Long, J.; Guo, C.; Xiao, J. Understanding the Product Selectivity of Syngas Conversion on ZnO Surfaces with Complex Reaction Network and Structural E. ACS Catal. 2021, 11, 12264–12273.

(25) Zhang, M.; Averseng, F.; Krafft, J.-M.; Borghetti, P.; Costentin, G.; Stankic, S. Controlled Formation of Native Defects in Ultrapure ZnO for the Assignment of Green Emissions to Oxygen Vacancies. J. Phys. Chem. C 2020, 124, 12696–12704.

(26) Qi, J.; Hu, X. The Loss of ZnO as the Support for Metal Catalysts by H_2 Reduction. Phys. Chem. Chem. Phys. 2020, 22 (7), 3953–3958.

(27) Borgwardt, R. H. Calcium Oxide Sintering in Atmospheres Containing Water and Carbon Dioxide. Ind. Eng. Chem. Res. 1989, 28 (4), 493–500.

(28) Fink, K. Ab Initio Cluster Calculations on the Electronic Structure of Oxygen Vacancies at the Polar ZnO(0001) Surface and on the Adsorption of H_2, CO, and CO_2 at These Sites. Phys. Chem. Chem. Phys. 2006, 8 (13), 1482–1489.

(29) Lassaletta, G.; Fernández, A.; Espinós, J. P.; González-Elipe, A. R. Spectroscopic Characterization of Quantum-Sized TiO_2 Supported on Silica: Influence of Size and TiO_2-SiO_2 Interface Composition. J. Phys. Chem. 1995, 99 (5), 1484–1490.

(30) Espinós, J. P.; Morales, J.; Barranco, A.; Caballero, A.; Holgado, J. P.; González-Elipe, A. R. Interface Effects for Cu, CuO, and Cu_2O Deposited on SiO_2 and ZrO_2. XPS Determination of the Valence State of Copper in Cu/SiO_2 and Cu/ZrO_2 Catalysts. J. Phys. Chem. B 2002, 106 (27), 6921–6929.

(31) Henderson, G. S.; de Groot, F. M. F.; Moulton, B. J. A. X-Ray Absorption Near-Edge Structure (XANES) Spectroscopy. Rev. Mineral. Geochem. 2014, 78 (1), 75–138.

(32) Hu, Y.; Wang, N.; Zhou, Z. Synergetic Effect of Cu Active Sites and Oxygen Vacancies in Cu/CeO_2-ZrO_2 for Water-Gas Shift Reaction. Catal. Sci. Technol. 2021, 11 (7), 2518–2528.

(33) Giehr, A.; Maier, L.; Schunk, S. A.; Deutschmann, O. Thermodynamic Considerations on the Oxidation State of Co/γ-Al_2O_3 and Ni/γ-Al_2O_3 Catalysts under Dry and Steam Reforming Conditions. ChemCatChem 2018, 10 (4), 751–757.

(34) Zhanpeisov, N. U.; Zhidomirov, G. M.; Baerns, M. Cluster Quantum-Chemical Study of the Chemisorption of Methane on Zinc Oxide Surface. J Mol Catal A Chem 1995, 99 (1), 35–39.

(35) Gao, J.; Hou, Z.; Lou, H.; Zheng, X. Dry (CO_2) Reforming. In Fuel Cells: Technologies for Fuel Processing; Elsevier, 2011; pp 191–221.

(36) Kumar, G.; Lau, S. L. J.; Krcha, M. D.; Janik, M. J. Correlation of Methane Activation and Oxide Catalyst Reducibility and Its Implications for Oxidative Coupling. ACS Catal. 2016, 6 (3), 1812–1821.

(37) Jiang, X.; Lis, B. M.; Purdy, S. C.; Paladugu, S.; Fung, V.; Quan, W.; Bao, Z.; Yang, W.; He, Y.; Sumpter, B. G.; Page, K.; Wachs, I. E.; Wu, Z. CO_2-Assisted Oxidative Dehydrogenation of Propane over VO_x/In_2O_3 Catalysts: Interplay between Redox Property and Acid–Base Interactions. ACS Catal. 2022, 12, 11239–11252.

(38) Philipp, R.; Fujimoto, K. FTIR Spectroscopic Study of CO_2 Adsorption/Desorption on MgO/CaO Catalysts. J. Phys. Chem. 1992, 96 (22), 9035–9038.

(39) Santos, V. H. J. M. dos; Pontin, D.; Ponzi, G. G. D.; Stepanha, A. S. de G. e.; Martel, R. B.; Schütz, M. K.; Einloft, S. M. O.; Dalla Vecchia, F. Application of Fourier Transform Infrared Spectroscopy (FTIR) Coupled with Multivariate Regression for Calcium Carbonate ($CaCO_3$) Quantification in Cement. Constr. Build. Mater. 2021, 313, 125413.

(40) Alba-Rubio, A. C.; Santamaría-González, J.; Mérida-Robles, J. M.; Moreno-Tost, R.; Martín-Alonso, D.; Jiménez-López, A.; Maireles-Torres, P. Heterogeneous Transesterification Processes by Using CaO Supported on Zinc Oxide as Basic Catalysts. Catal. Today 2010, 149, 281–287.

(41) Zhu, L.; Cao, M.; Zhou, H.; Zhang, N.; Zheng, J.; Li, Y.; Chen, B. H. A Highly Stable and Active CaO/Al_2O_3 Base Catalyst in the Form of Calcium Aluminate Phase for Oxidation of Cyclohexanone to ε-Caprolactone. Catal. Lett. 2014, 144 (7), 1188–1196.

(42) Wang, Y.; Zhuang, Q.; Takahashi, Y.; Ohtsuka, Y. Remarkable Enhancing Effect of Carbon Dioxide on the Conversion of Methane to C_2 Hydrocarbons Using Praseodymium Oxide. Catal. Letters 1998, 56, 203–206.

(43) Yabe, T.; Kamite, Y.; Sugiura, K.; Ogo, S.; Sekine, Y. Low-Temperature Oxidative Coupling of Methane in an Electric Field Using Carbon Dioxide over Ca-Doped $LaAlO_3$ Perovskite Oxide Catalysts. J. CO_2 Util. 2017, 20 (April), 156–162.

(44) Thang, H. V.; Pacchioni, G.; DeRita, L.; Christopher, P. Nature of Stable Single Atom Pt Catalysts Dispersed on Anatase TiO_2. J. Catal. 2018, 367, 104–114.

(45) Wang, H.; Schmack, R.; Sokolov, S.; Kondratenko, E. V.; Mazheika, A.; Kraehnert, R. Oxide-Supported Carbonates Reveal a Unique Descriptor for Catalytic Performance in the Oxidative Coupling of Methane (OCM). ACS Catal. 2022, 12, 9325–9338.

(46) Zhang, Z.; Gong, Y.; Xu, J.; Zhang, Y.; Xiao, Q.; Xi, R.; Xu, X.; Fang, X.; Wang, X. Dissecting $La_2Ce_2O_7$ Catalyst to Unravel the Origin of the Surface Active Sites Devoting to Its Performance for Oxidative Coupling of Methane (OCM). Catal. Today 2021, 400–401, 73–82.

(47) Siakavelas, G. I.; Charisiou, N. D.; AlKhoori, A.; Gaber, S.; Sebastian, V.; Hinder, S. J.; Baker, M. A.; Yentekakis, I. V.; Polychronopoulou, K.; Goula, M. A. Oxidative Coupling of Methane on Li/CeO_2 Based Catalysts: Investigation of the Effect of Mg- and La-Doping of the CeO_2 Support. Mol. Catal. 2022, 520, 112157.

(48) Bukhari, S. N.; Chong, C. C.; Setiabudi, H. D.; Ainirazali, N.; Aziz, M. A. A.; Jalil, A. A.; Chin, S. Y. Optimal Ni Loading towards Efficient CH_4 Production from H_2 and CO_2 over Ni Supported onto Fibrous SBA-15. Int. J. Hydrog. Energy 2019, 44 (14), 7228–7240.

(49) Pan, Q.; Peng, J.; Sun, T.; Wang, S.; Wang, S. Insight into the Reaction Route of CO_2 Methanation: Promotion Effect of Medium Basic Sites. Catal. Commun. 2014, 45, 74–78.

(50) Gao, X.; Wang, Z.; Huang, Q.; Jiang, M.; Askari, S.; Dewangan, N.; Kawi, S. State-of-Art Modifications of Heterogeneous Catalysts for CO_2 Methanation – Active Sites, Surface Basicity and Oxygen Defects. Catal Today 2022, 402, 88–103.

(51) Zhang, L.; Li, L.; Li, J.; Zhang, Y.; Hu, J. Carbon Dioxide Reforming of Methane over Nickel Catalyst Supported on MgO(111) Nanosheets. Top. Catal. 2014, 57, 619–626.

(52) Li, X.; Li, D.; Tian, H.; Zeng, L.; Zhao, Z. J.; Gong, J. Dry Reforming of Methane over Ni/La_2O_3 Nanorod Catalysts with Stabilized Ni Nanoparticles. Appl. Catal. B 2017, 202, 683–694.

(53) Wang, Y.; Zhao, Q.; Wang, Y.; Hu, C.; da Costa, P. One-Step Synthesis of Highly Active and Stable $Ni{-}ZrO_x$ for Dry Reforming of Methane. Ind. Eng. Chem. Res 2020, 59, 11441–11452.

(54) P, U.; Darbha, S. Direct Synthesis of Dimethyl Carbonate from CO_2 and Methanol over CeO_2 Catalysts of Different Morphologies. J. Chem. Sci 2016, 128 (6), 957–965.

(55) Burri, D. R.; Choi, K. M.; Han, D. S.; Sujandi; Jiang, N.; Burri, A.; Park, S. E. Oxidative Dehydrogenation of Ethylbenzene to Styrene with CO_2 over SnO_2-ZrO_2 Mixed Oxide Nanocomposite Catalysts. Catal. Today 2008, 131 (1–4), 173–178.

(56) Istadi; Amin, N. A. S. Optimization of Process Parameters and Catalyst Compositions in Carbon Dioxide Oxidative Coupling of Methane over CaO-MnO/CeO_2 Catalyst Using Response Surface Methodology. Fuel Process. Technol. 2006, 87 (5), 449–459.

2.8 Supporting Information

Supporting Information Table of Contents

Table S2.1. Summary of catalytic performance

Sample	CH_4 Conversion (%)	CO_2 Conversion (%)	C_2H_6 Yield (mmol/h)	C_2H_4 Yield (mmol/h)	CO Yield (mmol/h)
ZnO	6.7	7.3	0.01	0.005	0.60
0.4% Ca/ZnO	4.6	4.8	0.02	0.01	0.38
0.6% Ca/ZnO	2.9	1.9	0.05	0.03	0.11
2% Ca/ZnO	2.3	1.3	0.05	0.03	0.07
35% Ca/ZnO	1.7	0.9	0.04	0.02	0.05
45% Ca/ZnO	1.4	0.7	0.04	0.01	0.04
CaO	0.6	0.5	0.006	0.006	0.04

Reaction conditions: 850 °C; 100 mg catalyst; 13.3 mL/min total gas flow rate with P_{CH_4} = 0.25 atm, P_{CO_2} = 0.5 atm, P_{N_2} = 0.25 atm; 4 h on stream. All Ca loadings are reported in molar concentration of metal cations, as determined by ICP-MS (Table S2.2).

Table S2.2. Summary of physical properties of pure and binary metal oxides.

Sample	**BET Surface Area[a] (m^2/g)**	**Ca Loading[b] (%)**	**Ca Surface Concentration[c] (%)**
ZnO	2.7075 ± 0.0127		
0.4% Ca/ZnO	3.7840 ± 0.0193	0.41	6.9
0.6% Ca/ZnO	5.4405 ± 0.0418	0.62	12.1
2% Ca/ZnO	7.2562 ± 0.1101	2.04	10.2
35% Ca/ZnO	3.0918 ± 0.0095	34.94	62.1
45% Ca/ZnO	7.0391 ± 0.0375	44.55	71.8
CaO	39.6071 ± 0.0125		

[a]Determined by N_2 physisorption. [b]Determined by ICP-MS. [c]Determined by XPS

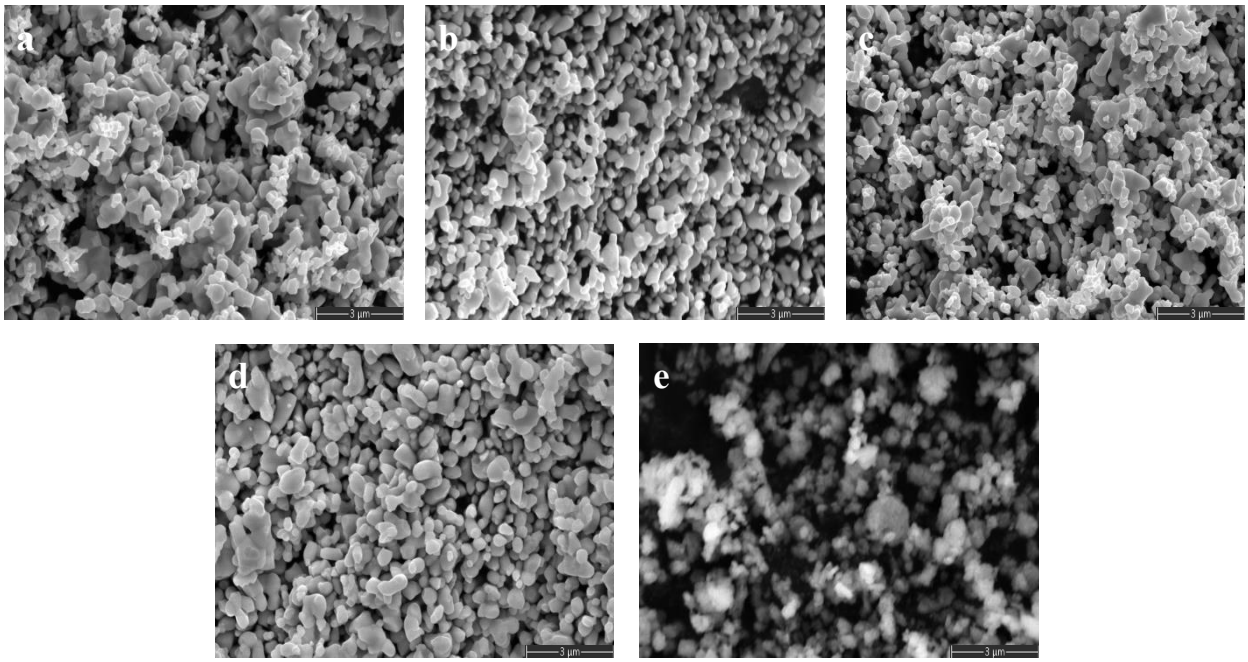

Figure S2.1. SEM images of calcined (a) ZnO, (b) 0.4% Ca/ZnO, (c) 0.6% Ca/ZnO, (d) 2% Ca/ZnO, (e) CaO.

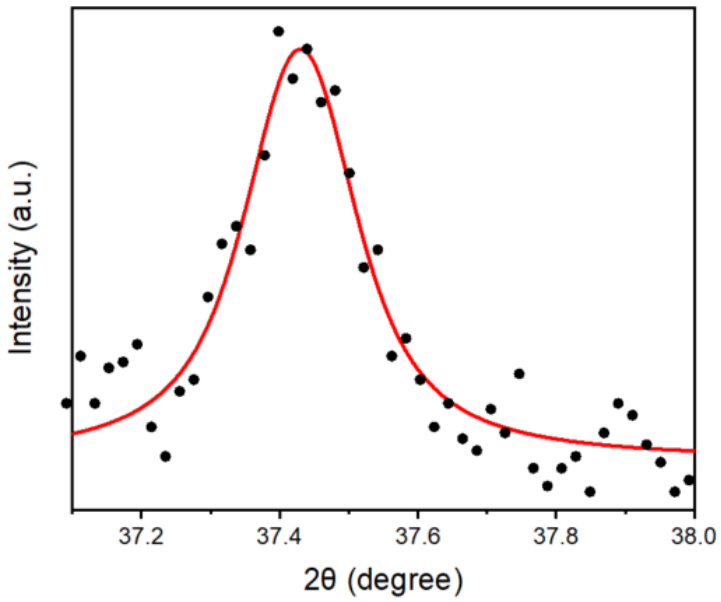

Figure S2.2. Magnification of CaO (200) peak in X-ray diffractogram characterizing the 2% Ca/ZnO sample.

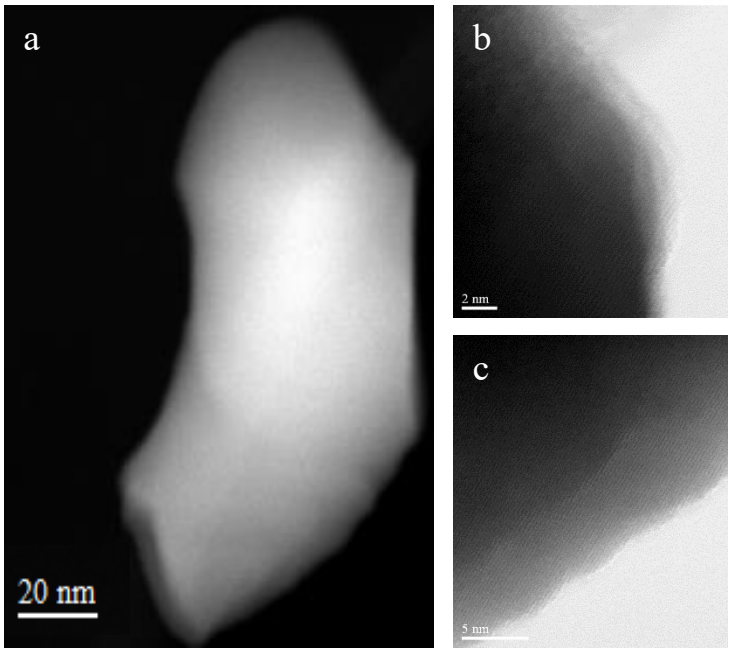

Figure S2.3. HAADF-STEM images of (a) a representative particle of 0.6% Ca/ZnO and (b-c) magnification of ZnO lattice fringes.

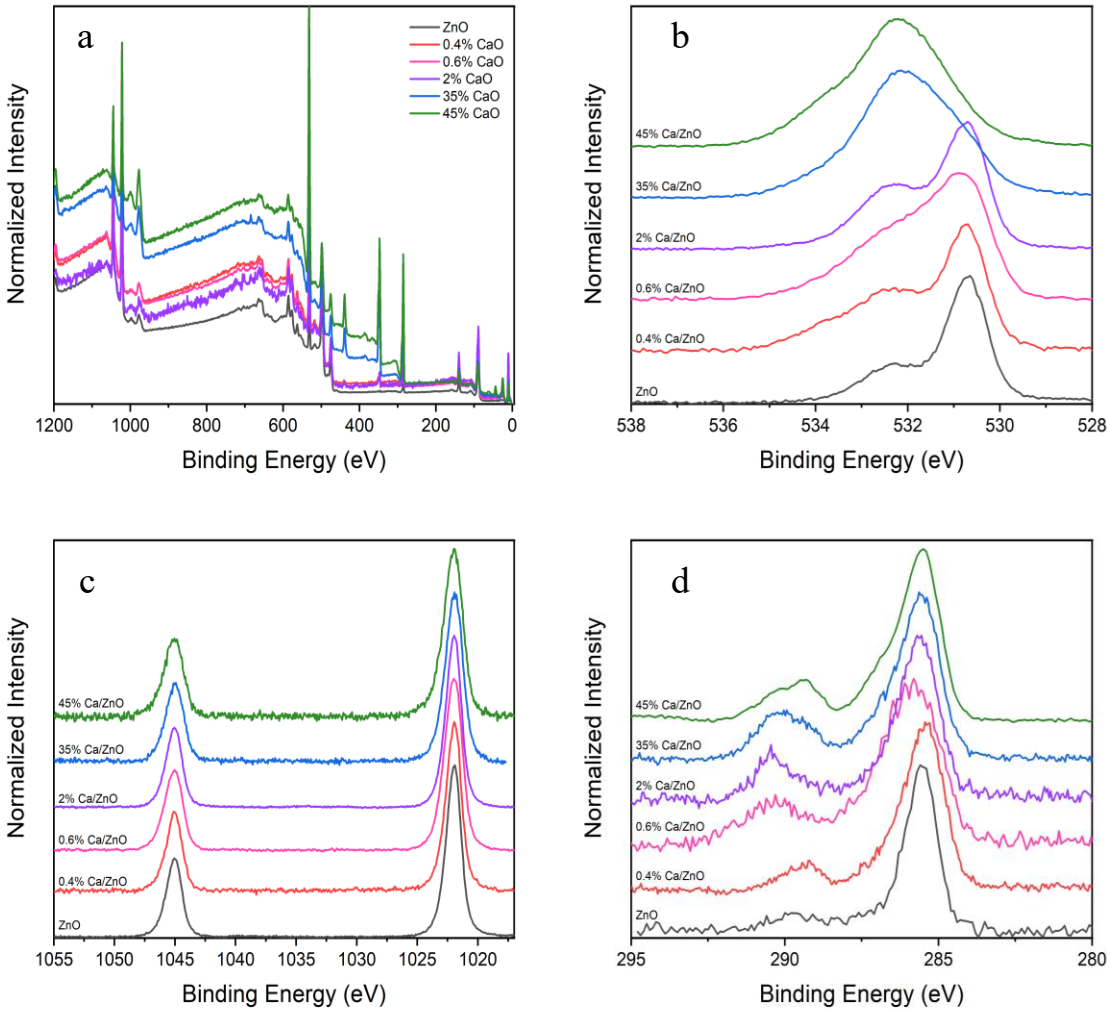

Figure S2.4. XPS spectra: (a) survey scan, and (b) O 1s, (c) Zn 2p, and (d) C 1s regions.

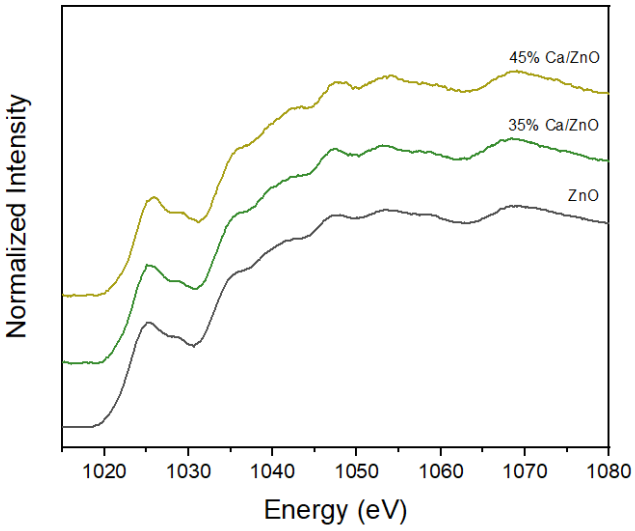

Figure S2.5. XANES spectra of Zn L_{23} region: high Ca loading samples compared to pure ZnO.

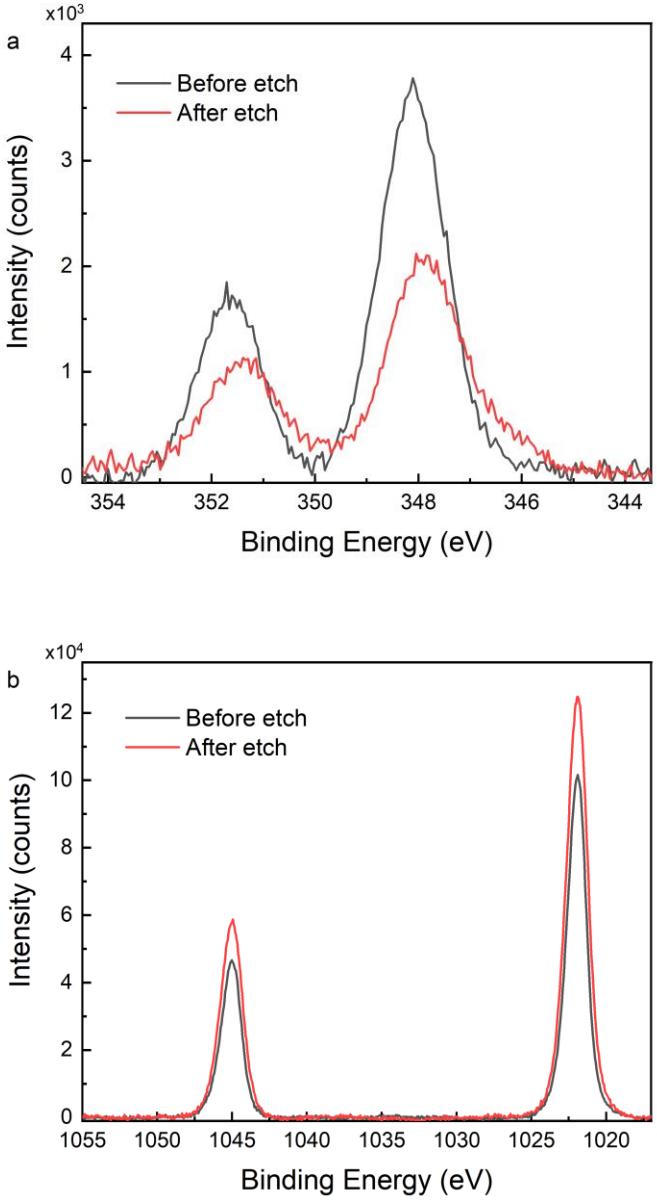

Figure S2.6. XPS scans of (a) Ca 2p and (b) Zn 2p regions characterizing 2% Ca/ZnO before and after an argon etch of the surface.

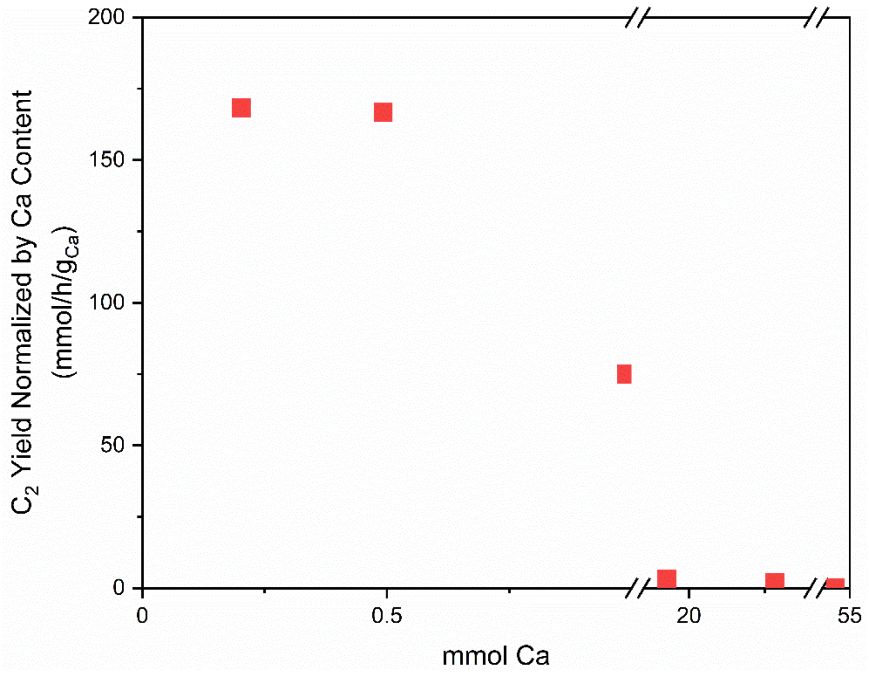

Figure S2.7. Methane coupling activity per calcium site demonstrates effectiveness of each calcium atom for different calcium loadings.

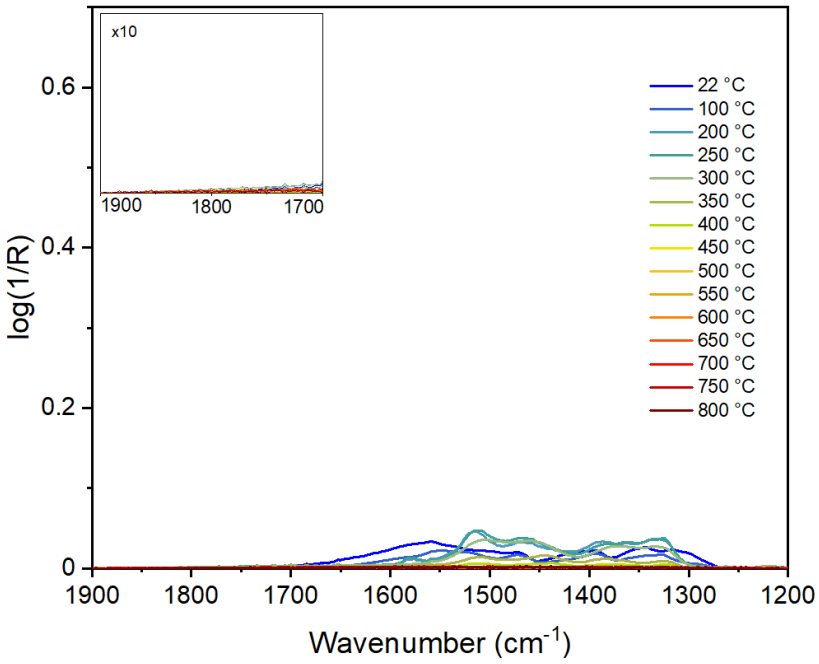

Figure S2.8. DRIFTS temperature programmed desorption of carbonate on ZnO in nitrogen ramping 1 °C/min. Spectra have been subtracted from sample at corresponding temperature prior to carbonate adsorption. Data are shown with the same axis scales as in main text Figure 2.4, for comparison.

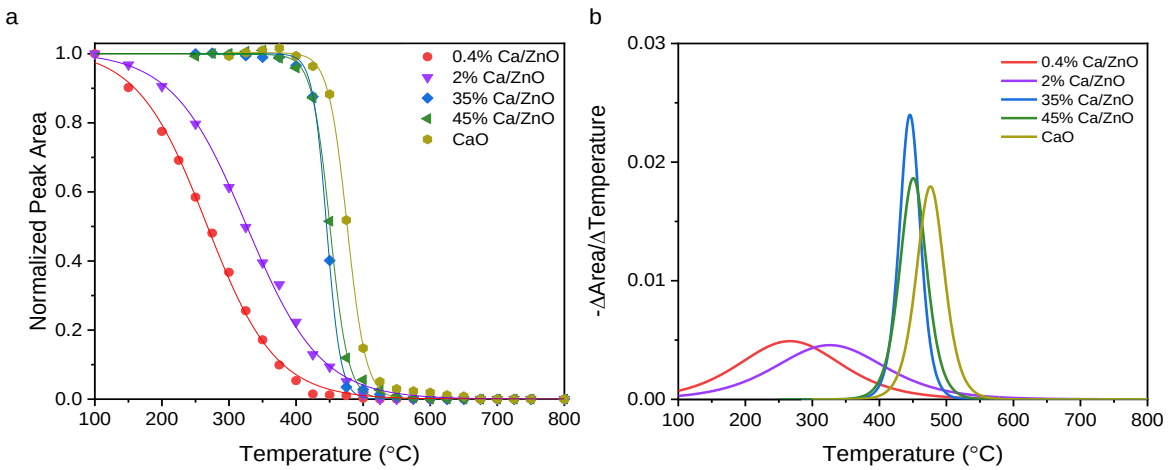

Figure S2.9. (a) DRIFTS-TPD profiles of integrated carbonate region and sigmoidal fit, (b) derivative of sigmoidal fits.

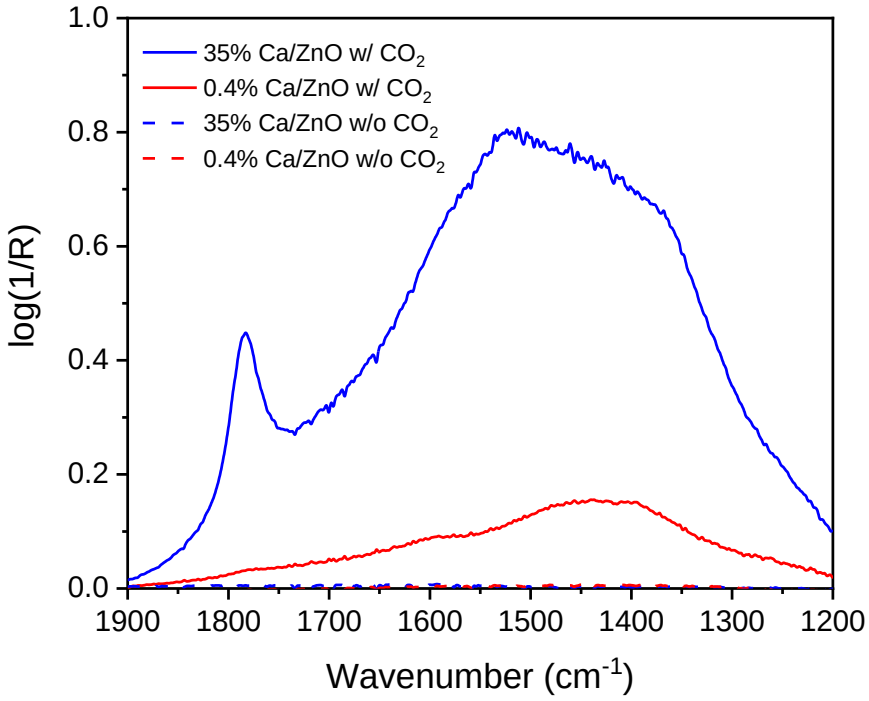

Figure S2.10. DRIFTS spectra characterizing the carbonate region at 850 °C in the absence and presence of 10% CO_2 during the temperature ramp.

Chapter 3. Impact of Local Structure in Supported CaO Catalysts for Soft Oxidant-Assisted Methane Coupling Assessed through Ca K-edge X-ray Absorption Spectroscopy

Reprinted from submission to *Journal of Physical Chemistry C*. 2023 American Chemical Society

3.1 Abstract

Soft oxidant-assisted methane coupling has emerged as a promising pathway to upgrade methane from natural gas sources to high-value commodity chemicals, such as ethylene, at selectivities higher than those associated with oxidative (O_2) methane coupling (OCM). To date, few studies report investigations into the electronic structure and the microscopic physical structure of catalytic active sites present in the binary metal oxide catalyst systems that are known to be effective for this reaction. Correlating catalyst activity to specific active site structures and electronic properties is an essential aspect of catalyst design. Here, we used X-ray absorption spectroscopy at the Ca K edge to ascertain the most probable local environment of Ca in ZnO-supported Ca oxide catalysts. These catalysts are shown here to be active for N_2O-assisted methane coupling (N_2O-OCM) and have previously been reported to be active for CO_2-assisted methane coupling (CO_2-OCM). X-ray absorption near edge structure features at multiple Ca loadings are interpreted through simulated spectra derived from ab initio full multiple scattering calculations. These simulations included consideration of CaO structures organized in multiple spatial arrangements – linear, planar, and cubic – with separate analyses of Ca atoms in the surfaces and bulk of the three-dimensional structures. Experiment and theory show that for low-Ca-loading catalysts (≤1 mol%), which contain sites particularly active for methane coupling, Ca primarily exists as oxidized, one- or two- dimensional clusters on the ZnO surface. In addition to their unique nanoscale structures, spectra also indicate that these clusters have varying degrees of undercoordinated surface Ca atoms that could further influence their catalytic activities. The local Ca structure was correlated with methane coupling activity from N_2O-OCM and previously reported CO_2-OCM reactor studies. This study provides a unique perspective on the physical and electronic

structure correlates of active sites for soft oxidant-assisted methane coupling that informs future catalyst development.

3.2 Introduction

There has been a recent surge in natural gas development, and the U.S. Department of Energy expects continual growth for at least the next several decades.[1] Natural gas is often a byproduct of oil extraction[2] in low-population areas which poses a major economic challenge for gas transportation.[3] As a result, it is often flared into carbon dioxide or released, emitting greenhouse gases to the atmosphere.[2] Roughly 90% of the end-use of natural gas is combustion for heat or energy, further adding carbon dioxide to the atmosphere.[4] Upgrading methane, the dominant chemical species present in natural gas, into a more energy-dense chemical or fuel would allow for a more efficient utilization of this abundant resource and help to reduce greenhouse gas emissions.

Oxidative coupling of methane (OCM) is a highly explored avenue of methane upgrading to larger hydrocarbons via C-C bond formation.[5] However, the presence of strong oxidant species at high temperatures leads to a strong trade-off between methane conversion and C_2 product selectivity[6] where undesirable combustion reactions of methane and C_2 products limit product yields below 30%.[7] However, the use of softer oxidants that do not form gas-phase oxygen species offers an opportunity to break the trade-off relationship. Carbon dioxide and nitrous oxide are both emerging oxidants to replace oxygen during OCM.[8–11] C_2 product selectivity over 80% can easily be achieved with binary metal oxide catalysts, notably when coupling a basic oxide with a reducible oxide.[12–14]

This cooperation had been demonstrated by previous efforts to characterize these binary oxide catalysts. For many bulk reducible metal oxides including MnO_2,[15] CeO_2,[14] CoO, CuO, Bi_2O_3, and Fe_2O_3,[16] XRD and XPS[17] have demonstrated their partial reduction after reaction. Reaction in the absence of any oxidant leads to complete reduction,[13] indicating CO_2- and N_2O-OCM proceed through a Mars van-Krevelen mechanism where oxygen vacancies are formed during the reaction with methane and are replenished by the oxidant.[12] The presence of oxygen vacancies has been confirmed in PrO_2 via O_2-TPD.[18]

Addition of a basic metal oxide can promote CO_2 chemisorption for increased conversion over the reducible sites during CO_2-OCM, demonstrated by CO_2-TPD.[12,19] Catalyst basicity and reducibility were also shown to correlate with C_2 product yields for N_2O-OCM.[20]

Recent work used CO_2-IR-TPD to establish a volcano relationship between catalyst basicity and CO_2-OCM performance.[21] The interface between basic and reducible metal oxides in a Ca/ZnO catalyst had a presence of medium-strength basicity and was proposed to be responsible for selective methane coupling. It was also observed that very low concentrations of calcium (~0.6 mol%) exhibited excellent catalytic performance, and the Ca sites had electronic and geometric properties that were not characteristic of bulk CaO species, according to various characterization methods, including Ca L-edge X-ray absorption near edge structure (XANES). However, the specific nature of these Ca species has not previously been thoroughly investigated.

X-ray absorption spectroscopy (XAS) is a useful tool for determining local structure of metal oxide nanoparticles. Decreases in second and third shell coordination numbers, relative to bulk metal oxide, have been correlated to nanoparticles of defined sizes.[22,23] These results in tandem with DFT calculations have predicted specific structures of supported metal oxide clusters with 9-13 metal atoms.[24] There have been few studies that use Ca K-edge extended X-ray absorption fine structure (EXAFS) to inform on Ca-containing nanoparticle sizes and structure of highly dispersed [25,26] and nanoparticle Ca species.[27,28]. Changes in Ca-O coordination can be observed during mineral crystallization as the solid phases become larger and more ordered.[29] Ca deposition on coal via impregnation and ion-exchange yielded catalysts that lacked any Ca-Ca coordination due to a high degree of dispersion.[25] The aggregation of $CaCO_3$ and CaO species was observed after high-temperature treatments.

This work uses Ca K-edge XAS paired with theoretical XAS simulations to evaluate the local coordination environment of Ca species in Ca/ZnO catalysts over the wide range of Ca compositions previously studied[21] and correlate structure to CO_2-OCM and N_2O-OCM performance. The structure of low-Ca-loading catalysts is contrasted with that of bulk CaO species to reveal the presence of ultra-small CaO clusters with one-dimensional linear and two-dimensional planar geometries. The difference in active

site structure is associated with enhanced methane coupling performance for low-Ca-loading Ca/ZnO catalysts.

3.3 Materials and Methods

Catalyst Synthesis

Calcium carbonate (98% purity) and calcium hydroxide (98% purity) were acquired from VWR and Acros Organics, respectively. Calcium oxide-zinc oxide composite catalysts were prepared via a wet impregnation synthesis as described earlier.[21] Briefly, calcium nitrate tetrahydrate (99% ACS Reagent, MP Biomedicals) was dissolved in MilliQ (18 Mohm) water. Zinc oxide (99.9% metal basis, Alfa Aesar) was added, and the resulting slurry was sonicated, and stirred partially covered overnight. The resulting white solids were dried at 120 °C for 24 h before calcining in 50 mL/min air (zero air, Praxair) at 850 °C (ramp 5 °C/min) for 4 h. Henceforth, the Ca loading will be denoted by the resulting Ca/(Zn + Ca) ratio, or mol% of cation. Calcium oxide was synthesized by heating 100 mL of a 0.25M calcium nitrate solution in an oil bath to 80°C.[30] Under vigorous stirring, a 50 mL solution of 1M NaOH was added dropwise, resulting in a cloudy solution of white precipitate. The solids were vacuum filtered, washed with deionized water, and dried overnight at 120 °C before calcination (see above). Calcium composition was determined by ICP-OES (Table S1).

Materials Characterization

Calcium K-edge XAS data were collected at beamline 4-3 of the Stanford Synchrotron Radiation Lightsource equipped with a double-crystal Si(111) monochromator at an orientation of $\Phi = 90°$. Helium was used as the ionization chamber gas, with the ion chamber voltage at 200 VDC and negative polarity. To minimize absorption by air at these low photon energies, a UHP helium-purged tube was installed between the first ion chamber and the sample stage. The photon energy was initially calibrated with a Ti metal foil in transmission mode. The beamline was calibrated by defining the edge energy, the maximum if the first derivative of the Ti foil spectra, to 4966.0 eV. Subsequently, an initial reference spectrum of $CaCO_3$ was acquired where E_0 was observed to be 4037.6 eV. Measurements of $CaCO_3$ were repeated at least every 24 h, and E_0 was aligned to 4037.6 eV to account for any drift in the monochromator. Spectra

were acquired between 3805.0 and 4645.0 eV. At least 4 spectra of each sample were acquired and merged to improve the signal-to-noise ratio. All data was collected in fluorescent mode. For calcium catalysts with ≤2 mol%, data was collected using a 7-element Canberra silicon-drift detector. For all other samples and standards, a PIPS detector was used. Approximately 1-3 mg of sample were ground to a fine powder and smeared as a thin uniform layer onto a zero sulfur-containing adhesive tape and placed in an air-tight cell inside a glovebox and then transferred to the beamline stage with helium flow.

Post-processing and analysis of the XAS data were performed using the Athena and Artemis software of the Demeter package.[31] Energy correction was applied from the corresponding $CaCO_3$ glovebox reference spectrum. Normalization of the pre-edge region in the range of 43.4 to 20.0 eV below the edge with a linear fit, and in the range of 50.0 to 400.0 eV above the edge with second-order polynomial fit. The data were modeled in q-space to reduce any errors associated with fitted coordination numbers by filtering out high-frequency (scattering paths at longer R) components from the data. The data was fit in the q-range of 3.4 to 9.1 $Å^{-1}$. The same k-range and a back Fourier transform R-range of 1.0 to 3.5 Å was used. EXAFS models were built using scattering paths generated from cif files using FEFF6. cif files were downloaded from the Materials Project[32] and consisted of $Ca(OH)_2$ (mp-23879), CaO (mp-2605), and ZnO (mp-2133) where the central Zn atom was replaced with a Ca atom to simulate an isolated Ca atom within the ZnO lattice. The amplitude reduction factor S_0^2 was determined from a fit of 2 mol% Ca/ZnO to be 0.73. For all catalysts, the Ca-O coordination number was fixed to 6.

Computational Details

The XANES simulations were performed with FEFF10.[33–35] The SCF stage used a cut off radius of 5 Å, and maximum angular momenta of 3 and 2 for Ca and O, respectively. The FMS stage used a cut off radius of 9 Å, with maximum angular momenta of 4 and 3 for Ca and O, respectively. These values ensured convergence for the bulk case. The model for the bulk CaO simulations was generated from the experimental structure[36] of CaO with space group $Fm\bar{3}m$ and lattice constant 4.8105 Å, resulting in a Ca-O bond distance of 2.405 Å. The model for the Ca in the surface was generated by cleaving the bulk model in order to expose the (100) surface. The cluster models were generated by repeating the neutral Ca_4O_4 cubic

unit along one, two, or three directions in order to generate "linear", "planar" and "cubic" clusters (as shown in insets of Figure 3.4). These are labeled as (n,l,m) according to the number of cubic units in each direction. For simplicity, all structures retain the original crystal structure. All calculations used the final state rule approximation for the core hole, and the default Hedin-Lundqvist approximation for the self-energy. The calculations also included room temperature thermal damping at the level of single scattering, using the correlated Debye model with a Debye temperature of 562 K. This temperature was chosen to match the fitted σ^2 for the Ca-O paths in the catalysts at 300 K. While the bulk and surface simulations were performed on a single representative Ca atom, for the (n,l,m) clusters the XANES calculations were performed for each Ca atom in the structure, and the resulting spectra averaged to obtain the final result. The effect of dipole-forbidden transitions was studied by adding the MULTIPOLE card to the FEFF calculations to include quadrupole contributions. In addition, the effect of s→d transitions were quantified by removing the s→p contributions from the total spectra. The theoretical spectra were normalized using a procedure similar to that used in EXAFS analysis in which the post-edge decay of the atomic background is removed. Finally, the difference between the XANES of the catalysts and that of bulk CaO (ΔXANES) was quantitatively compared to that of the (n,l,m) clusters and the theoretically simulated bulk CaO. This was done using a Frechet form figure of merit (FOM), described in detail in the SI.

Catalytic Activity Measurements

N_2O-OCM experiments over a series of Ca loadings were conducted in a quartz down-flow, packed-bed reactor with 4 mm ID. A sample mass of 0.750 g was sieved between 250 and 425 μm and loaded into the tube, supported by quartz wool (Acros Organics). The reactor was heated in a tubular furnace at 5 °C min^{-1} to 800 °C under 13.3 mL min^{-1} argon (99.997%, Praxair) and then quickly cooled to 550 °C. Flow was then switched to bypass the reactor and adjusted to 3.3 mL min^{-1} methane (99.9995%, Matheson), 6.7 mL min^{-1} nitrous oxide (99.998%, Linde), and 3.3 mL min^{-1} argon prior to flow through the reactor. Reaction products were measured by an online Agilent 7890A gas chromatograph (GC) with a CP-SilicaPLOT column to quantify hydrocarbon species with FID and Porapak Q and ShinCarbon ST columns to quantify all other species with TCD. Activation energies were determined after verifying the reactor was in a

differential regime. A sample mass of 0.2 g and a total flowrate of 30 mL min^{-1} with varying feed ratios were used. The reactor was heated in a tubular furnace at 5 °C min^{-1} to 800 °C under 13.3 mL min^{-1} argon and then quickly cooled to 520 °C. Flow was then switched to bypass the reactor and stabilize for 45 minutes. Reactor temperature was held for 2.5 h while injecting to the GC, then quickly ramped by 10 °C and held for another 2.5 h. This proceeded from 520 °C to 560 °C. Steady state data over the 2.5 h period was averaged.

3.4 Results and Discussion

XANES and Pre-Edge Evaluation of Calcium Structure

The XANES spectra of Ca/ZnO catalysts with varying concentrations of Ca are compared to common bulk Ca reference compounds – CaO, $Ca(OH)_2$, and $CaCO_3$ – in Figure 3.1. The overall shape of the spectra of all Ca/ZnO catalysts resemble that of CaO, with the white line absorption centered at 4046.8 eV and a significant shoulder feature at 4037.9 eV. Spectra of catalysts with 2 mol% and higher Ca content are nearly identical to that of CaO, indicating that Ca exists in its bulk oxide phase in these higher Ca-loaded catalysts (Figure S3.1). This is consistent with XRD, TEM, and L-edge XANES results, published in prior work.[21] Below 2 mol% Ca content, the shoulder feature diminishes, the white line peak decreases and broadens, a new pre-edge feature grows at 4034.3 eV, and post-edge oscillations are significantly dampened. These features resemble those seen in the spectrum of $Ca(OH)_2$, but rigorous EXAFS analysis verifies the absence of a hydroxide phase; XAS associated the hydroxide phase is addressed later. The new pre-edge feature is only present in the two lowest Ca-loading catalysts. Several different physical assignments of this peak have been reported.[37,38] Theoretical simulations of Ca local density of states, provided later in this report, provides justification for assigning this peak to a Ca 1s to p electronic transition.

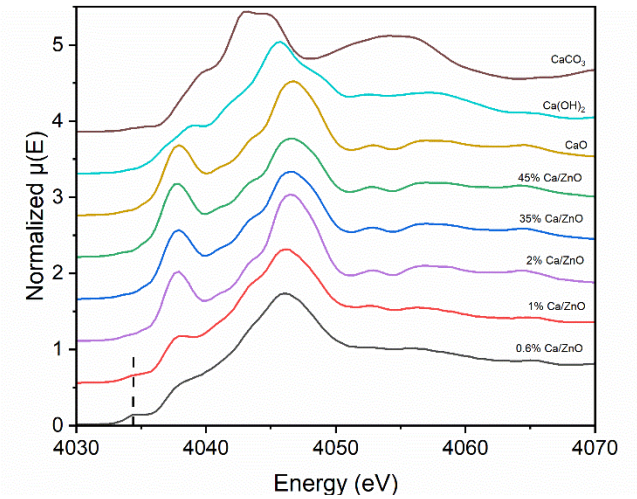

Figure 3.1. *Ex situ* Ca K-edge XANES spectra collected at room temperature in He. Dashed line to visualize pre-edge feature. Spectra offset for clarity.

Structural Characterization Analyzing Extended X-ray Absorption Fine Structure Spectroscopy

Modeling of the EXAFS spectra provides information on the local structure of dispersed Ca sites present in the low-Ca-loading catalysts – 1 and 0.6 mol% Ca/ZnO. To determine the precise Ca coordination environment, a q-space fit was used[39] to filter out high frequency components to quantify observed changes in specifically the first two scattering paths (see Methods for more details). At high Ca composition, self-absorption[40] distorts the data for >2 mol% Ca, which prevents EXAFS analysis of those catalysts. The 2 mol% Ca/ZnO catalyst was reported to contain CaO particles >40 nm in size, determined by XRD.[21] This sample has well-defined XAS features that demonstrate the absence of the self-absorption effects observed with higher Ca loadings. Combined, these results reinforce our assumption that the Ca speciation in 2 mol% Ca/ZnO catalyst is equivalent to that of bulk CaO. Thus, the 2 mol% Ca/ZnO catalyst was used to determine the value of S_0^2, 0.73 (Figure S3.2, Table S3.2), which is consistent with a previously reported value of 0.8.[41]

The magnitudes of the Fourier transforms of the EXAFS spectra for the low-Ca-loading catalysts are shown in Figure 3.2. The first peak is comparable in intensity across the three catalysts. The 1 and 0.6 mol% Ca/ZnO catalysts exhibit a significant decrease in all peak intensities at distances beyond 2.4 Å. Path

analysis of CaO (Figure S3.3) shows that the first peak is associated with Ca-O at bonding distance 2.42 Å and the second peak is only associated with Ca-Ca single scattering at a distance of 3.42 Å. These results suggests that, at loadings ≤1 mol%, the Ca exists as nanoparticles significantly smaller than those in the higher-Ca-loading catalysts, where we henceforth refer to the ultra-small microstructure of Ca in the two low-Ca-loading catalysts as clusters.

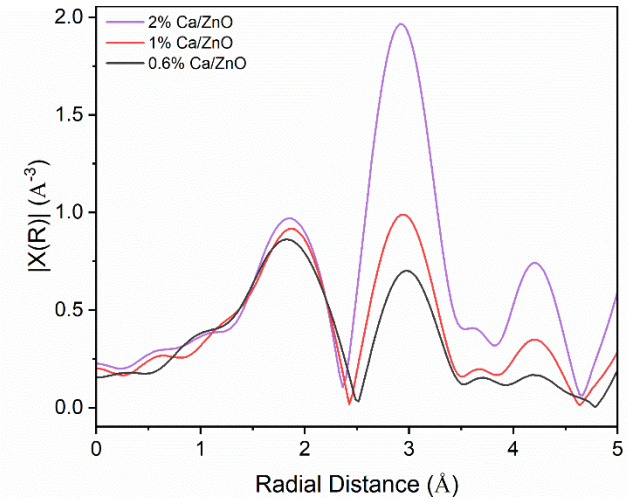

Figure 3.2. Magnitude of the Fourier transform of phase-uncorrected k^2-weighted EXAFS of low-Ca-loading Ca/ZnO catalysts using k-range of 3.4 to 9.1 Å^{-1}.

The two low-Ca-loading catalysts were modeled with the Ca-O and Ca-Ca scattering paths of bulk CaO. The Ca-O coordination was first allowed to float, but always converged to a value close to 6. In subsequent models, it was fixed to 6 to simply the model. This is a safe assumption since the first shell peak intensity in R-space is equivalent to the 2 mol% Ca/ZnO reference, and isolated Ca atoms have been reported to maintain a bulk Ca-O coordination number.[25] The fitting results are shown in Figure 3.3 and Table 3.1. The data of the high-Ca-loading catalysts are presented in R-, q-, and k-space in Figure S3.4 without fits. All fits result in oxygen and calcium distances associated with bulk CaO with little to no increases in the σ^2. The lack of difference in the Ca-O bond length supports a similar coordination number to that of bulk CaO.[42] This is consistent with reports that Ca nanostructures undergo negligible lattice distortion and maintain rigidity.[43,44] The Ca-Ca CNs are 5.9 ± 0.4 and 4.1 ± 0.7 for the 1 mol% and 0.6

mol% Ca/ZnO catalysts, respectively. These CN are significantly smaller than the bulk CaO Ca-Ca CN of 12, indicating that calcium exists as nanoparticles of decreasing size.[22,45] Structural disorder could also lead to a reduction of long-range coordination but would predominately influence the third and higher shells.[22] No influence of the ZnO support is observed in the EXAFS data. While the data can be fit with a Ca-Zn scattering path, the σ^2 and ΔE_0 values are large and make less chemical sense than of the model with only Ca-O and Ca-Ca scattering paths. Thus, models with Ca-Zn scattering paths are rejected. (Figures S3.5-6, Tables S3.3-4). Similarly, models of calcium hydroxide or mixtures of oxide and hydroxide were ruled out due to poor fitting of the data with large R-factor, σ^2, and ΔE_0 values (Figures S3.7-8, Tables S3.5-6).

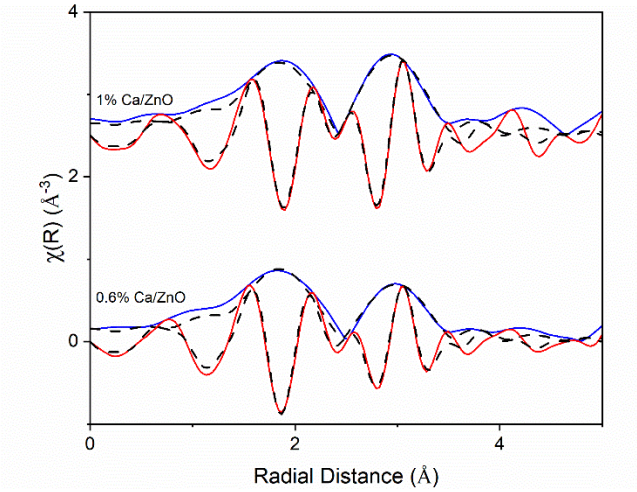

Figure 3.3. The magnitudes and imaginary portions of the k^2-weighted R-space functions for spectra associated with the low-Ca-loading catalysts are shown using solid blue and red lines, respectively; fits shown with dashed lines. The data were back Fourier transformed in the R-range of 1.0 to 3.5 Å and fit in the q-range of 3.4 to 9.1 $Å^{-1}$.

Table 3.1. Best fit of the EXAFS parameters for Ca/ZnO catalysts.

	Path	**N**	**R (Å)**	**σ^2 x 10^3 ($Å^2$)**	**ΔE_0 (eV)**	**R-Factor**	**S_0^2**
1% Ca/ZnO	Ca-O	6	2.37 ± 0.01	6.1 ± 1.6	0.8 ± 1.0	0.0111	0.73
	Ca-Ca	5.9 ± 0.4	3.41 ± 0.01	4.6			
0.6% Ca/ZnO	Ca-O	6	2.36 ± 0.02	6.7 ± 1.9	1.6 ± 1.8	0.0347	
	Ca-Ca	4.1 ± 0.7	3.42 ± 0.03	4.6			

Notation: N, coordination number; S_0^2, amplitude correction term; ΔE_0, energy correction factor; R, scattering path length; σ^2, disorder term. A *k*-range of 3.4-9.1 $Å^{-1}$ and R-range of 1.0-3.5 Å were used. Values without error bounds were held constant.

Computational Simulation of X-ray Absorption Spectra of Ca Nanoparticle Structures

Theoretical simulations of XANES spectra provide additional, complementary insight into the specific structures responsible for spectral features observed. The XANES spectra associated with the Ca/ZnO catalysts were simulated using FEFF10, as described in the Methods section. These simulations included consideration of CaO structures organized in multiple spatial arrangements, with separate analyses of Ca atoms in the surface and bulk of three geometries – linear, planar, and cubic – shown in insets of Figure 3.4. The spectrum of bulk CaO was simulated using a Ca atom surrounded by 6 and 7 full coordination layers for O and Ca, respectively. This system was used to find the best computational parameters for FEFF and to assess the quality of the XANES simulations for a system with known structure. The spectrum contains all major features found in the experimental spectrum (Figure S3.9). Using those parameters, the XANES of a Ca atom on the (100) surface of CaO was also calculated (Figure S3.10) and found to qualitatively reproduce all the characteristic differing features in the spectrum for a low-Ca-loading catalyst versus bulk CaO – decreased intensity of the shoulder, white line, and EXAFS oscillations, as well as increased intensity of a new pre-edge peak. The agreement between the spectrum for 0.6 mol% Ca/ZnO and that simulated for surface atoms supports the existence of clusters with a high fraction of exposed and undercoordinated Ca atoms. Computational investigations into the growth of $(CaO)_n$ nanoclusters found that cubic-like structures, including linear and planar geometries, were most favorable and stable.[44,46,47] Therefore, unrelaxed clusters with a range of sizes and Ca-Ca CNs were modeled in linear, planar, and cubic geometries (Figure S3.11). The unrelaxed structures provide a convenient, sound approximation because of the negligible differences in Ca-O bond distance and σ^2 between the experimental bulk CaO and low-Ca-loading EXAFS fits. The experimentally determined Ca-Ca CNs were 4.1 ± 0.7 and 5.9 ± 0.4 for 0.6 mol% Ca/ZnO and 1 mol% Ca/ZnO catalysts, respectively, which best correspond to linear and planar structures.

Figure S3.12 show the average theoretical spectra for each of these structures, compared to bulk CaO. Since the main objective is to determine the origin of differences between the low-Ca-loading systems

and bulk CaO, the difference spectrum (ΔXANES) between the 0.6 mol% Ca/ZnO catalyst and bulk CaO was generated – it provides a direct visualization of differences in each spectral region. This difference in experimental results was compared to the differences between the theoretical XANES of the linear, planar, and cubic CaO clusters and that of bulk CaO. To provide a more quantitative measure of agreement between theory and experiment, a normalized Frechet distance was calculated as a FOM (Table S3.7) for the complete theoretical energy range as well as individual ranges that characterize energy regions of importance – pre-edge, shoulder, white line, post-edge, and low EXAFS. The baseline accuracy of the theoretical spectra to the experimental spectra was assessed by applying the Frechet analysis to the experimental versus theoretical CaO bulk data. We find that the largest deviations between theory and experiment (Table S3.7, bottom) occur in the shoulder and white line regions of the spectra. This is likely due to the use of the muffin-tin potential approximation in FEFF. Therefore, these regions should be considered less relevant when assessing the ΔXANES results.

Visual inspection of the ΔXANES results shows the spectra generated from linear clusters ranging from 7.2 to 26.5 Å in length in Figure 3.4 agree most closely with the experimental spectra in the post-white line and low EXAFS regions, showing little difference for different cluster sizes. The longer linear clusters also give reasonable results in the shoulder region. However, all linear clusters display significant discrepancies relative to the experiment in the pre-edge and white line regions. The Frechet FOM supports this qualitative assessment, showing that the linear clusters provide the best quantitative results in the post-white line region and near-best results in the low EXAFS region. Despite the visual discrepancies in the white line region, the long linear clusters provide best results in these regions of all clusters studied. Similar agreement and discrepancies with respect to experiment are observed for the planar clusters with side length of 7.2 to 26.5 Å, but with slightly better agreement in the pre-edge and shoulder region (Figure 3.4b). Thus, these clusters provide the best overall agreement of all shapes and sizes simulated here. Simulated spectra for cubic clusters begin to resemble those of simulated and experimental bulk CaO, notably in the post-white line and EXAFS regions of the spectra (Figure 3.4c). Despite providing the best agreement in the pre-

edge region, discussed in more detail below, they show an overall less satisfactory agreement than spectra simulated based on the linear and planar structure. Thus, if present, they can be regarded as a minority species. In summary, this analysis suggests that simulated spectra generated from larger linear and planar structures agree best with experimental results. With this data, it is not possible to definitively conclude which of these structures with low dimensionality is the majority species present in these catalysts, since each produces spectra with similarities to experimental results in different spectral regions. Without privileging specific spectral regions in the assessment of structures, the results suggest that a mixture of these ultra-small supported one-dimensional and two-dimensional CaO clusters is likely.

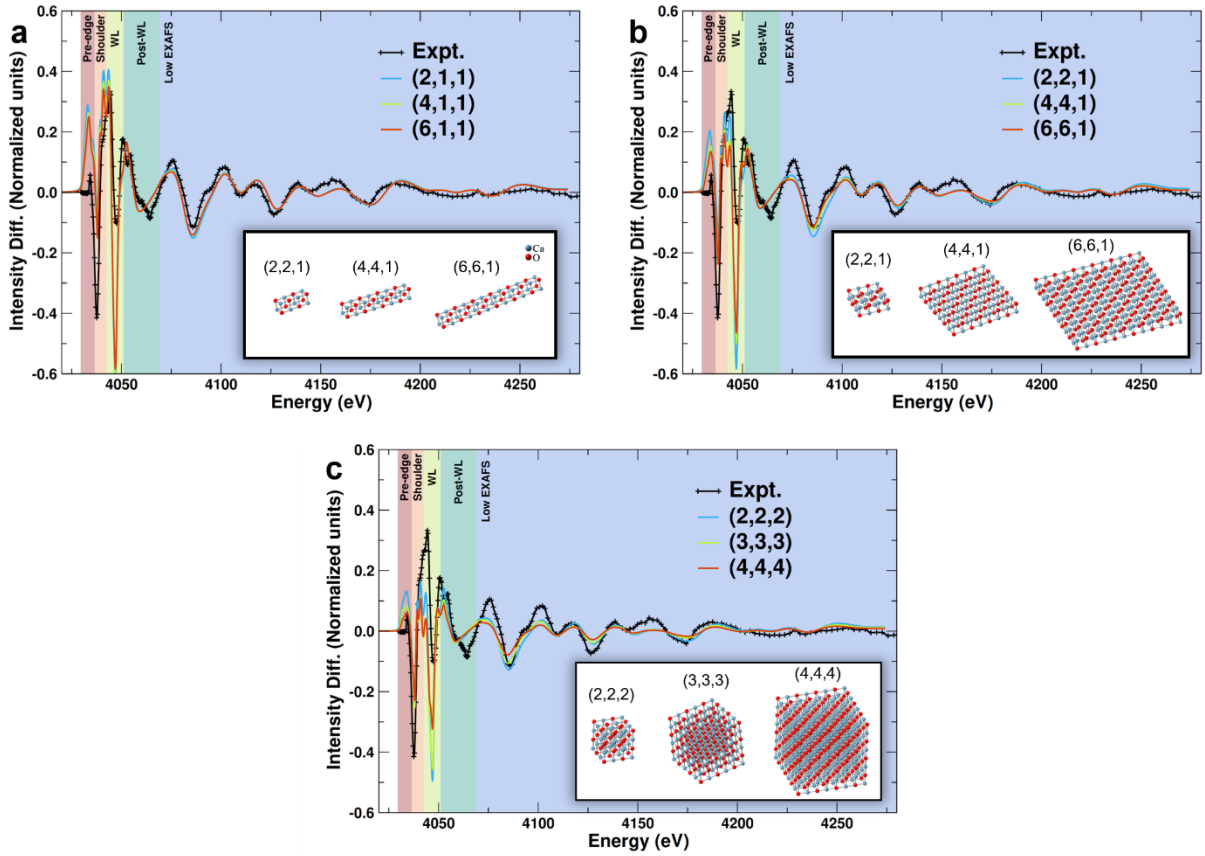

Figure 3.4. Difference between the experimental spectra of 0.6 mol% Ca/ZnO and CaO reference compared to the difference between simulated spectra of CaO nanoparticles of varying sizes and bulk CaO for the (b) linear, (c) planar, and (d) cubic morphologies. The numbers in parentheses represent the number of unit cells of each dimension.

The angular momentum decomposed local density of state (LDOS), shown in Figure 3.5, helps to qualitatively identify which electronic transitions contribute to each region of the spectra. Given the computational cost of the LDOS simulations, here we use the Ca on the surface as a proxy for the behavior of undercoordinated atoms in the clusters. In bulk CaO, the white line is dominated by transitions to Ca 4p states, in agreement with selection rules and previous assignments.[48] The shoulder and post-white line regions show clear Ca p – O p hybridization, reflecting oxygen ligation. No electronic transition in the pre-edge region is observed. The LDOS for a surface Ca atom demonstrates hybridization with oxygen p states in the shoulder and post-white line regions, as observed for bulk CaO, but also with much lower intensity. In the LDOS for surface Ca atoms, a pre-edge feature arising from Ca p states is found to exist, likely due to empty p states formed from reduced coordination. When the surface Ca atom is fully coordinated by the addition of a single oxygen atom (Figure 3.5c), the pre-edge feature disappears, likely due to the conversion and shift to higher energies of the empty p-like surface state into a σ* state associated with the new CaO bond. This pre-edge peak has been reported to be the Ca 1s to 3d transition of asymmetric clusters,[37,49] an assumption taken from the interpretation of 3d transition metals. However, Figure 3.5 demonstrates that the pre-edge can result from the Ca p states of undercoordinated surface Ca atoms. Simulations of the 1s to 3d transition required the activation of quadrupole transitions. Figure S3.13 deconvolute the influence of the 1s to p and 1s to d transition on the LDOS. The 1s to d transition has a negligible contribution to the rise of the pre-edge peak in the undercoordinated surface Ca atom. Geometric distortions around the central absorbing Ca atom do not increase the intensity of the 1s to d transition (Figures S3.13b,d,f). The LDOS and the weight of the quadrupole transitions suggest the pre-edge peak results from the empty Ca p states in undercoordinated Ca for the unrelaxed structures simulated here. This analysis of the pre-edge peak must be carefully reconciled with the fact that the EXAFS best fit is obtained with fully O-coordinated Ca. Therefore, it is possible that the too large pre-edge peaks observed for the linear and planar clusters compared to the experimental result is due to the presence of too-many undercoordinated atoms in these systems, and better results might be obtained by partially capping them. Altogether, computational analysis

of XANES data suggests that catalysts with 1 mol% Ca or less are comprised of ultra-small supported CaO clusters organized into linear and planar atomic structures with monolayer thickness.

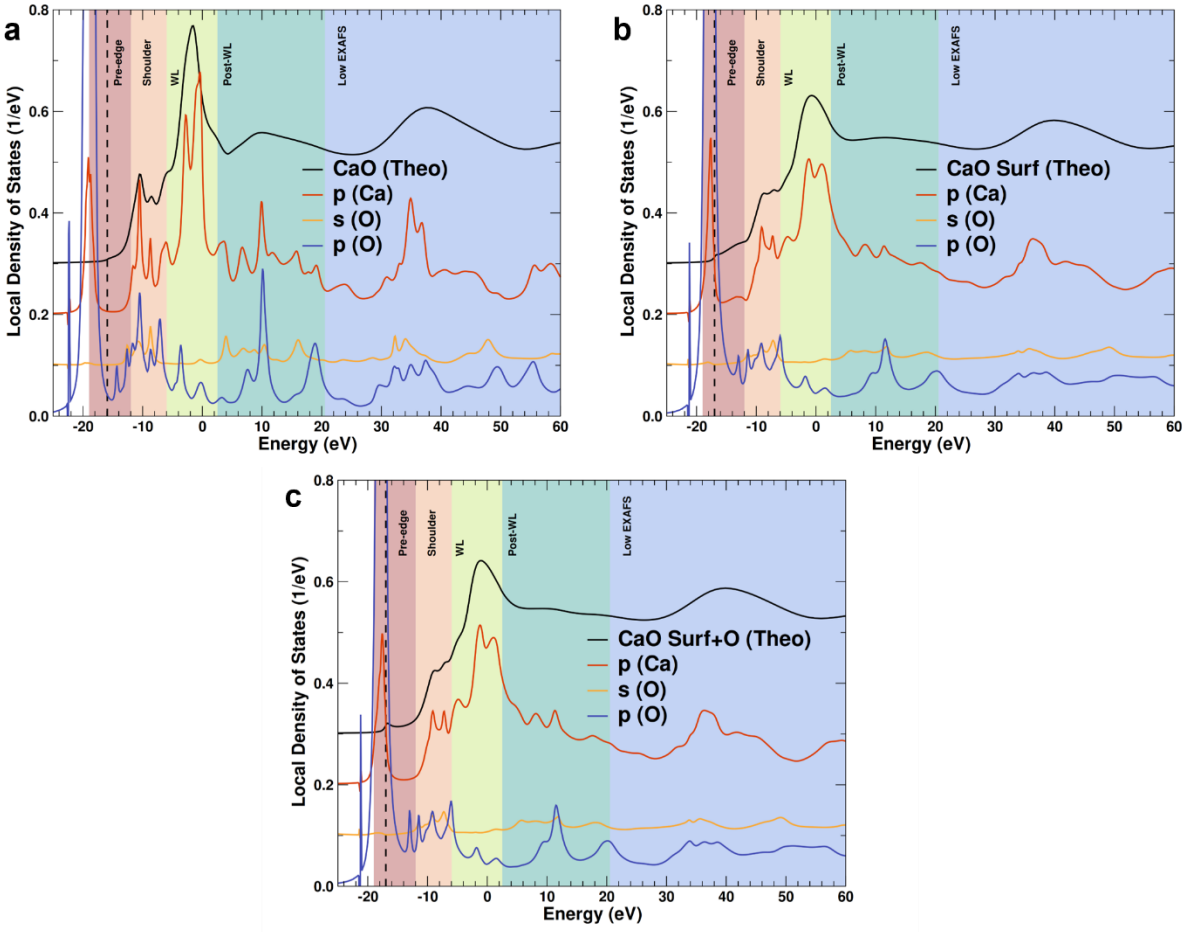

Figure 3.5. Projected local density of states for (a) bulk CaO, (b) surface Ca atom, and (c) oxygen-terminated surface Ca atom. Dotted line represents Fermi level.

Initial CaO Nanocluster Speciation Affects CO_2-OCM Performance

Evaluation of the CO_2-OCM performance of these catalysts, reported previously, showed that selectivity to methane coupling was significantly greater for catalysts with less than 2 mol% Ca compared with those with higher Ca loadings.[21] In the low-loading regime, increased Ca loading was associated with increased C_2 product yields. The further observation that the rate of methane coupling normalized by Ca loading was similar among low-loading samples suggested that in the low-loading regime, C_2 production rate increases with an increase in the number of interface sites between CaO and ZnO. At and above 2 mol% Ca loading,

further Ca addition only slows the production rate of C_2 species due to the formation of an inactive bulk CaO phase. Characterization revealed that the low loading catalysts were electronically distinct from bulk CaO, likely due to increased interaction with ZnO.[21]

The XAS results reported here validate the previous hypothesis that the Ca species present in the low loading catalysts are highly dispersed as ultra-small clusters. As Ca loading increases, the cluster size becomes slightly larger. Increasing the size of linear and planar CaO structures decreases the amount of the exposed ZnO surface, blocking sites unselective to coupling and creating new, highly selective interfacial sites. For an equivalent number of atoms, the fraction of CaO-ZnO interfacial atomic sites is considerably higher for linear and planar structures than for the cubic structure. The undercoordinated Ca species present in the clusters, as suggested to exist by the presence of the pre-edge feature, may also serve as selective methane coupling sites independent of the ZnO interaction.[50,51]

Relating Ca Structure to N_2O-OCM Performance and Kinetics

The Ca/ZnO catalysts with varying Ca loadings were evaluated in this study for their N_2O-assisted methane coupling (N_2O-OCM) activity, which complements prior catalysis results reported for CO_2-OCM.[21] As was observed for CO_2-OCM catalysis, it is revealed that there are two regimes of catalytic activity, defined by Ca loading: below 2 mol% Ca, where C_2 product selectivity is 39%, and higher Ca-loadings, where C_2 product selectivity decreases with Ca loading to only 3% over CaO. The transition between these two catalytic regimes correlates to the changes in Ca structure observed by XAS. The catalysts with low-Ca-loading that display higher selectivity to C_2 products were found to have ultra-small linear and planar CaO clusters, while the less selective catalysts have bulk CaO phases. The distinct activity in the low-loading regime is reflected in Figure 3.6 by the increase in both selectivity and yield of C_2 products between 0.2 mol% and 0.6 mol% Ca loading; this is the same composition range where maximum C_2 products formed during CO_2-OCM.[21] At the lowest Ca loading examined, 0.2 mol%, the presence of Ca on the surface had only a minor influence on N_2O-OCM catalysis. However, further addition of linear/planar CaO structures can quickly cover the catalyst surface with selective sites, reflected in the strong influence of loading on performance. Normalizing the activity shown in Figure 3.6 of the supported cluster catalysts by the mass

of Ca, as determined by ICP, results in normalized C_2 product yields of 98 and 35 mmol/h/g_{Ca} over the 1 mol% Ca/ZnO and 0.6 mol% Ca/ZnO catalysts, respectively. The low dimensionality of the CaO clusters suggests that nearly all Ca atoms are surface-exposed. The normalized C_2 product yield decreases as the cluster size become larger, likely due to the undercoordinated Ca concentration decreasing with increasing cluster size, represented by the decreasing pre-edge feature. C_{3+} selectivities and yields trend with those of C_2 products. These higher hydrocarbons are likely secondary products formed by further coupling of C_2 species.[52] Catalysts with ≥35 mol% Ca where large, bulk CaO particles exist, have reduced methane coupling performance with increasing loading, and partial or complete combustion to CO_x is favored with increasing loading (Table S3.8); activity resembles that of pure CaO at the highest loadings.[50,53] The trends of selectivity and product yields for N_2O-OCM are strongly correlated, suggesting that methane oxidation is in direct competition with methane coupling (presumably with the release of methyl radicals[54]) over these catalysts, an observation that is in contrast with findings from CO_2-OCM catalysis, where bulk CaO phases were inactive due to stable carbonate formation.

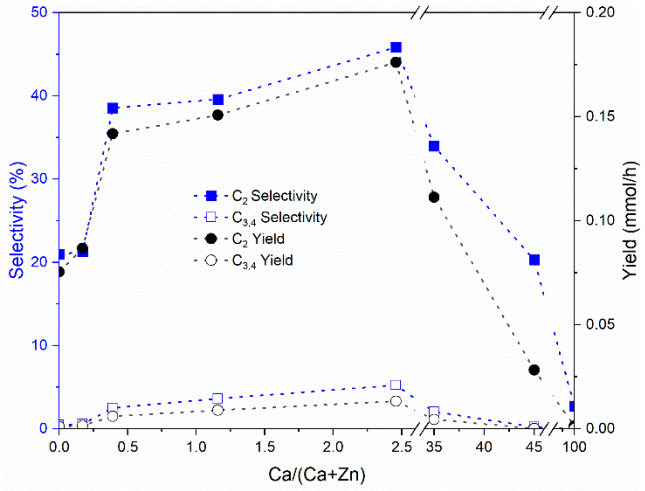

Figure 3.6. Effects of Ca loading on C_{2+} selectivity (■) and C_{2+} yield (●). Reaction conditions: 550 °C; 0.75 g catalyst; 13.3 mL min^{-1} total gas flow rate with P_{CH_4} = 0.23 atm, P_{N_2O} = 0.45 atm, P_{Ar} = 0.32 atm; 7 h on stream. All Ca loadings are reported in molar concentration of metal cations, as determined by ICP-OES (Table S3.1). All reactant conversions and product yields are reported in Table S3.8. Dotted lines are included to guide the eye.

Analyses of results from XAS and reactor studies establish that there are distinct regimes of both CaO structure and catalytic activity as Ca loading is varied. The impact of the two structural and catalytic regimes – methane coupling-selective small CaO clusters and unselective bulk CaO particles – on reaction kinetics was further studied by comparing the activation energies of 1 mol% Ca/ZnO and 35 mol% Ca/ZnO (Figure 3.7). Plots of reactant conversion and product yields versus inverse space velocity in Figure S3.14 confirm the reactor is operating in the differential regime. The activation energies for ethane formation, the primary product of methane coupling, are 183 ± 1.9 kJ/mol and 256 ± 9.8 kJ/mol for 1 mol% Ca/ZnO and 35 mol% Ca/ZnO, respectively. The energy of 183 kJ/mol is in good agreement with that previously reported for a similar reactant composition over Li/MgO, where oxygen incorporation from N_2O to the catalyst surface was determined to be the rate-determining step.[52] The significantly larger E_a of 35 mol% Ca/ZnO suggests either a different active site structure, a change in the rate-determining step, or both. The initial CaO structure differs based on the XAS results here, with undercoordinated Ca sites in 1-2D clusters only existing in the low-Ca-loading catalysts. For basic metal oxide catalysts, the presence of CO_2 from reaction products can inhibit methane coupling, shifting the E_a to higher energy due to the formation of carbonate species.[51,52,55] Carbonate can poison CaO active sites and will require higher temperatures to desorb on the high-Ca-loading Ca/ZnO catalysts.[21] Therefore, it is likely that the higher E_a in the catalyst with a bulk CaO phase is due to a different active site structure that has a different rate-determining step than the structure present in 1 mol% Ca/ZnO.

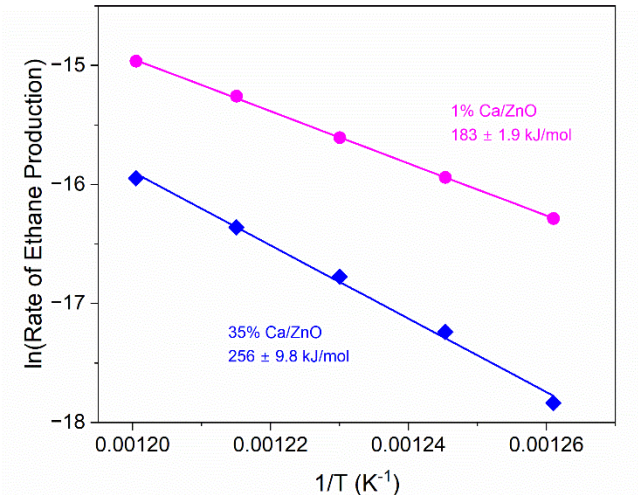

Figure 3.7. Comparison of methane coupling to ethane activation energies over 1 mol% Ca/ZnO and 35 mol% Ca/ZnO: 200 mg catalyst, total flow of 30 mL/min, methane:N_2O:argon feed ratio of 1:2:1, temperature range of 520 °C to 560 °C. Error calculated from linear fit.

Bulk CaO is very effective at N_2O decomposition to N_2 and O_2.[56–58] N_2O decomposition rates are completely unaffected by the presence of methane over CaO,[59] supporting our finding that bulk CaO does not perform N_2O-OCM but facilitates N_2O decomposition and secondary oxidation reactions. During N_2O decomposition, surface oxygen species are formed as intermediates in the reaction path leading to desorbed O_2.[60,61] Various adsorbed oxygen species have been found responsible for the overoxidation of methane and hydrocarbon products during OCM.[62,63] The surface species formed on CaO during N_2O decomposition likely interact strongly with the hydrocarbons present, leading to eventual oxidation. Gas-phase oxidation to CO_x species can also occur via $CH_3\bullet$ oxidation by molecular O_2.[64] Therefore, the ethane observed to be generated over 35 mol% Ca/ZnO is likely a result of the reaction occurring at interfacial sites between CaO and ZnO.

The generation of CO_2 leads to the formation of a stable $CaCO_3$ phase at reaction temperature.[51] While CaO is still the dominant phase in Ca/ZnO catalysts after N_2O-OCM, the carbonate phase can be observed by XRD on all catalysts with ≥1 mol% Ca content after N_2O-OCM (Figure S3.15). However, pure CaO seems to convert mostly to carbonate. $CaCO_3$ is a poor N_2O decomposition catalyst.[65] This may be due to the inhibition of surface O_2^- generation.[66] Figure S3.16 compares the activity of CaO and $CaCO_3$. The

conversion of N_2O over CaO is initially 100% and gradually decreases with time on stream, likely as carbonate surface species form. The steady state C_2 product selectivity over CaO and $CaCO_3$ are 3% and 14%, respectively. Calcium carbonate formation on bulk CaO therefore does not significantly improve the methane coupling performance but inhibits N_2O decomposition. Higher C_2 product selectivities are observed over ZnO-supported CaO clusters than over bulk CaO or $CaCO_3$ catalysts. While carbonate deposition likely occurs on supported CaO clusters during reaction, these catalysts maintain their enhanced methane coupling performance relative to bulk CaO. Neither the rate of carbonate deposition nor any potential *in situ* evolution of CaO during reaction are studied here. All results presented herein indicate the presence of a relationship between the microstructural environment of ZnO-supported Ca in the synthesized catalysts and activity toward methane coupling with the alternative oxidants N_2O and CO_2.

3.5 Conclusion

This work investigates the local physical and electronic structures of Ca in ZnO-supported CaO soft oxidant-assisted methane coupling catalysts through Ca K-edge XANES and EXAFS. XANES results have been interpreted through simulated spectra derived from *ab initio* multiple scattering calculations (FEFF), which elucidates the structural correlates of sites that are active for methane coupling. Results show that below 2 mol% Ca loading, the Ca sites exist as CaO clusters organized as one-dimensional and two-dimensional structures with approximately one atomic layer thickness. The Ca-Ca coordination numbers derived from EXAFS data suggest that the size of these clusters is approximately 7.2 to 26.5 Å. The simulated spectrum of a surface Ca atom matches well with the experimental spectrum measured for the low-Ca-loading catalysts. An increasing pre-edge intensity with decreasing Ca loading indicates the presence of undercoordinated surface Ca atoms, according to local densities of states calculations. Catalysts containing these low-dimensional CaO clusters yield enhanced CO_2- and N_2O-assisted methane coupling activity when compared with catalysts containing CaO particles with bulk properties. Significantly different activation energies for ethane formation over 1 mol% Ca/ZnO and 35 mol% Ca/ZnO catalysts are observed (183 ± 1.9 kJ/mol and 256 ± 9.8 kJ/mol, respectively), which is attributed to observed differences in active site structure and carbonate stability. These results suggest that future investigation of this system should

involve *in situ* characterization of the Ca speciation during reactions to probe the significance and influence of carbonate formation on reactivity. These results provide fundamental insights into the active site structure of binary metal oxide catalysts, which contributes to optimization of C_2 product yields during soft oxidant-assisted methane coupling.

3.6 Acknowledgements

L. R. F. and C. X. K. acknowledge support by the U.S. Department of Energy (DOE), Office of Basic Energy Sciences (BES), Division of Chemical Sciences, Geosciences and Biosciences (CSGB), Gas Phase Chemical Physics and Catalysis Science Programs, under grant DE-SC0020320. Co-ACCESS is supported by the U.S. Department of Energy, Office of Basic Energy Sciences, Chemical Sciences, Geosciences and Biosciences Division. Use of the Stanford Synchrotron Radiation Lightsource, SLAC National Accelerator Laboratory, is supported by the U.S. Department of Energy, Office of Science, Office of Basic Energy Sciences under Contract No. DE-AC02-76SF00515. The theoretical XANES simulations used resources of the National Energy Research Scientific Computing Center (NERSC), a U.S. Department of Energy Office of Science User Facility located at Lawrence Berkeley National Laboratory, operated under contract no. DE-AC02-05CH11231 using NERSC award ERCAP0023078. We thank all graduate student members of the UC Davis catalysis cluster that assisted in XAS data collection.

3.7 References

(1) Howarth, R. W. Methane Emissions and Climatic Warming Risk from Hydraulic Fracturing and Shale Gas Development: Implications for Policy. Energy Emiss. Control Technol. 2015, 3, 45–54.

(2) Franz, R.; Uslamin, E. A.; Pidko, E. A. Challenges for the Utilization of Methane as a Chemical Feedstock. Mendeleev Commun. 2021, 31 (5), 584–592.

(3) Chen, W.; Duan, X.; Zhou, X.; Chen, D. Design and Tailoring of Advanced Catalytic Process for Light Alkanes Upgrading. EcoMat 2021, 3 (2), e12095.

(4) Horn, R.; Schlögl, R. Methane Activation by Heterogeneous Catalysis. Catal. Lett. 2015, 145 (1), 23–39.

(5) Ortiz-Bravo, C. A.; Chagas, C. A.; Toniolo, F. S. Oxidative Coupling of Methane (OCM): An Overview of the Challenges and Opportunities for Developing New Technologies. J. Nat. Gas Sci. Eng. 2021, 96, 104254.

(6) Ghose, R.; Hwang, H. T.; Varma, A. Oxidative Coupling of Methane Using Catalysts Synthesized by Solution Combustion Method: Catalyst Optimization and Kinetic Studies. Appl. Catal. A: Gen. 2014, 472, 39–46.

(7) Cruellas, A.; Bakker, J. J.; van Sint Annaland, M.; Medrano, J. A.; Gallucci, F. Techno-Economic Analysis of Oxidative Coupling of Methane: Current State of the Art and Future Perspectives. Energy Convers. Manag. 2019, 198, 111789.

(8) Aika, K. I.; Nishiyama, T. Utilisation of CO_2 in the Oxidative Coupling of Methane over PbO-MgO and PbO-CaO. J. Chem. Soc., Chem. Commun. 1988, No. 1, 70–71.

(9) Ayodele, B. V.; Mustapa, S. I.; Witoon, T.; Kanthasamy, R.; Zwawi, M.; Owabor, C. N. Radial Basis Function Neural Network Model Prediction of Thermo-Catalytic Carbon Dioxide Oxidative Coupling of Methane to C_2-Hydrocarbon. Top Catal. 2020, 64, 328–337.

(10) Hutchings, G. J.; Scurrell, M. S.; Woodhouse, J. R. The Role of Surface O^- in the Selective Oxidation of Methane. J. Chem. Soc., Chem. Commun. 1987, No. 18, 1388–1389.

(11) Aydin, Z.; Zanina, A.; Kondratenko, V. A.; Rabeah, J.; Li, J.; Chen, J.; Li, Y.; Jiang, G.; Lund, H.; Bartling, S.; Linke, D.; Kondratenko, E. V. Effects of N_2O and Water on Activity and Selectivity in the Oxidative Coupling of Methane over Mn-Na_2WO_4/SiO_2: Role of Oxygen Species. ACS Catal. 2022, 12 (2), 1298–1309.

(12) Istadi; Amin, N. A. S. Synergistic Effect of Catalyst Basicity and Reducibility on Performance of Ternary CeO_2-Based Catalyst for CO_2-OCM to C_2 Hydrocarbons. J. Mol. Catal. A Chem 2006, 259, 61–66.

(13) Wang, Y.; Ohtsuka, Y. CaO-ZnO Catalyst for Selective Conversion of Methane to C_2 Hydrocarbons Using Carbon Dioxide as the Oxidant. J. Catal. 2000, 192 (1), 252–255.

(14) Wang, Y.; Takahashi, Y.; Ohtsuka, Y. Carbon Dioxide as Oxidant for the Conversion of Methane to Ethane and Ethylene Using Modified CeO_2 Catalysts. J. Catal. 1999, 186 (1), 160–168.

(15) Asami, K.; Fujita, T.; Nishiyama, Y.; Ohtsuka, Y. Formation of Ethane and Ethylene from Methane and Carbon Dioxide over Manganese Oxide Catalysts. J. Jpn. Pet. Inst. 1996, 39 (2), 137–143.

(16) Asami, K.; Fujita, T.; Kusakabe, K.-I.; Nishiyama, Y.; Ohtsuka, Y. Conversion of Methane with Carbon Dioxide into C_2 Hydrocarbons over Metal Oxides. Appl. Catal. A: Gen. 1995, 126 (2), 245–255.

(17) Cai, Y.; Chou, L.; Li, S.; Zhang, B.; Zhao, J. Selective Conversion of Methane to C_2 Hydrocarbons Using Carbon Dioxide over Mn-$SrCO_3$ Catalysts. Catal. Lett. 2003, 86 (4), 191–195.

(18) Wang, Y.; Zhuang, Q.; Takahashi, Y.; Ohtsuka, Y. Remarkable Enhancing Effect of Carbon Dioxide on the Conversion of Methane to C_2 Hydrocarbons Using Praseodymium Oxide. Catal. Lett. 1998, 56, 203–206.

(19) Litawa, B.; Michorczyk, P.; Ogonowski, J. Influence of CO_2 on the Catalytic Performance of La_2O_3 /CeO_2 and CaO/CeO_2 Catalysts in the Oxidative Coupling of Methane. Pol. J. Chem. Technol. 2013, 15 (1), 22–26.

(20) Ferreira, A. C.; Gasche, T. A.; Leal, J. P.; Branco, J. B. Methane Activation with Nitrous Oxide over Bimetallic Oxide Ca-Lanthanide Nanocatalysts. Mol. Catal. 2017, 443, 155–164.

(21) Filardi, L. R.; Yang, F.; Guo, J.; Kronawitter, C. X.; Runnebaum, R. C. Surface Basicity Controls C–C Coupling Rates during Carbon Dioxide-Assisted Methane Coupling over Bifunctional Ca/ZnO Catalysts. Phys. Chem. Chem. Phys. 2023, 25 (14), 9859–9867.

(22) Chen, L. X.; Rajh, T.; Wang, Z.; Thurnauer, M. C. XAFS Studies of Surface Structures of TiO_2 Nanoparticles and Photocatalytic Reduction of Metal Ions. J. Phys. Chem. B 1997, 101, 10688–10697.

(23) Romanchuk, A.; Trigub, A.; Plakhova, T.; Kuzenkova, A.; Svetogorov, R.; Kvashnina, K.; Kalmykov, S. Effective Coordination Numbers from EXAFS: General Approaches for Lanthanide and Actinide Dioxides. J. Synchrotron Radiat. 2022, 29 (Pt 2), 288–294.

(24) Karim, A. M.; Prasad, V.; Mpourmpakis, G.; Lonergan, W. W.; Frenkel, A. I.; Chen, J. G.; Vlachos, D. G. Correlating Particle Size and Shape of Supported $Ru/\gamma\text{-}Al_2O_3$ Catalysts with NH_3 Decomposition Activity. J. Am. Chem. Soc. 2009, 131 (34), 12230–12239.

(25) Yamashita, H.; Nomura, M.; Tomita, A. Local Structures of Metals Dispersed on Coal. 4. Local Structure of Calcium Species on Coal after Heat Treatment and CO_2 Gasification. Energy Fuels 1992, 6 (5), 656–661.

(26) Huggins, F. E.; Huffman, G. P.; Shah, N.; Jenkins, R. G.; Lytle, F. W.; Greegor, R. B. Further EXAFS Examination of the State of Calcium in Pyrolysed Char. Fuel 1988, 67 (7), 938–941.

(27) Okasinski, J.; Cohen, J. B.; Hwang, J.; Mason, T. O.; Ding, Z.; Warschkow, O.; Ellis, D. E. Defect and Electronic Structures of Calcium-Doped Lanthanum Cuprate. J. Am. Ceram. Soc. 1999, 82 (9), 2451–2459.

(28) Liou, S.-C.; Chen, S.-Y.; Lee, H.-Y.; Bow, J.-S. Structural Characterization of Nano-Sized Calcium Deficient Apatite Powders. Biomater. 2004, 25 (2), 189–196.

(29) Qiao, L.; Zizak, I.; Zaslansky, P.; Ma, Y. The Crystallization Process of Vaterite Microdisc Mesocrystals via Proto-Vaterite Amorphous Calcium Carbonate Characterized by Cryo-X-Ray Absorption Spectroscopy. Crystals 2020, 10 (9), 750.

(30) Mirghiasi, Z.; Bakhtiari, F.; Darezereshki, E.; Esmaeilzadeh, E. Preparation and Characterization of CaO Nanoparticles from $Ca(OH)_2$ by Direct Thermal Decomposition Method. J. Ind. Eng. Chem. 2014, 20 (1), 113–117.

(31) Ravel, B.; Newville, M. ATHENA, ARTEMIS, HEPHAESTUS: Data Analysis for X-Ray Absorption Spectroscopy Using IFEFFIT. J. Synchrotron Radiat. 2005, 12 (4), 537–541.

(32) Jain, A.; Ong, S. P.; Hautier, G.; Chen, W.; Richards, W. D.; Dacek, S.; Cholia, S.; Gunter, D.; Skinner, D.; Ceder, G.; Persson, K. A. Commentary: The Materials Project: A Materials Genome Approach to Accelerating Materials Innovation. APL Mater. 2013, 1 (1), 11002.

(33) Rehr, J. J.; Kas, J. J.; Prange, M. P.; Sorini, A. P.; Takimoto, Y.; Vila, F. Ab Initio Theory and Calculations of X-Ray Spectra. C. R. Phys. 2009, 10 (6), 548–559.

(34) Rehr, J. J.; Kas, J. J.; Vila, F. D.; Prange, M. P.; Jorissen, K. Parameter-Free Calculations of X-Ray Spectra with FEFF9. Phys. Chem. Chem. Phys. 2010, 12 (21), 5503–5513.

(35) Kas, J. J.; Vila, F. D.; Pemmaraju, C. D.; Tan, T. S.; Rehr, J. J. Advanced Calculations of X-Ray Spectroscopies with FEFF10 and Corvus. J. Synchrotron Radiat. 2021, 28 (6), 1801–1810.

(36) Ralph W. G. Wyckoff. Crystal Structures, 2nd ed.; Interscience Publishers / John Wiley & Sons: New York, 1963; Vol. 1.

(37) Eichert, D.; Salomé, M.; Banu, M.; Susini, J.; Rey, C. Preliminary Characterization of Calcium Chemical Environment in Apatitic and Non-Apatitic Calcium Phosphates of Biological Interest by X-Ray Absorption Spectroscopy. Spectrochim. Acta B 2005, 60 (6), 850–858.

(38) Asokan, K.; Jan, J. C.; Chiou, J. W.; Pong, W. F.; Tseng, P. K.; Lin, I. N. X-Ray Absorption Spectroscopy Studies of $Ba_{1-x}Ca_xTiO_3$. J. Synchrotron Radiat. 2001, 8, 839–841.

(39) Chakraborty, D.; Smitshuysen, T. E. L.; Kakekhani, A.; Jespersen, S. P. F.; Banerjee, S.; Krabbe, A.; Hagen, N.; Silva, H.; Just, J.; Damsgaard, C. D.; Helveg, S.; Rappe, A. M.; Nørskov, J. K.; Chorkendorff, I. Reversible Atomization and Nano-Clustering of Pt as a Strategy for Designing Ultra-Low-Metal-Loading Catalysts. J. Phys. Chem. C 2022, 126 (38), 16194–16203.

(40) Tröger, L.; Arvanitis, D.; Baberschke, K.; Michaelis, H.; Grimm, U.; Zschech, E. Full Correction of the Self-Absorption in Soft-Fluorescence Extended X-Ray-Absorption Fine Structure. Phys. Rev. B 1992, 46 (6), 3283–3289.

(41) Jalilehvand, F.; Spångberg, D.; Lindqvist-Reis, P.; Hermansson, K.; Persson, I.; Sandström, M. Hydration of the Calcium Ion. An EXAFS, Large-Angle X-Ray Scattering, and Molecular Dynamics Simulation Study. J. Am. Chem. Soc. 2001, 123 (3), 431–441.

(42) Sowrey, F. E.; Skipper, L. J.; Pickup, D. M.; Drake, K. O.; Lin, Z.; Smith, M. E.; Newport, R. J. Systematic Empirical Analysis of Calcium-Oxygen Coordination Environment by Calcium K-Edge XANES. Phys. Chem. Chem. Phys. 2004, 6, 188–192.

(43) Batra, P.; Gaba, R.; Issar, U.; Kakkar, R. Structures and Stabilities of Alkaline Earth Metal Oxide Nanoclusters: A DFT Study. J. Theor. Chem. 2013, 2013, 1–14.

(44) Malliavin, M.-J.; Coudray, C. Ab Initio Calculations on $(MgO)_n$, $(CaO)_n$, and $(NaCl)_n$ Clusters (n=1-6). J. Chem. Phys. 1997, 106 (6), 2323–2330.

(45) Moscovici, J.; Michalowicz, A.; Decker, S.; Lagadic, I.; Latreche, K.; Klabunde, K. Alkaline Earth Oxide Nanoparticles as Destructive Absorbents for Environmental Toxins. J. Synchrotron Radiat. 1999, 6, 604–606.

(46) Bawa, F.; Panas, I. Competing Pathways for MgO, CaO, SrO, and BaO Nanocluster Growth. Phys. Chem. Chem. Phys. 2002, 4 (1), 103–108.

(47) Aguado, A.; López, J. M. Structures and Stabilities of CaO and MgO Clusters and Cluster Ions: An Alternative Interpretation of the Experimental Mass Spectra. J. Phys. Chem. B 2000, 104 (35), 8398–8405.

(48) Chaboy, J.; Quartieri, S. X-Ray Absorption at the Ca K Edge in Natural-Garnet Solid Solutions: A Full-Multiple-Scattering Investigation. Phys. Rev. B 1995, 52 (9), 6349–6357.

(49) Martin-Diaconescu, V.; Gennari, M.; Gerey, B.; Tsui, E.; Kanady, J.; Tran, R.; Pécaut, J.; Maganas, D.; Krewald, V.; Gouré, E.; Duboc, C.; Yano, J.; Agapie, T.; Collomb, M.-N.; DeBeer, S. Ca K-Edge XAS as a Probe of Calcium Centers in Complex Systems. Inorg. Chem. 2015, 54 (4), 1283–1292.

(50) Roguleva, V. G.; Kondratenko, E. V.; Maksimov, N. G.; Selyutin, G. E.; Anshits, A. G. The Influence of the Reaction Medium of Oxidative Methane Coupling on the Nature of Bulk Defects of the Li/CaO System. Catal. Lett. 1992, 16 (1), 165–171.

(51) Thum, L.; Rudolph, M.; Schomäcker, R.; Wang, Y.; Tarasov, A.; Trunschke, A.; Schlögl, R. Oxygen Activation in Oxidative Coupling of Methane on Calcium Oxide. J. Phys. Chem. C 2019, 123 (13), 8018–8026.

(52) Yamamoto, H.; Chu, H. Y.; Xu, M.; Shi, C.; Lunsford, J. H. Oxidative Coupling of Methane over a Li^+/MgO Catalyst Using N_2O as an Oxidant. J. Catal. 1993, 142 (1), 325–336.

(53) Roguleva, V. G.; Nikiphorova, M. A.; Maksimov, N. G.; Anshits, A. G. Oxidative Coupling of Methane over Li/CaO Catalysts Using O_2 and N_2O as Oxidants. Catal. Today 1992, 13 (2), 219–226.

(54) Driscoll, D. J.; Martir, W.; Wang, J. X.; Lunsford, J. H. Formation of Gas-Phase Methyl Radicals Over MgO. J. Am. Chem. Soc. 1985, 107 (1), 58–63.

(55) Guan, C.; Liu, Z.; Wang, D.; Zhou, X.; Pang, Y.; Yu, N.; van Bavel, A. P.; Vovk, E.; Yang, Y. Exploring the Formation of Carbonates on La_2O_3 Catalysts with OCM Activity. Catal. Sci. Technol. 2021, 11 (19), 6516–6528.

(56) Snis, A.; Miettinen, H. Catalytic Decomposition of N_2O on CaO and MgO: Experiments and Ab Initio Calculations. J. Phys. Chem. B 1998, 102 (14), 2555–2561.

(57) Hu, X.; Wu, L.; Ju, S.; Dong, C.; Yang, Y.; Qin, W. Mechanistic Study of Catalysis on the Decomposition of N_2O. Environ. Eng. Sci. 2014, 31 (6), 308–316.

(58) Wu, L.; Hu, X.; Qin, W.; Dong, C.; Yang, Y. Effect of Sulfation on the Surface Activity of CaO for N_2O Decomposition. Appl. Surf. Sci. 2015, 357, 951–960.

(59) Satsuma, A.; Maeshima, H.; Watanabe, K.; Suzuki, K.; Hattori, T. Effects of Methane and Oxygen on Decomposition of Nitrous Oxide over Metal Oxide Catalysts. Catal. Today 2000, 63 (2–4), 347–353.

(60) Karlsen, E. J.; Nygren, M. A.; Pettersson, L. G. M. Theoretical Study on the Decomposition of N_2O over Alkaline Earth Metal-Oxides: MgO-BaO. J. Phys. Chem. A 2002, 106 (34), 7868–7875.

(61) Tench, A. J.; Lawson, T.; Kibblewhite, J. F. J. Oxygen Species Adsorbed on Oxides Part 1.-Formation and Reactivity of $(O^-)_s$ on MgO. J. Chem. Soc., Faraday Trans. 1 1972, 68, 1169–1180.

(62) Lin, C.-H.; Campbell, K. D.; Wang, J.-X.; Lunsford, J. H. Oxidative Dimerization of Methane over Lanthanum Oxide. J. Phys. Chem. 1986, 90 (4), 534–537.

(63) Peil, K. P.; Goodwin, J. G.; Marcelin, G. Surface Phenomena during the Oxidative Coupling of Methane over Li/MgO. J. Catal. 1991, 131 (1), 143–155.

(64) Karakaya, C.; Zhu, H.; Zohour, B.; Senkan, S.; Kee, R. J. Detailed Reaction Mechanisms for the Oxidative Coupling of Methane over La_2O_3/CeO_2 Nanofiber Fabric Catalysts. ChemCatChem 2017, 9 (24), 4538–4551.

(65) Hansen, P. F. B.; Dam-Johansen, K.; Johnsson, J. E.; Hulgaard, T. Catalytic Reduction of NO and N_2O on Limestone during Sulfur Capture under Fluidized Bed Combustion Conditions. Chem. Eng. Sci. 1992, 47 (9–11), 2419–2424.

(66) Yang, T.; Feng, L.; Shen, S. Oxygen Species on the Surface of La_2O_3/CaO and Its Role in the Oxidative Coupling of Methane. J. Catal. 1994, 145 (2), 384–389.

3.8 Supporting Information

Supporting Information Table of Contents

Table S3.1. Calcium concentration determined from ICP-OES.

Labeled mol%	**ICP Quantification mol%**	**ICP Quantification wt%**
0.2%	0.17	0.084
0.4%	0.39	0.193
0.6%	0.58	0.287
1%	1.33	0.659
2%	2.4	1.23
35%	34.5	19.0
45%	45.4	26.0

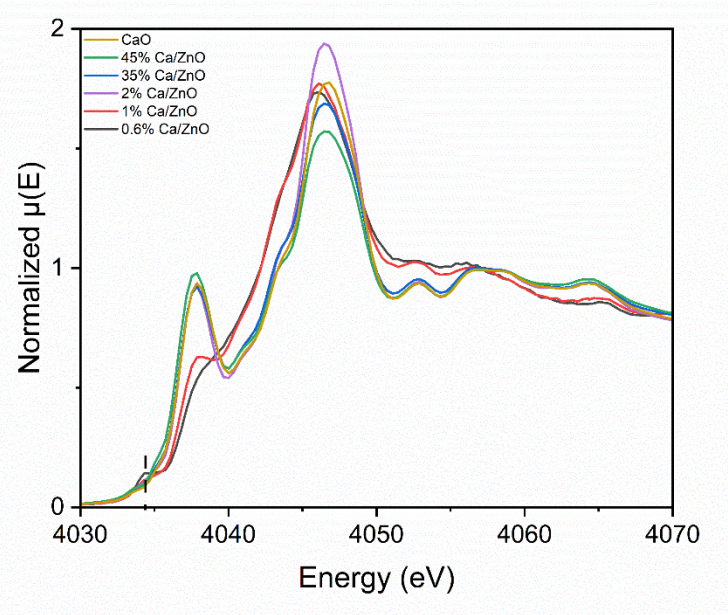

Figure S3.1. *Ex situ* Ca K-edge XANES spectra characterizing Ca/ZnO catalysts of varying composition collected at room temperature in He. Dashed line to visualize pre-edge feature.

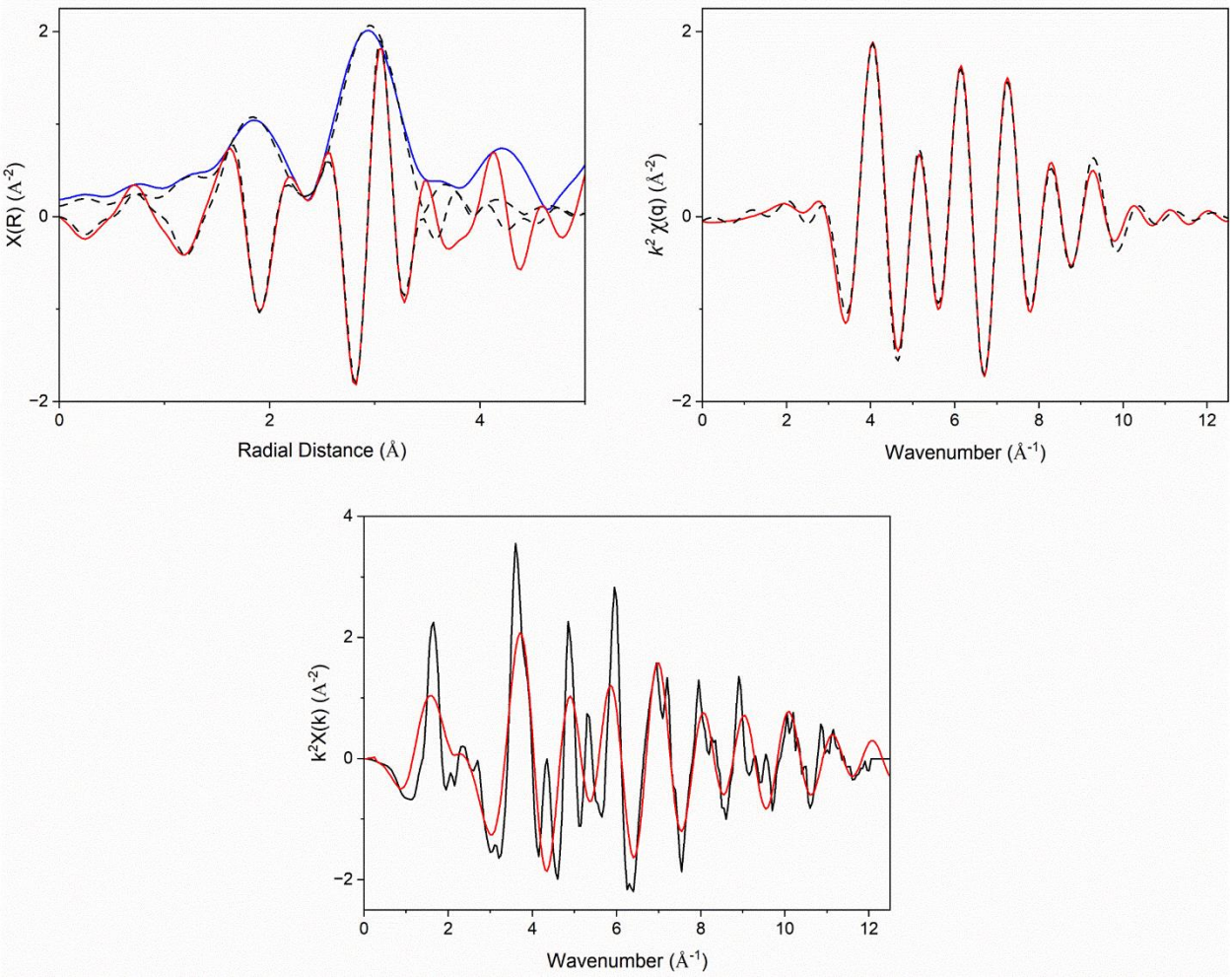

Figure S3.2. The magnitude (blue) and imaginary (red) portion of the k^2-weighted Fourier transforms of the EXAFS spectra (top left) and q-space function (top right) used to calculate S_0^2 from 2 mol% Ca/ZnO, with fits are shown in dotted lines; k-space (k^2-weighting) data and fits in black and red, respectively (bottom).

Table S3.2. Best-fit of the EXAFS parameters of 2 mol% Ca/ZnO. Notation: N, coordination number; S_0^2, amplitude correction term; ΔE_0, energy correction factor; R, scattering path length; σ^2, disorder term. Values without error bounds were held constant. A k-range of 3.4-9.1 Å^{-1} and R-range of 1.0-3.5 Å were used.

Reference	**Path**	**N**	**R (Å)**	**σ^2 x 10^3 (Å^2)**	**ΔE_0 (eV)**	**R-Factor**	**S_0^2**
2% Ca/ZnO	Ca-O	6	2.39 ± 0.01	5.2 ± 2.0	0.3 ± 0.6	0.0044	0.73
	Ca-Ca	12	3.41 ± 0.01	4.6 ± 1.0			

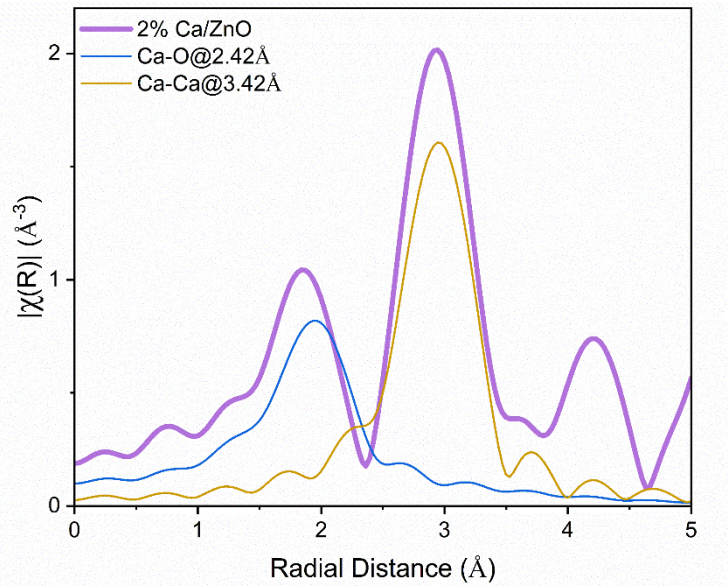

Figure S3.3. Magnitude of the Fourier transform of the first two phase-uncorrected single-scattering paths of CaO: Ca-O at bond distance of 2.42 Å and Ca-Ca at 3.42 Å, simulated with FEFF6. The comparison of the simulated paths to 2 mol% Ca/ZnO confidently describes the first 2 peaks of the data.

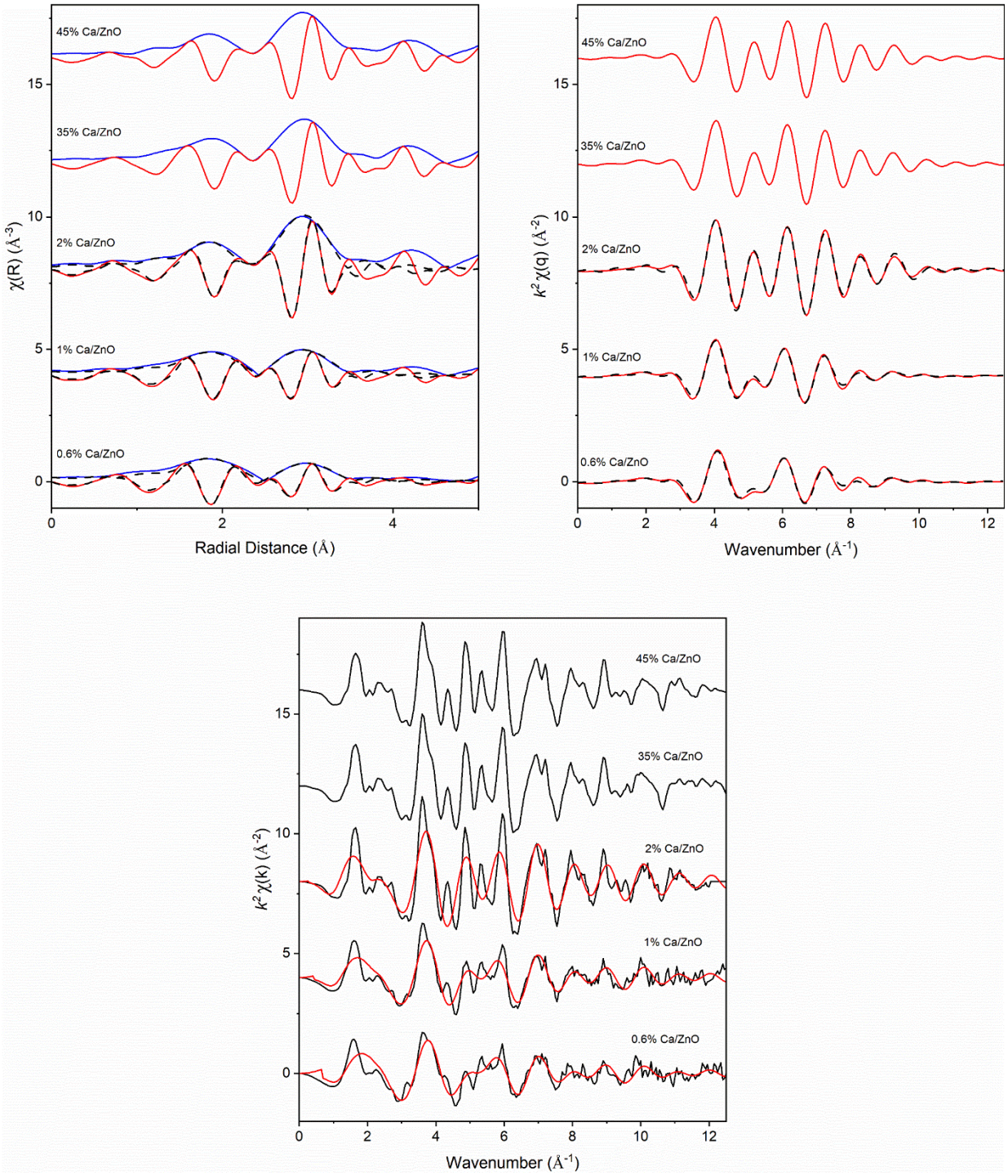

Figure S3.4. The magnitude and imaginary portion of the k^2-weighted Fourier transforms of the EXAFS spectra (top left) are shown using solid blue and red lines, respectively and q-space data (top right) shown in red, where fits are shown with dotted lines; k-space (k^2-weighting) data and fits in black and red, respectively (bottom).

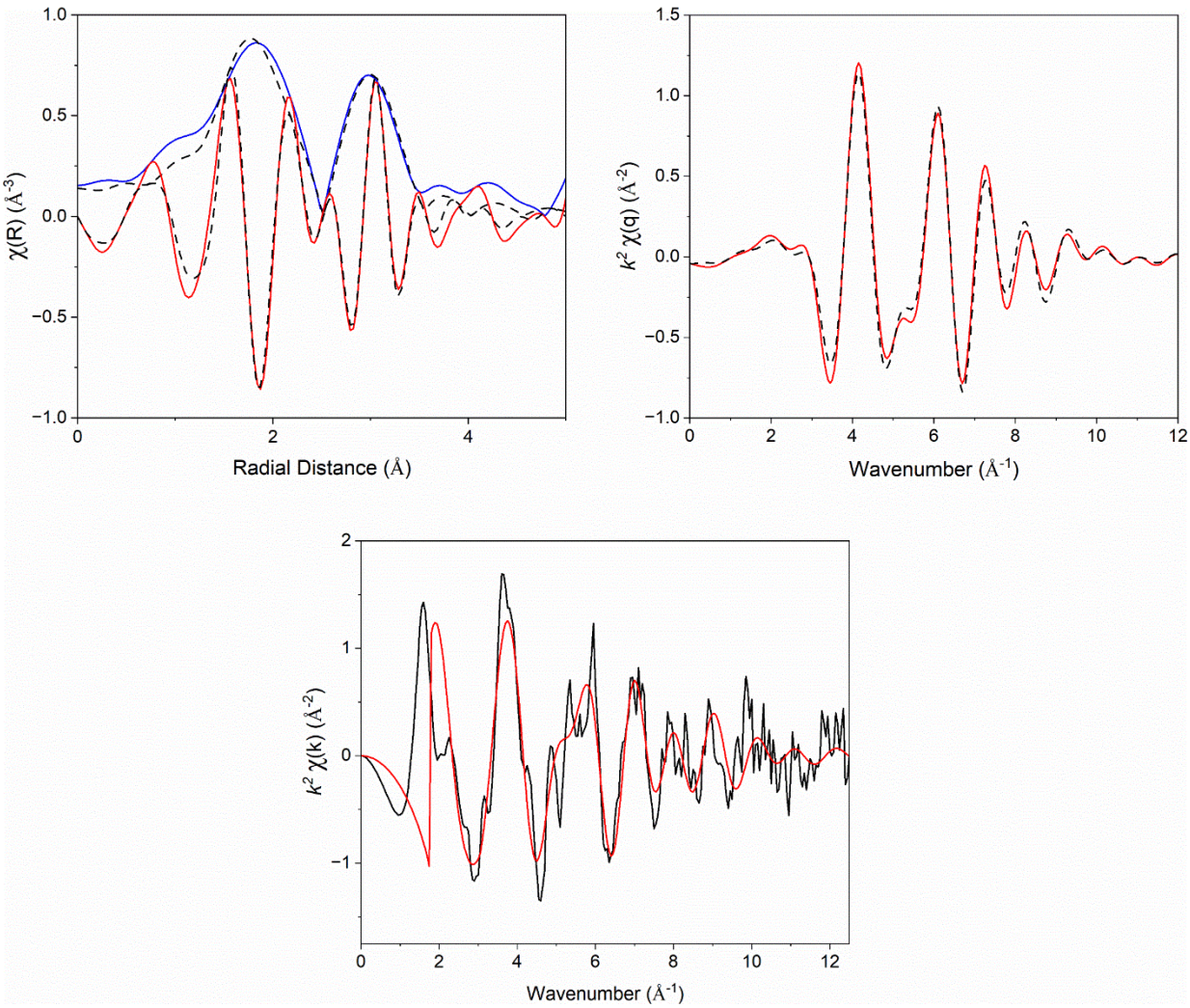

Figure S3.5. The magnitude and imaginary portion of the k^2-weighted Fourier transforms of the EXAFS spectra (top left) are shown using solid blue and red lines, respectively, and q-space data (top right) of the 0.6 mol% Ca/ZnO sample shown in red, where fits using a model of an isolated calcium atom on ZnO are shown with dotted lines; k-space (k^2-weighting) data and fits in black and red, respectively (bottom).

Table S3.3. Best-fit of the EXAFS parameters. Notation: N, coordination number; S_0^2, amplitude correction term; ΔE_0, energy correction factor; R, scattering path length; σ^2, disorder term. Values without error bounds were held constant. A k-range of 3.4-9.1 Å^{-1} and R-range of 1.0-3.5 Å were used.

Path	**N**	**R**	**σ^2 x 10^3 (Å^2)**	**ΔE_0 (eV)**	**R-Factor**	**S_0^2**
Ca-O	6	2.23 ± 0.02	10.1 ± 1.7	11.9 ± 1.3	0.0104	0.73
Ca-Zn	9.1 ± 3.1	3.25 ± 0.01	12.8 ± 3.7			

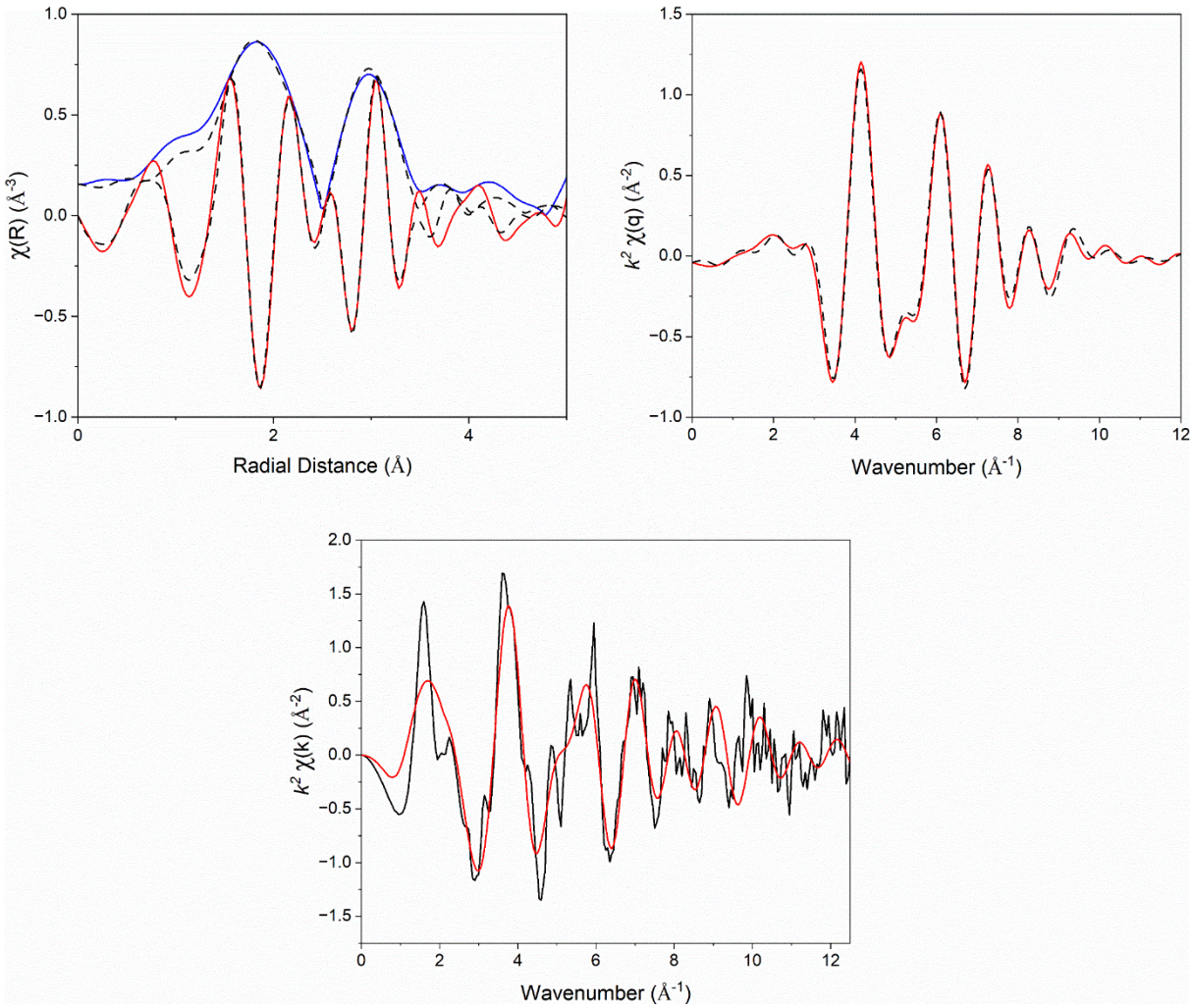

Figure S3.6. The magnitude and imaginary portion of the k^2-weighted Fourier transforms of the EXAFS spectra (top left) are shown using solid blue and red lines, respectively, and q-space data (top right) of the 0.6 mol% Ca/ZnO sample are shown in red, where fits using a model of calcium oxide nanoparticles on ZnO are shown with dotted lines; k-space (k^2-weighting) data and fits in black and red, respectively (bottom).

Table S3.4. Best-fit of the EXAFS parameters. Notation: N, coordination number; S_0^2, amplitude correction term; ΔE_0, energy correction factor; R, scattering path length; σ^2, disorder term. Values without error bounds were held constant. A k-range of 3.4-9.1 Å^{-1} and R-range of 1.0-3.5 Å were used.

Path	**N**	**R**	**σ^2 x 10^3 (Å^2)**	**ΔE_0 (eV)**	**R-Factor**	**S_0^2**
Ca-O	6	2.34 ± 0.3	7.5 ± 4.0	-0.6 ± 63.8	0.00566	0.73
Ca-Ca	4.7 ± 95.6	3.38 ± 1.0	4.6			
Ca-Zn	6.5 ± 910.0	3.10 ± 8.8	16.5 ± 108.1	-22.4 ± 827.1		

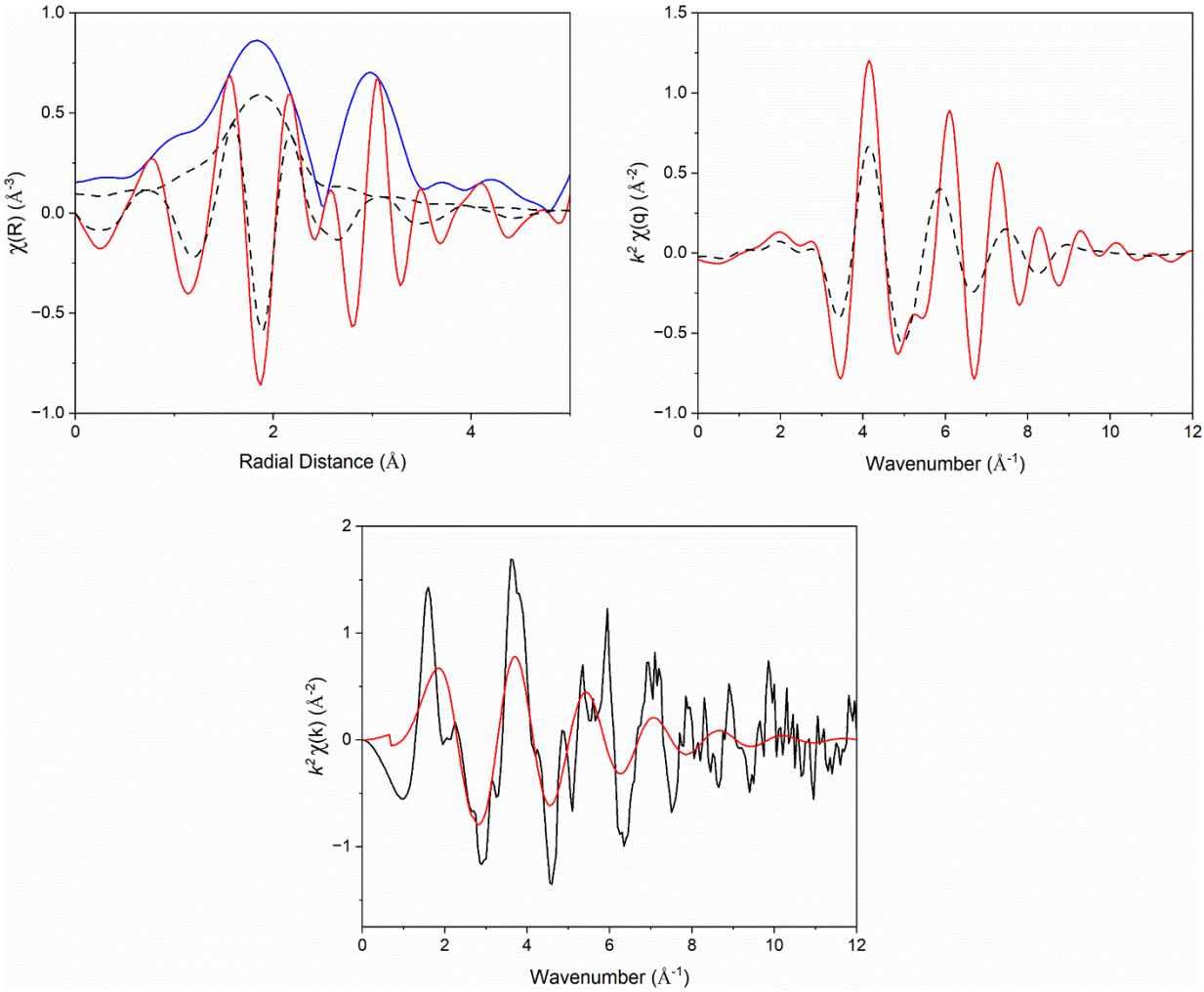

Figure S3.7. The magnitude and imaginary portion of the k^2-weighted Fourier transforms of the EXAFS spectra (top left) are shown using solid blue and red lines, respectively, and q-space data (top right) of the 0.6 mol% Ca/ZnO sample shown in red, where fits using a model of pure calcium hydroxide are shown with dotted lines; k-space (k^2-weighting) data and fits in black and red, respectively (bottom).

Table S3.5. Best-fit of the EXAFS parameters. Notation: N, coordination number; S_0^2, amplitude correction term; ΔE_0, energy correction factor; R, scattering path length; σ^2, disorder term. Values without error bounds were held constant. A k-range of 3.4-9.1 Å^{-1} and R-range of 1.0-3.5 Å were used.

Path	**N**	**R**	**σ^2 x 10^3 (Å^2)**	**ΔE_0 (eV)**	**R-Factor**	**S_0^2**
Ca-O	6	2.37 ± 0.3	12.1 ± 17.4	1.8 ± 25.6	0.5453	0.73
Ca-Ca	0.0 ± 16.8	3.63	10.8 ± 183472			

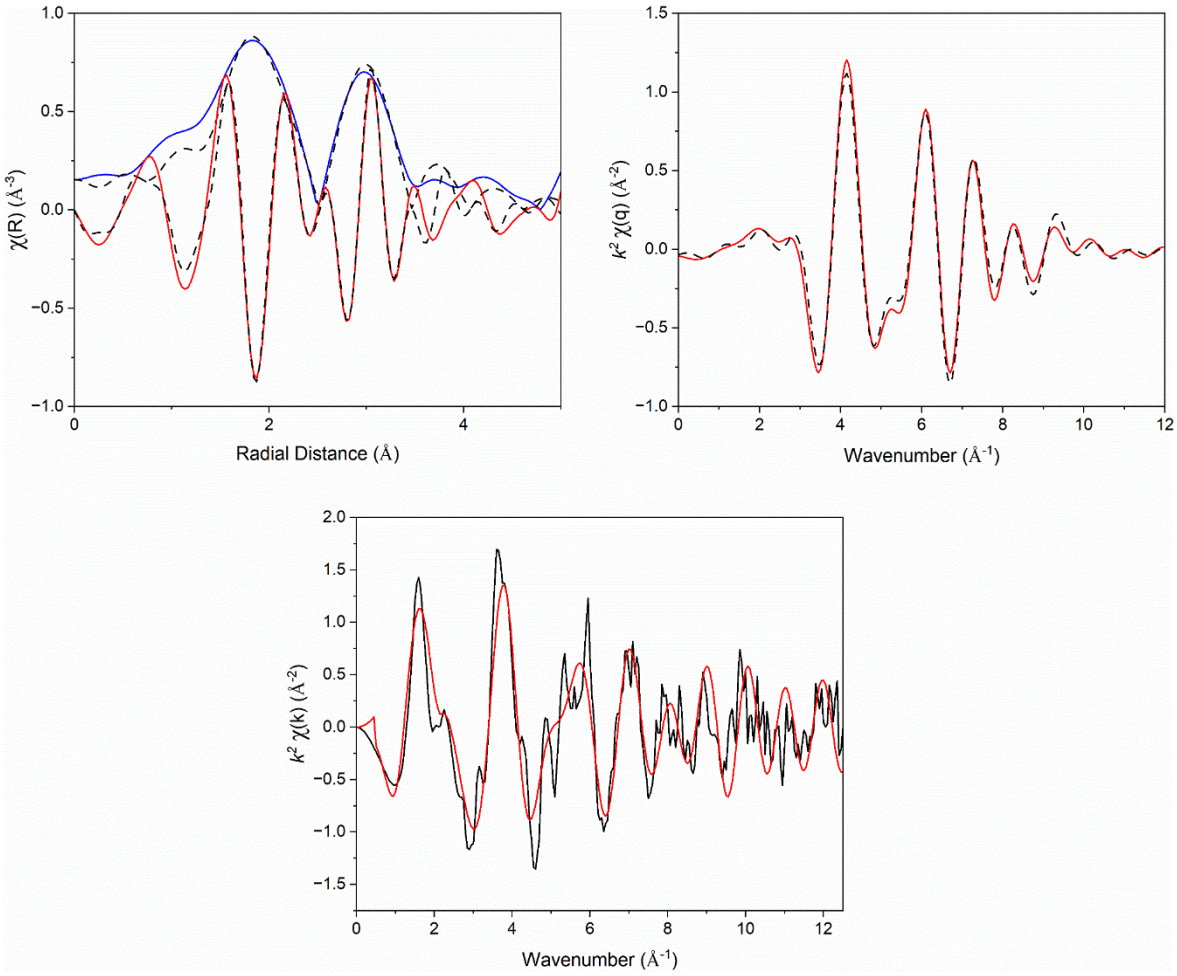

Figure S3.8. The magnitude and imaginary portion of the k^2-weighted Fourier transforms of the EXAFS spectra (top left) are shown using solid blue and red lines, respectively, and q-space data (top right) of the 0.6 mol% Ca/ZnO sample shown in red, where fits using a model of both calcium hydroxide and calcium oxide are shown with dotted lines; k-space (k^2-weighting) data and fits in black and red, respectively (bottom).

Table S3.6. Best-fit of the EXAFS parameters. Notation: N, coordination number; S_0^2, amplitude correction term; ΔE_0, energy correction factor; R, scattering path length; σ^2, disorder term. Values without error bounds were held constant. A k-range of 3.4-9.1 Å^{-1} and R-range of 1.0-3.5 Å were used.

Path	**N**	**R**	**σ^2 x 10^3 (Å^2)**	**ΔE_0 (eV)**	**R-Factor**	**S_0^2**
Ca-O	6	2.36 ± 0.1	6.9 ± 7.7	0.9 ± 9.6	0.0088	0.73
Ca-Ca (oxide)	11.5 ± 34.6	3.47 ± 0.1	4.6			
Ca-Ca (hydroxide)	11.1 ± 43.3	3.63	4.5 ± 1.1	-6.9 ± 14.5		

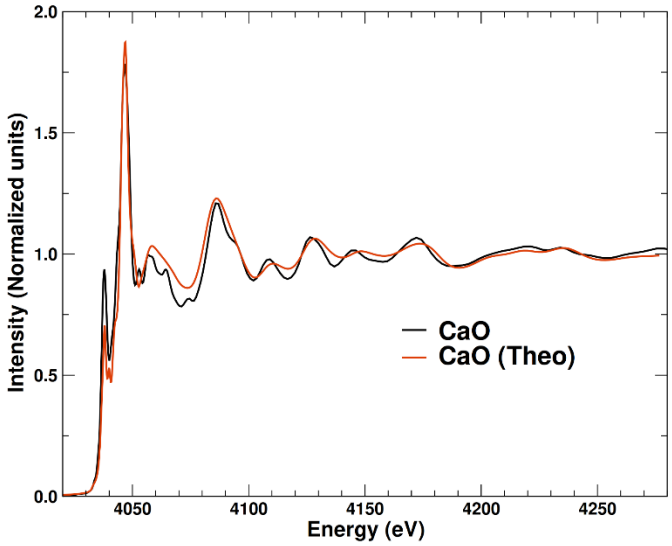

Figure S3.9. Comparison of experimentally measured Ca K-edge XANES spectrum of CaO reference to simulated XANES spectrum of a Ca atom from within the bulk of a large CaO structure.

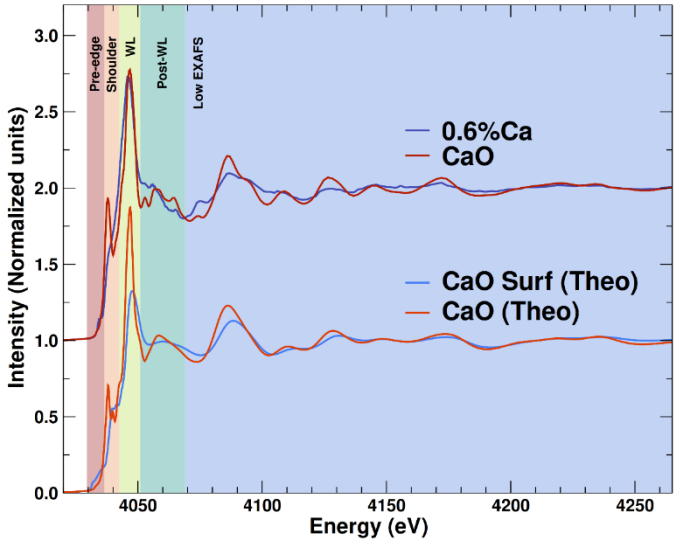

Figure S3.10. Comparison of experimental spectra of 0.6 mol% Ca/ZnO and bulk CaO reference to simulated spectra of a surface Ca atom of a CaO slab and a bulk Ca atom.

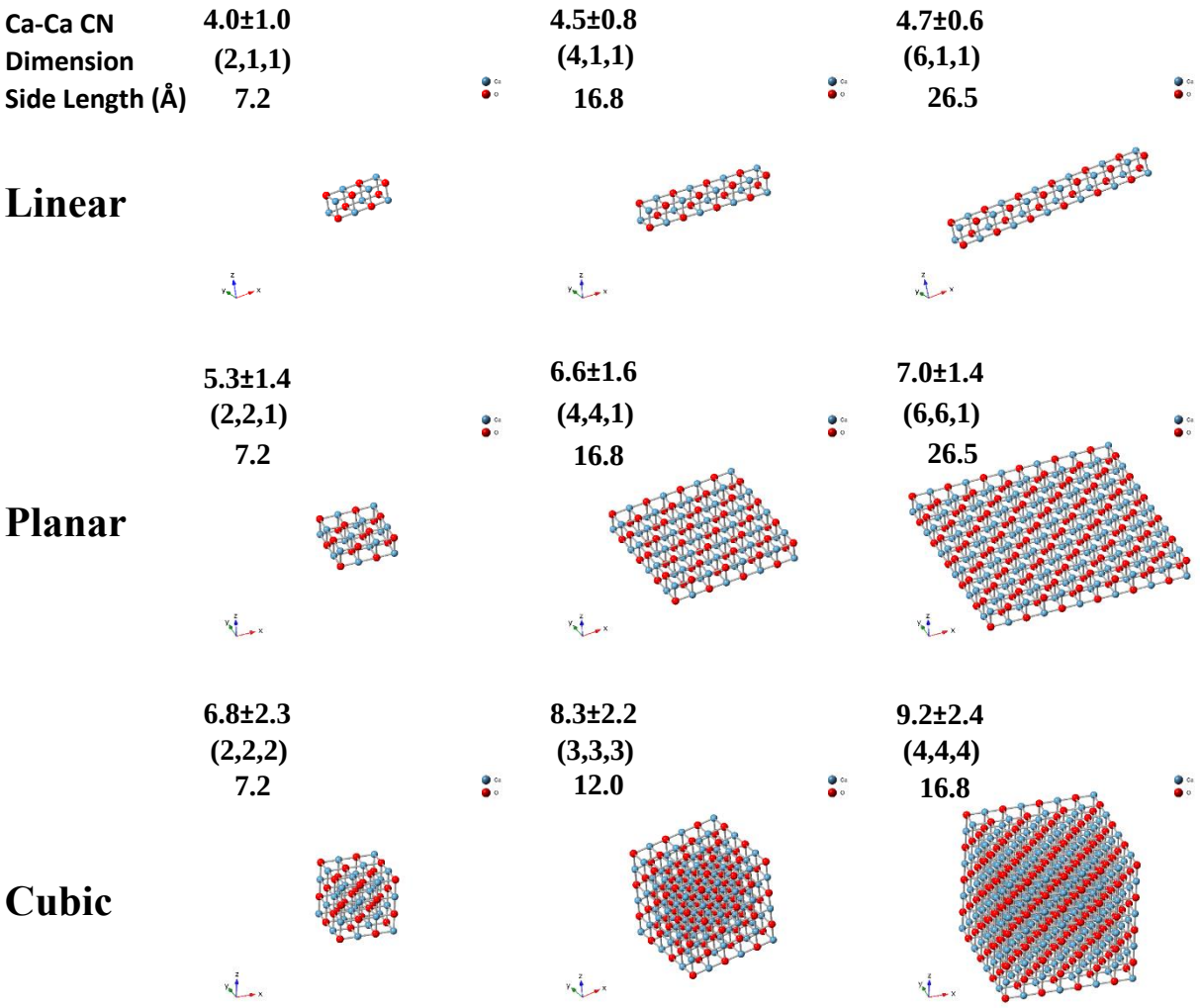

Figure S3.11. CaO structures of varying size and morphology used to simulate Ca K-edge spectra

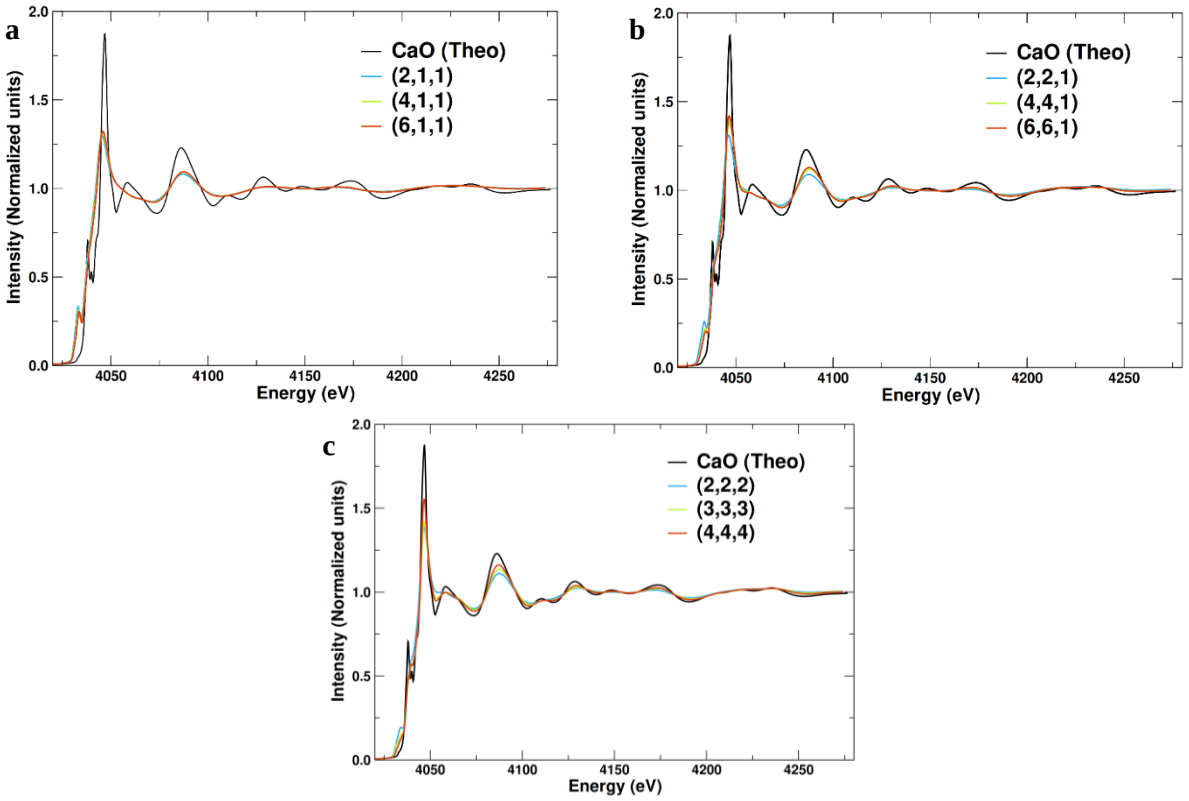

Figure S3.12. Comparison between the simulated XANES spectra of bulk CaO and varying sizes of (a) linear, (b) planar, and (c) and cubic structures.

Table S3.7. Total and regional ΔXANES matching Frechet-distance-like errors between theory and experiment. The Frechet figure of merit (FOM) is defined as: Given a reference function f_1 and a target f_2 represented by the curve segments with coordinates $\{x_{1i}, y_{1i}\}$ and $\{x_{1i}, y_{1i}\}$, we define the vector $\vec{d}_{1i2} = \{d_{1i2j}\}$ of distances from point i in f_1 to any point in f_2. With these distances we can define the FOM as $FOM = \sum_i \min[\vec{d}_{1i2}]/L$, where the normalization factor L is the length of the f_1 curve segment defined as $L = \int_{x_{11}}^{x_{1n}} dx_1 \sqrt{1 + \left(\frac{\partial f_1}{\partial x_1}\right)^2}$.

NP	Pre-edge	Shoulder	WL	Post-WL	Low EXAFS	Total
Ln_01_01_01	5.09	6.72	5.07	0.74	0.34	0.82
Ln_02_01_01	3.72	4.59	4.19	0.70	0.33	0.69
Ln_03_01_01	3.22	3.29	4.03	**0.68**	0.31	0.62
Ln_04_01_01	3.23	3.93	3.79	0.70	0.31	0.63
Ln_05_01_01	3.05	3.63	3.62	0.69	0.31	0.61
Ln_06_01_01	2.96	3.51	**3.56**	0.69	0.31	0.60
Pl_02_02_01	2.65	2.82	3.85	0.70	0.35	0.62
Pl_03_03_01	2.10	2.54	3.63	**0.68**	0.33	0.57
Pl_04_04_01	1.80	2.42	3.82	0.71	**0.30**	0.55
Pl_05_05_01	1.67	2.40	3.84	0.71	**0.30**	0.54
Pl_06_06_01	1.56	**2.39**	3.75	0.72	**0.30**	**0.53**
Cu_02_02_02	1.73	2.59	4.20	0.70	0.35	0.60
Cu_03_03_03	1.18	2.92	4.71	0.85	0.33	0.61
Cu_04_04_04	**0.83**	3.02	3.99	0.85	0.36	0.60

NP	Pre-edge	Shoulder	WL	Post-WL	Low EXAFS	Total
CaO Expt vs Theo	0.11	0.84	0.51	0.28	0.10	0.15

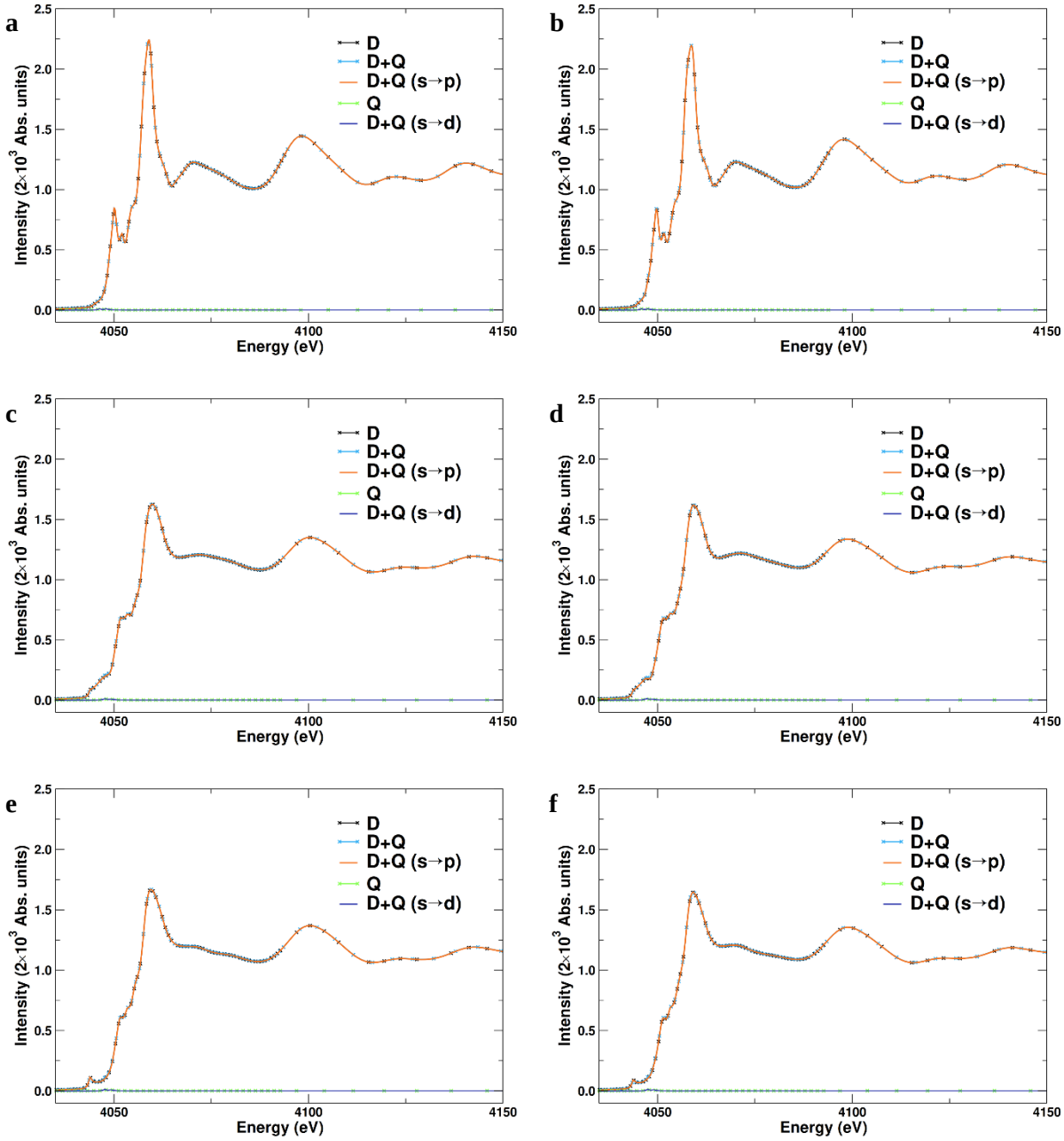

Figure S3.13. Decomposition of the dipole and dipole+quadrupole contributions to the theoretical spectra of (a-b) bulk CaO, (c-d) surface Ca atom, and (e-f) oxygen-terminated surface Ca atom into their s→p and s→d components (a, c, e) without and (b, d, f) with a distortion applied to the central Ca atom of +0.1 Å along the z-axis.

Table S3.8. Summary of catalytic performance over the range of Ca loadings.

Ca Loading	CH_4 Conversion (%)	N_2O Conversion (%)	C_2H_6 Yield (mmol/h)	C_2H_4 Yield (mmol/h)	$C_{3,4}$ Yield (mmol/h)	CO Yield (mmol/h)	CO_2 Yield (mmol/h)
ZnO	8.6	11.4	0.06	0.01	0.001	0.004	0.56
0.2%	9.9	13.9	0.06	0.02	0.002	0.005	0.63
0.4%	9.0	9.2	0.11	0.03	0.006	0.009	0.43
1%	9.3	9.3	0.12	0.03	0.009	0.014	0.42
2%	9.3	7.4	0.15	0.03	0.013	0.029	0.35
35%	8.0	8.0	0.10	0.02	0.004	0.069	0.35
45%	3.4	5.2	0.03	0.00	0.000	0.000	0.22
CaO	1.2	11.4	0.00	0.00	0.000	0.006	0.10

Reaction conditions: 550 °C; 0.75 g catalyst; 13.3 mL min^{-1} total gas flow rate with P_{CH_4} = 0.23 atm, P_{N_2O} = 0.45 atm, P_{Ar} = 0.32 atm; 7 h on stream. All Ca loadings are reported in molar concentration of metal cations, as determined by ICP-MS (Table S#).

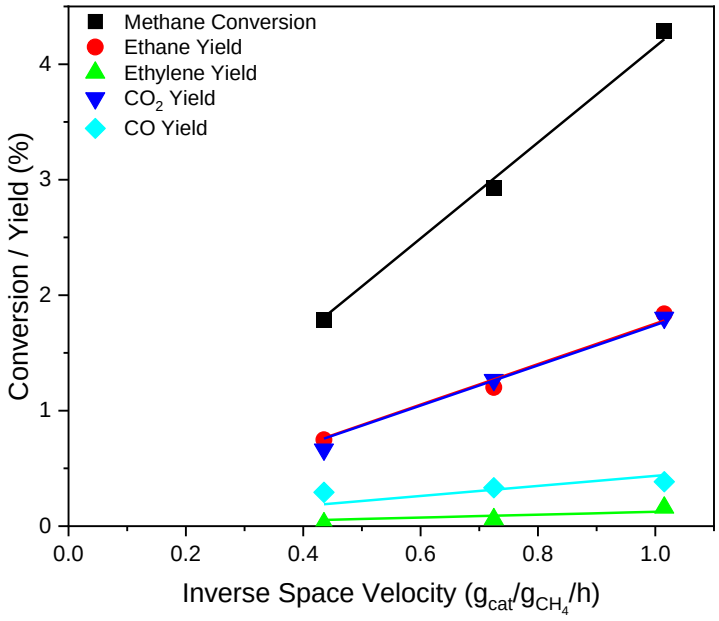

Figure S3.14. Inverse space velocity of reactant conversion and product rates confirming differential regime during steady state N_2O-OCM at 560 °C, 43.75 mL/min total flow, methane:N_2O:argon feed ratio of 1:3:1, varying catalyst mass (0.15 g, 0.25 g, 0.35 g).

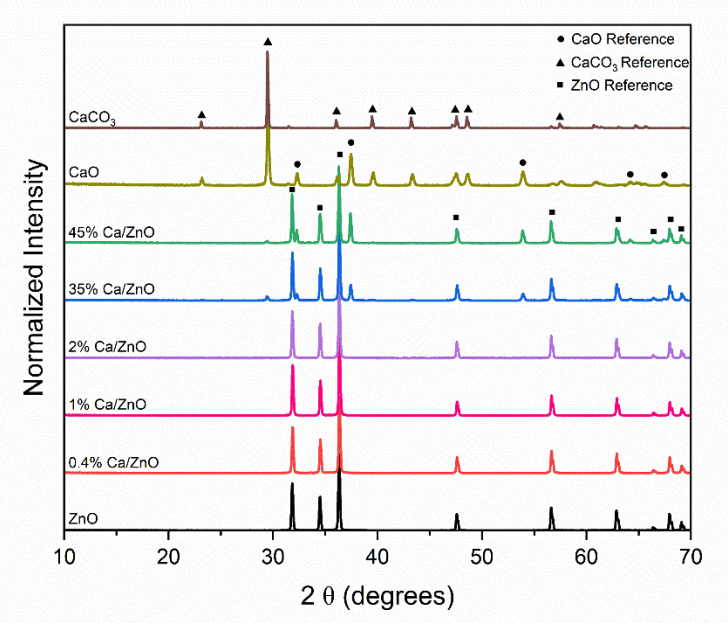

Figure S3.15. X-ray diffractograms of catalysts after N_2O-OCM. Diffractograms were collected using a Bruker D8 Advanced Diffractometer with Cu Kα radiation. Powder catalysts were sieved through a 304 stainless steel wire cloth disc with a mesh size of 200 to ensure a random distribution of exposed facets, then adhered to silica sample holders with Dow Corning high vacuum grease.

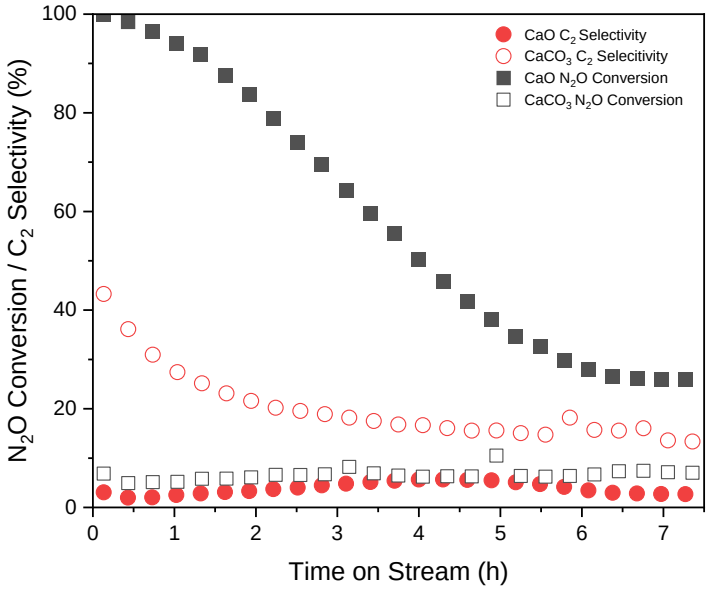

Figure S3.16. Reactivity of CaO and $CaCO_3$ over the course of N_2O-OCM. Reaction conditions: 550 °C; 0.75 g catalyst; 13.3 mL min^{-1} total gas flow rate with P_{CH_4} = 0.23 atm, P_{N_2O} = 0.45 atm, P_{Ar} = 0.32 atm.

Chapter 4. Effects of Reaction Conditions on Kinetics and Product Distributions across Multiple Oxidants: CO_2, N_2O, and O_2

4.1 Abstract

The CO_2-OCM and N_2O-OCM catalytic performances of Ca clusters on ZnO have been compared with that of bulk CaO on ZnO in Chapters 2 and 3, respectively. There are assumed to be many mechanistic similarities between CO_2-OCM, N_2O-OCM, and OCM, but few studies comparing all three reactions over similar catalysts exists. In this chapter, Ca/ZnO catalytic performances for CO_2-OCM, N_2O-OCM, and OCM are presented, which demonstrate the kinetic differences between OCM and soft oxidant-assisted OCM that result in differing dependencies of C_2 yields on reactant concentrations and temperature.

4.2 Introduction

Soft oxidant-assisted methane coupling is being explored as an alternative to OCM. The yields of C_2 products from OCM fall short of the commercial expectation of >25% single-pass yield due to the formation of undesired products, CO and CO_2, via overoxidation.[1] However, little is understood about the soft oxidant-assisted methane coupling mechanism and the influence of reaction parameters compared to OCM. CO_2 addition to OCM over Pb/MgO and Li/MgO decreases total methane conversion but increases C_2 product selectivity. Higher C_2 product selectivity are observed with CO_2 present in the reactant feed at similar degrees of methane conversion.[2,3] However, very few studies have compared catalyst performance between OCM and CO_2-OCM. Comparisons between N_2O-OCM and OCM have demonstrated the positive influence of N_2O on C_2 product selectivities over Sm_2O_3 and Li/CaO.[4,5] A preliminary result of N_2O addition to OCM feed over MgO suggests an improvement of C_2 product selectivities as well.[6] However, there have been very limited studies that compare catalytic performance of a single, well-defined catalyst for all three of these methane coupling reactions. In this chapter, reaction conditions of CO_2-OCM, N_2O-OCM, and OCM are varied to measure similarities and differences in their impact on reaction kinetics and product distributions over impregnated metal oxides, namely Ca/ZnO.

4.3 Experimental Methods

Catalyst Synthesis

Calcium oxide-zinc oxide composite catalysts were prepared via a wet impregnation synthesis as described earlier.[7] Briefly, calcium nitrate tetrahydrate (99% ACS Reagent, MP Biomedicals) was dissolved in MilliQ (18 Mohm) water. Zinc oxide (99.9% metal basis, Alfa Aesar) was added, and the resulting slurry was sonicated, and stirred partially covered overnight. The resulting white solids were dried at 120 °C for 24 h before calcining in 50 mL/min air (zero air, Praxair) at 850 °C (ramp 5 °C/min) for 4 h. Calcium oxide was synthesized by heating 100 mL of a 0.25M calcium nitrate solution in an oil bath to 80°C.[8] Under vigorous stirring, a 50 mL solution of 1M NaOH was added dropwise, resulting in a cloudy solution of white precipitate. The solids were vacuum filtered, washed with deionized water, and dried overnight at 120 °C before calcination (see above).

Calcium was ion-exchanged onto ZnO by first creating 40 mL of a 50 mM $Ca(NO_3)_2$ solution, then adding 0.3 g ZnO powder to the solution while stirring. A 1 M NH_4OH solution was added dropwise until the pH of the calcium solution reached 10.8. The solution was stirred for 24 h with periodic pH adjustments. The solids were vacuum filtered and rinsed with MilliQ water 3 times, then oven dried overnight at 80 °C before calcination (see above).

ZnO of varying morphology was synthesized hydrothermally by dissolving 1.5 g zinc nitrate hexahydrate (99% metals basis, Alfa Aesar) in 200 mL MilliQ water. Trisodium citrate anhydrous (99%, Alfa Aesar) was added to the solution to result in a citrate:Zn ratio of 0.002 only for the plates.[9] A second solution of 0.7 g hexamethylenetetramine (99.0+%, TCI America) dissolved in 200 mL MilliQ water was made. Both solutions were cooled in an ice bath for 10 min before being combined in an autoclavable bottle, shaken, and heated at 95 °C for 4 h for plates or 21 h for rods. The resulting suspension was cooled in an ice bath, filtered, rinsed with MilliQ water 3 times, then oven dried overnight at 120 °C before calcination (see above).

Li/MgO catalysts were synthesized by first adding 1.0 g MgO (99+%, 100 nm) to 20 mL MilliQ water at 50 °C and sonicating the solution. $LiCO_3$ (=99%, ACS Reagent Grade, MP Biomedicals) was added to the solution. The mixture was stirred uncovered for roughly 48 h or until all water evaporated.[10] The solids were oven dried at 80 °C overnight before calcination (see above).

Pt/MgO[11] and Pd/MgO[12] catalysts were acquired from collaborators.

Catalytic activity measurements

All reactor experiments were conducted in a quartz down-flow, packed-bed reactor with 4 mm ID. Generally, catalyst powder was loaded into the tube, supported by quartz wool (Acros Organics). The reactor was heated in a tubular furnace to reaction temperature under nitrogen (99.999%, Praxair) for CO_2-OCM and N_2O-OCM or dry air for OCM. Flow was then switched to bypass the reactor and adjusted to the desired reaction mixture prior to flow through the reactor. Reaction products were measured by an online Agilent 7890A gas chromatograph (GC) with a FID and TCD. Empty reactors were used to determine conversion in the absence of catalyst prior to each experiment. Experiments that involve ramping the reaction temperature consisted of pretreating the catalyst *in situ* according to its typical calcination procedure before cooling to the initial reaction temperature and stabilizing reactant flowrates. The heating rate was either programmed such that each GC injection occurred every 25 °C or held at the target temperature until reaching steady state before ramping to the next target temperature. Specific experimental details, including space velocity, reaction temperature, and reactant concentrations, accompany the respective data in figure captions below.

Materials characterization

Calcium loading was quantified by inductively coupled plasma optical emission spectroscopy (ICP-OES). CO_2-TPD experiments were performed with a Netzsch STA 449 F3 Jupiter thermogravimetric analysis unit with QMS 403 D Aeolos mass spectrometer. Roughly 30 mg of material are loaded into the sample cup and pretreated with 40 mL min^{-1} dry air at 850 °C (5 °C min^{-1}) ramp for 4 h. Once cooled to room temperature (< 30 °C), 50 mL min^{-1} CO_2 was flowed for 1 h, then purged with 50 mL min^{-1} N_2 for 1 h or until the MS signal had stabilized. The TPD was carried out in 30 mL min^{-1} N_2 and heating to 900 °C (10 °C min^{-1}).

Nitrogen physisorption isotherms were measured using a Micromeritics 3Flex physisorption/chemisorption instrument. Physisorption measurements were made at -196 °C. Samples were degassed at 300 °C for 3 h under vacuum prior to analysis. Surface areas were determined by the BET method. Scanning electron microscopy (SEM) was performed on a Thermo Fisher Scientific Quattro ESEM. Samples were pressed onto carbon tape on a sample stub. Images were acquired under vacuum using a spot size of 3 and an accelerating voltage of 5 kV. X-ray diffraction (XRD) patterns were recorded on a Bruker D8 Advanced Diffractometer with Cu Kα radiation. Powder samples were sieved through a 304 stainless steel wire cloth disc with a mesh size of 200 to ensure a random distribution of exposed facets. They were adhered to silica sample holders with Dow Corning high vacuum grease. Synchrotron X-ray absorption spectroscopy (XAS) experiments were conducted at beamline 7.3.1 of the Advanced Light Source (ALS), Lawrence Berkeley National Laboratory. Spectra of total electron yield (TEY) were collected and charge-corrected by referencing a standard to known values.[13,14] Diffuse reflectance infrared Fourier transform spectroscopy (DRIFTS) was performed with a Bruker VERTEX 70 FTIR Spectrometer equipped with a Pike Technologies DiffusIR MidIR Accessory. Spectra were collected with 128 scans at a resolution of 2 cm^{-1}. *In situ* calcinations were performed by heating the sample 10 °C min^{-1} to 850 °C for 30 min under 20 mL min^{-1} of dry air flow. At room temperature (below 30 °C), N_2O was introduced by flowing 10 mL min^{-1} of N_2O. After the signal stabilized, the cell was purged with 50 mL min^{-1} of N_2 for 10 min.

4.4 Results and Discussion

Kinetic Analysis of N_2O-OCM

The influence of active site structure on the N_2O-OCM rate was discussed in Chapter 3. Here, the effect of reactant concentration on kinetic parameters is investigated. First, the activation energy of ethane production, shown in Figure 4.1, gradually increases with increasing N_2O concentration. The activation energy over 1% Ca/ZnO still remains significantly lower than that over 35% Ca/ZnO. This minor change in activation energy can be a result of a minor change to the active site structure during reaction. The main differences in the reaction conditions are the concentrations of oxidant and CO_x products. The calcium sites

begin as oxidized clusters and transform during reaction into carbonate crystallites of undetermined size (Chapter 3). N_2O adsorption does not form stable surface species (Figure 4.7), but CO_x adsorption does. It is possible that the carbonate phase on the catalyst surface is larger and has a great inhibitory effect with a higher concentration of CO_x in the gas phase. Surface carbonate formation is known to significantly impact reaction kinetics[15] and makes determination of inherent N_2O-OCM kinetics in the absence of carbonate difficult.

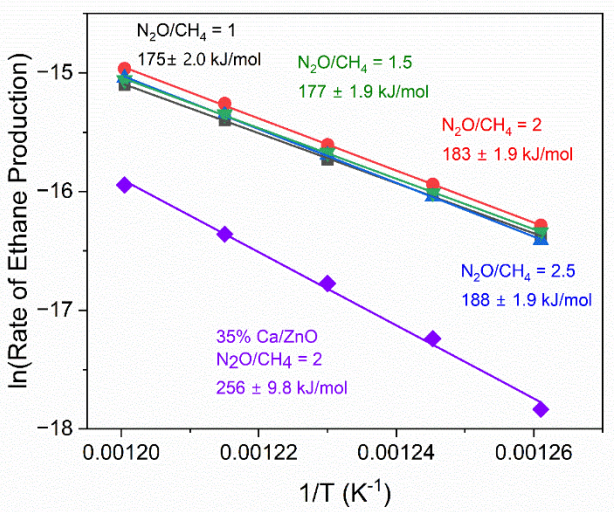

Figure 4.1. Comparison of methane coupling activation energies over 1% Ca/ZnO and 35% Ca/ZnO with varying reactant feed compositions: 200 mg catalyst, total flow of 30 mL/min, P_{CH_4} = 0.25 atm, temperature range of 520 °C to 560 °C. Error calculated from linear fit.

By changing the partial pressure of N_2O, we can determine the methane coupling rate dependence on the reactant concentration (Figure 4.2). As N_2O partial pressure increases from 0.25 to 0.5 atm, the rate of ethane formation increases. Higher than 0.5 atm, the rate seems to decrease, but additional work would be needed to prove the statistical significance of the trend. A lack of N_2O partial pressure dependence on the ethane formation rate at high pressures indicates a high surface coverage of reactive surface oxygen intermediates formed from N_2O dissociation. Again, CO_2 poisoning could be playing a major role in the observed rates.[15] Experiments that measure the methane coupling rate and other relevant kinetic parameters should also be conducted with controlled addition of CO_2 to quantify its effects.

The reaction order of N_2O for the rate of ethane formation was found to be 0 at partial pressures greater that 0.5 atm. Below that, the reaction order was experimentally determined in Figure 4.3 to be ~0.15 at all temperatures measured. The lack of change with temperature is likely because the temperature is not changing the coverage of surface oxygen species formed from N_2O dissociation. The positive, non-integer value of the reaction order suggests the ethane formation rate is controlled by multiple steps, yielding a complex mechanism and rate law.

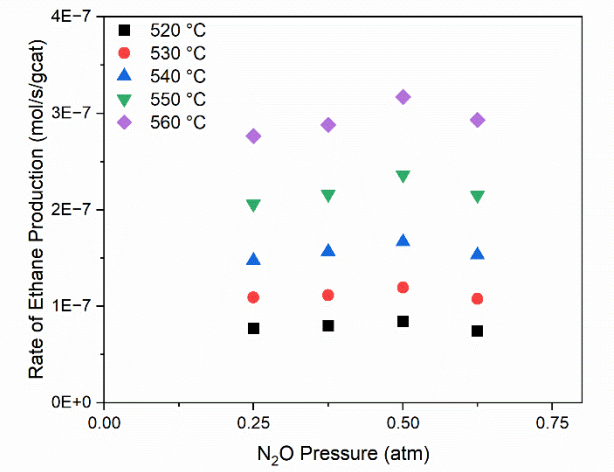

Figure 4.2. Effect of N_2O partial pressure on the steady state methane coupling rate at P_{CH_4} = 0.25 atm and balance argon measured at 5 different temperatures between 520 °C to 560 °C; 30 mL/min total flow over 200 mg of 1% Ca/ZnO.

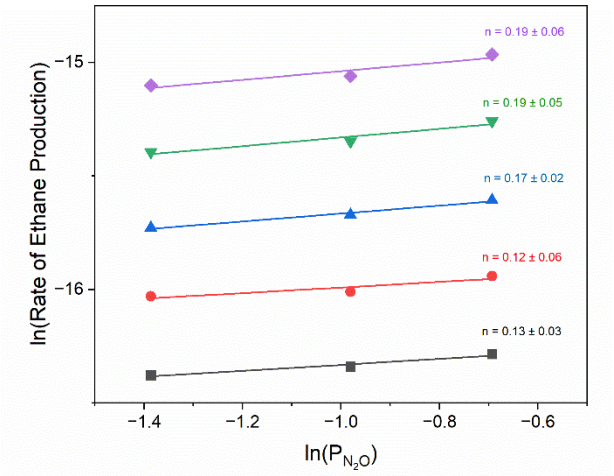

Figure 4.3. Steady state methane coupling rate law dependence on N_2O partial pressure at P_{CH_4} = 0.25 atm and balance argon measured at 5 different temperatures between 520 °C to 560 °C; 30 mL/min total flow over 200 mg of 1% Ca/ZnO.

N_2O concentration has a small effect on the methane coupling rate, but we hypothesize it would have a larger impact on methane oxidation to CO_x species. There was no change in CO_x production rate at partial pressures above 0.5 atm, again suggesting that the catalyst surface is covered predominately by active surface oxygen species formed from N_2O dissociation. Below 0.5 atm N_2O, the reaction order is ~0.86 with respect to N_2O for both CO and CO_2 formation (Figure 4.4). The positive, non-integer value of the reaction order suggests the methane oxidation rate, too, is controlled by multiple steps, yielding a complex mechanism and rate law. The same reaction order for CO and CO_2 formation indicates that the rate limiting step for their formation is the same one involving N_2O.

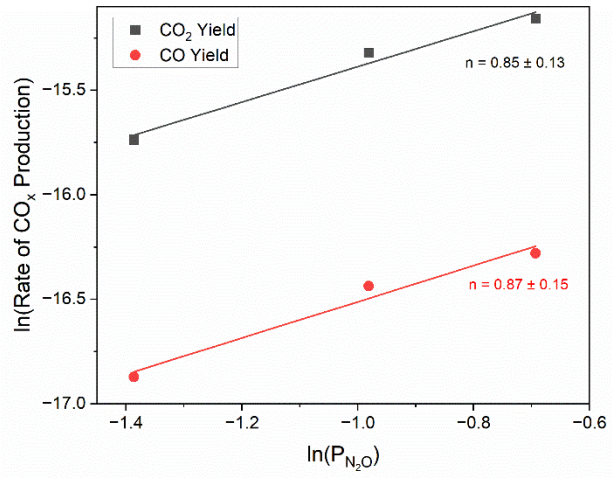

Figure 4.4. Steady state methane oxidation rate law dependence on N_2O partial pressure at P_{CH_4} = 0.25 atm and balance argon measured at 5 different temperatures between 520 °C to 560 °C; 30 mL/min total flow over 200 mg of 1% Ca/ZnO.

The steady-state conversion-selectivity trend of N_2O-OCM over 1% Ca/ZnO developed by changing both catalyst mass and reactant flowrates is shown in Figure 4.5. Some discontinuity is observed between conditions with different masses of catalyst. Ethane, CO, and CO_2 selectivity trends do not approach 0 with decreasing conversion, but ethylene and $C_{3,4}$ products do. This indicates that ethane, CO, and CO_2 are primary reactions products from methane coupling, partial oxidation, and complete oxidation, respectively. Ethylene and $C_{3,4}$ products are secondary products. The rising trend of CO_2 complements the decrease in CO selectivity, suggesting that higher methane conversion leads to more complete oxidation. Ethane selectivity also decreases with increasing methane conversion, while the selectivities of ethylene and $C_{3,4}$ products increase. At higher conversions, ethane further reacts and undergoes dehydrogenation or coupling.

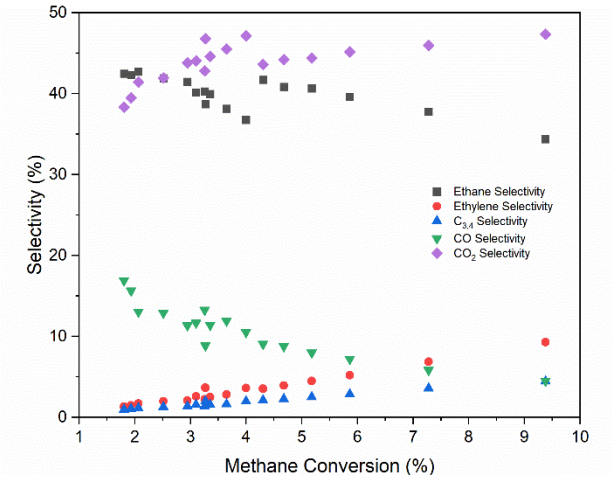

Figure 4.5. Selectivity–conversion relationship of product distribution during N_2O-OCM over 1% Ca/ZnO. Conversion varied by changing the space velocity 0.4-1.8 $g_{cat}/(g_{CH_4}/h)$.

Product ratios are plotted in Figure 4.6 as both a function of temperature and N_2O/CH_4 ratio to illustrate the changes in product distribution under varying conditions. With increasing temperature, CO is further oxidized to CO_2, and ethane dehydrogenates more readily to ethylene. The rate of C_2 product formation increases more rapidly than CO_x production with temperature. There is a large increase in CO_x/C_2 and C_2H_4/C_2H_6 ratios once N_2O composition is in excess of methane. The higher concentration of oxidant leads to deeper oxidation to secondary products.

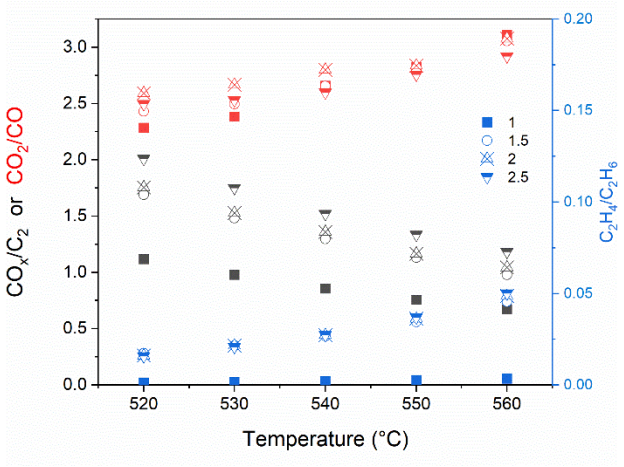

Figure 4.6. Influence of N_2O/CH_4 feed ratio on product distribution over 1% Ca/ZnO: 200 mg catalyst, total flow of 30 mL/min, $P_{CH_4} = P_{Ar}$, temperature range of 520 °C to 560 °C.

The ability of Ca/ZnO to adsorb and desorb CO_2 during CO_2-OCM was determined to be as strong descriptor of methane coupling activity.[7] We hypothesize that the adsorption and desorption of N_2O is of equal importance. *Ab initio* calculations predict N_2O preferably adsorbs side-on to a corner O^{2-} site on CaO(100), but dissociation occurs by oxygen end-on interaction with a surface O^{2-}.[16] Attempts to characterize the adsorption with *in situ* DRIFTS is shown in Figure 4.7. After exposing CaO to N_2O, bands at 3655 cm^{-1} of calcium hydroxide[17], 2250-2175 cm^{-1} of gaseous N_2O[18], and 1600-1320 cm^{-1}, 1080 cm^{-1}, and 866 cm^{-1} of calcium carbonate[19] were observed. The hydroxide and carbonates surface phases formed from exposure to gas impurities of H_2O and CO_2. No additional peaks corresponding to adsorbed N_2O or NO species at 1031 cm^{-1} or 1265 cm^{-1},[20] respectively, were observed. Contrary to CO_2 adsorption, N_2O

exposure does not yield any surface-stable adsorbates. Therefore, interactions with the catalyst surface must be very brief for N_2O decomposition.

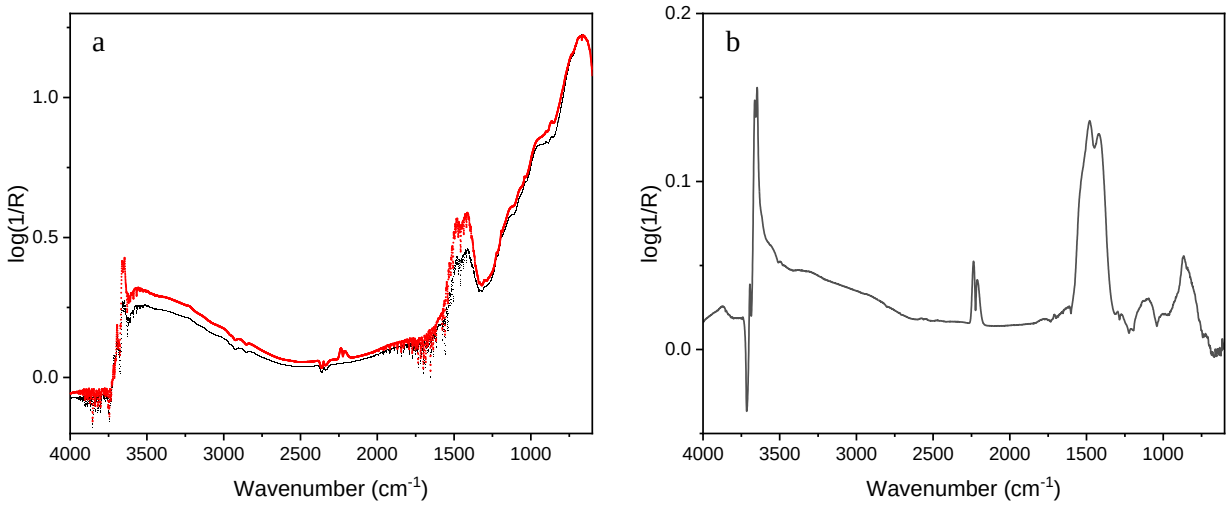

Figure 4.7. DRIFTS spectra (a) before (black) and after (red) introducing CaO to a gas stream of N_2O. (b) Difference between before and after spectra.

Mechanistic Investigation of CO_2-OCM and Comparisons to Traditional OCM

The work in Chapter 2 focused predominately on the geometric and electronic active site structure of CO_2-OCM catalysts. Here, we conduct a preliminary investigation into the reaction mechanism and influence of process parameters – temperature, oxidant concentration and identity – over Ca/ZnO catalysts and others. The influence of CO_2 concentration on CO_2-OCM conversion and product distribution are shown in Figures 4.8-9. An excess of CO_2 in the reactant feed at a partial pressure of 0.67 atm drastically increases both methane conversion and C_2 product selectivity. Conversely, decreasing CO_2 concentration and eventually removing it decreases methane conversion and C_2 product selectivity in favor of methane reforming to CO. The production of CO in the absence of an oxidant leads to catalysts reduction by lattice oxygen removal.[21] A significant increase in C_2 product selectivity at low CO_2 concentrations and little effect at high concentrations is consistent with reducible oxide supported CaO catalysts.[22] The activity is not reversible under these conditions, demonstrated by the changes in activity and selectivity between conditions of

identical feed composition of 0.5 atm CO_2. There is significant catalyst deactivation observed for CO formation. Due to this deactivation, the reaction order of CO_2 cannot be determined.

By taking the median product yields at each feed condition (as in Figure 4.9), the selectivity of C_2 products scales with the concentration of CO_2 in the reactant feed. CO_2 is critical for the active surface oxygen species formation that is selective for methane coupling.[21] A higher CO_2 concentration results in deeper ethane dehydrogenation to ethylene. CO_2-assisted ethane dehydrogenation is proposed to operate by a similar Mars van Krevelen mechanism.[23] A C_2H_4/H_2 ratio of 1.0 would be expected for non-oxidative ethylene formation. This ratio is greater than 1.0 for all conditions with CO_2 present and increases as CO_2 concentration increases. Water is produced at the expense of hydrogen likely due to a combination of oxidative coupling and dehydrogenation as well as reverse water gas shift (RWGS). RWGS is relevant at the reaction temperature of 850 ^oC[24] and affects CO_2-assisted ethane dehydrogenation.[25]

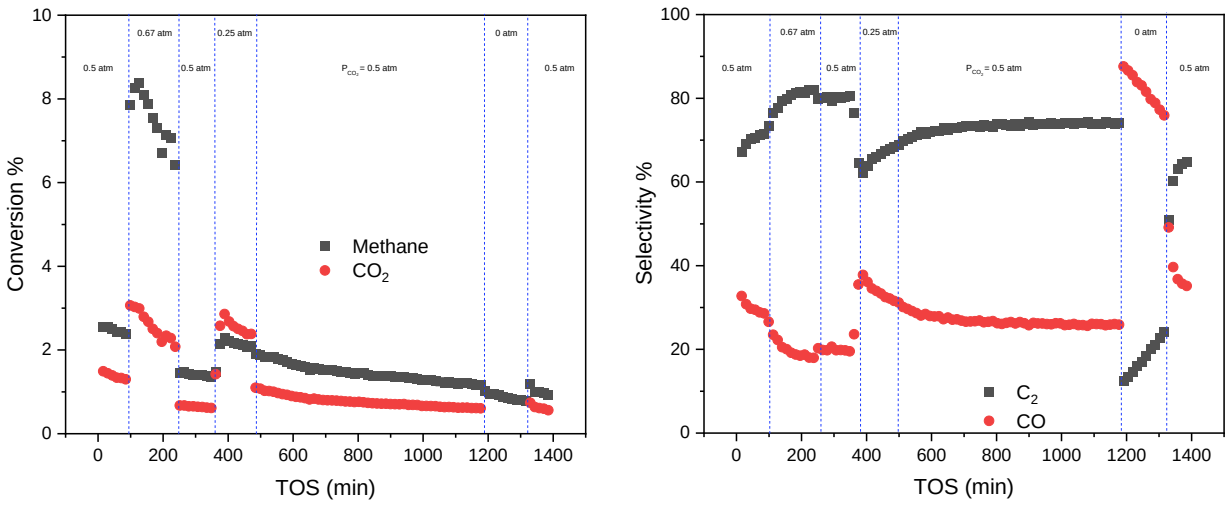

Figure 4.8. Effect of CO_2 partial pressure on CO_2-OCM activity over 0.1 g 35% Ca/ZnO. 13.3 mL/min total flow, P_{CH_4} = 0.25 atm with nitrogen balance, 850 ^oC.

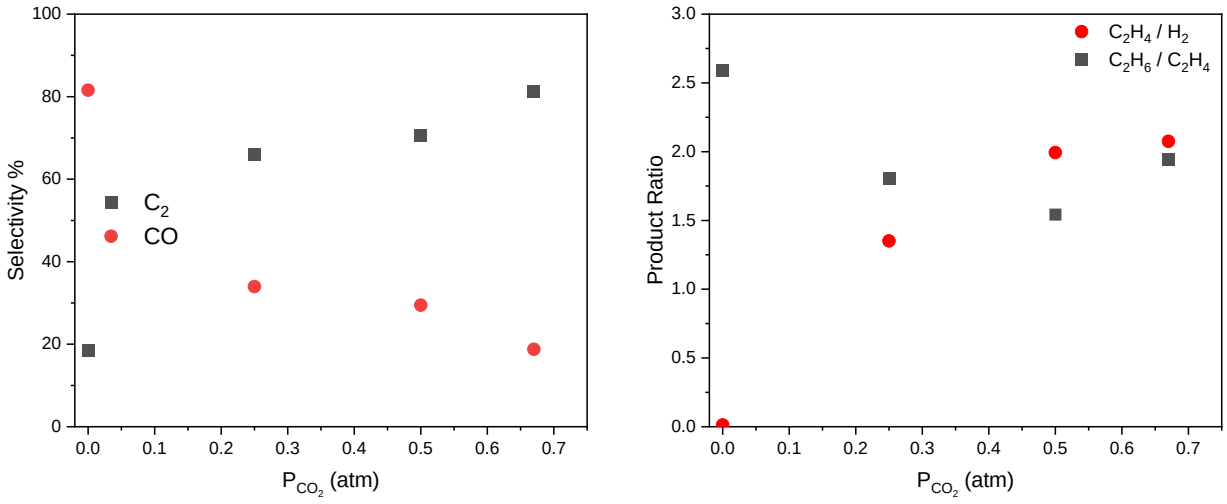

Figure 4.9. Effect of CO_2 partial pressure on CO_2-OCM product distribution over 0.1 g 35% Ca/ZnO. 13.3 mL/min total flow, P_{CH_4} = 0.25 atm with nitrogen balance, 850 ^oC.

Ion-exchange is an effective method of dispersing cationic species on a support to generate near-homogenous sites.[26] Dispersed Ca on ZnO exhibits unique catalytic performance for CO_2-OCM and N_2O-OCM, shown in Chapters 2 and 3, respectively. Calcium ion-exchange was explored as a method of catalyst synthesis and compared to the wet impregnation method, shown in Figure 4.10. Higher C_2 product selectivity is achieved over the Ca-ZnO ion-exchanged catalysts, compared to pure ZnO and 0.4% Ca/ZnO synthesized via wet impregnation. C_2 product yields are roughly comparable to CO yields over Ca-ZnO, while CO yields are 50 and 10 times greater than the C_2 product yields over ZnO and 0.4% Ca/ZnO, respectively. The rates of product formation over Ca-ZnO are stable with time on stream for at least the 4 hours measured. The product yields continually change over the 0.4% Ca/ZnO catalyst. We hypothesize that the Ca sites formed during ion-exchange are highly disperse, yielding maximum Ca-ZnO interface sites. These sites may be resistant to sintering and thus highly stable. The Ca loading of the Ca-ZnO catalyst and the Ca site structure was not studied here, but that information could inform on the catalytic performance of highly disperse Ca sites over ZnO.

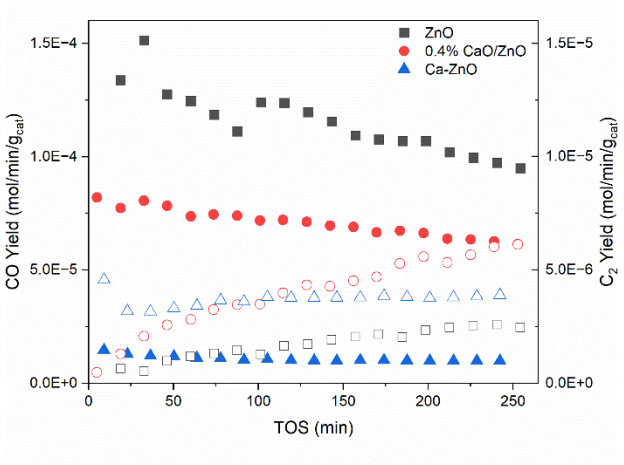

Figure 4.10. CO (filled) and C_2 (hollow) product rates of ion-exchanged Ca-ZnO compared to pure ZnO and 0.4% Ca/ZnO. 850 °C; 100 mg catalyst; 13.3 mL min^{-1} total gas flow rate with P_{CH_4} = 0.25 atm, P_{CO_2} = 0.5 atm, P_{N_2} = 0.25 atm.

Another synthesis method explored is the wet impregnation of zinc oxide onto CaO. The comparison between 50% CaO/ZnO and 50% ZnO/CaO is shown in Figure 4.11. Identical synthesis procedures were followed, except for the change of precursors. We hypothesized that different interfacial sites would form by swapping the support, independent of catalyst composition. Higher C_2 product yield and selectivity are achieved over the CaO/ZnO catalyst than ZnO/CaO. This may result from the blocking of ZnO reforming sites on the catalyst surface by CaO species. ZnO/CaO exhibits higher stability over at least the 4 hours of time on stream measured. The reason for this is currently unknown. Characterization of these catalysts *in situ* and after reaction would inform on the catalyst structure changes during reaction. The difference in catalytic performance between these two catalysts demonstrates that CO_2-OCM activity is not only composition-dependent but dependent on CaO/ZnO interface structure.

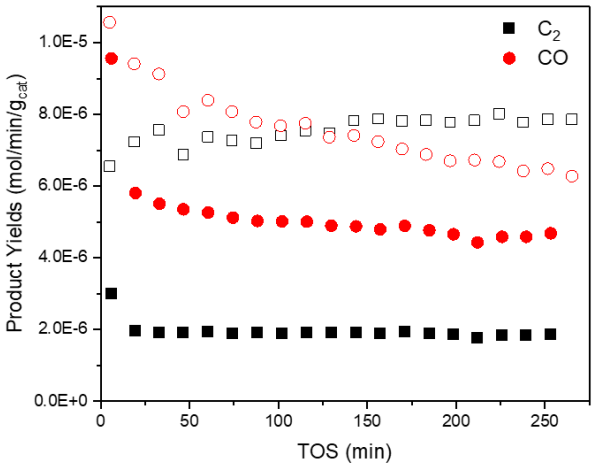

Figure 4.11. Effect of synthesis order on product yields with 50% CaO/ZnO (hollow) and 50% ZnO/CaO (filled). 850 °C; 100 mg catalyst; 13.3 mL min^{-1} total gas flow rate with P_{CH_4} = 0.25 atm, P_{CO_2} = 0.5 atm, P_{N_2} = 0.25 atm.

The catalytic OCM performance was evaluated over the stable 50% ZnO/CaO catalyst. Reactant conversion and product selectivity is shown in Figure 4.12 at times on stream less than 150 minutes. CO and CO_2 were the dominant products formed with ca. 10% ethane selectivity and negligible ethylene formation. 50% ZnO/CaO catalyzes methane oxidation more effectively than methane coupling. The addition of CO_2 to OCM reactant feeds has been reported to enhance C_2 selectivity.[2,3] After 150 minutes on

stream, half of the oxygen in the reactor feed was replaced with CO_2 to be at a O_2/CO_2 ratio of 1. Methane and O_2 conversions significantly dropped. Ethane selectivity increased slightly while ethylene selectivity remained negligible. CO selectivity increased, but some of the CO originates from CO_2 dissociation rather than methane oxidation making determination of methane coupling activity difficult. CO_2 production is no longer able to be quantified.

Product yields and selectivities directly comparing OCM and CO_2-OCM are shown in Figure 4.13 to further quantify the significance of CO_2 on the reaction rates. Here, C_2 selectivity during CO_2-OCM is defined as the fraction of C_2 products in the total product stream, and CO selectivity is the fraction of CO in the total product stream resulting from both methane oxidation and CO_2 dissociation. Despite quantifying the total product output and not only the products formed from methane, lower C_2 product yield and higher C_2 product selectivity were attained during CO_2-OCM compared to OCM. Oxygen can more effectively activate methane, leading to higher conversion, but it also leads to lower C_2 product selectivities due to methane and hydrocarbon oxidation.[27] The addition of CO_2 to the OCM feed (≥150 min) does improve the C_2 product selectivity compared to the absence of CO_2. The C_2 product yield and selectivity is higher during CO_2-OCM without any oxygen present in the feed than with a co-feed of oxidants. Pure CO_2 as the oxidant enhances C_2 selectivity likely by limiting overoxidation.

CO_2-OCM was performed at 850 °C while OCM was performed at 650 °C. CaO/ZnO catalysts are not active for CO_2-OCM at 650 °C, while secondary reactions like oxidation and dehydrogenation become dominant during OCM at 850 °C. This temperature difference may also influence the distribution and concentration of surface intermediates. Carbonate may be stable in higher concentrations at 650 °C. Reactant feed concentrations also differ to avoid a flammable reaction mixture during OCM. Direct comparisons of reactions that are very endothermic and exothermic is difficult for these reasons. Comparing product yields and selectivities at similar methane conversions may be the best future course of action. The results presented here are only valid over a catalyst with bulk CaO; evaluating the influence of oxidant concentrations over a catalyst with lower Ca concentration, and CaO clusters, may provide different results.

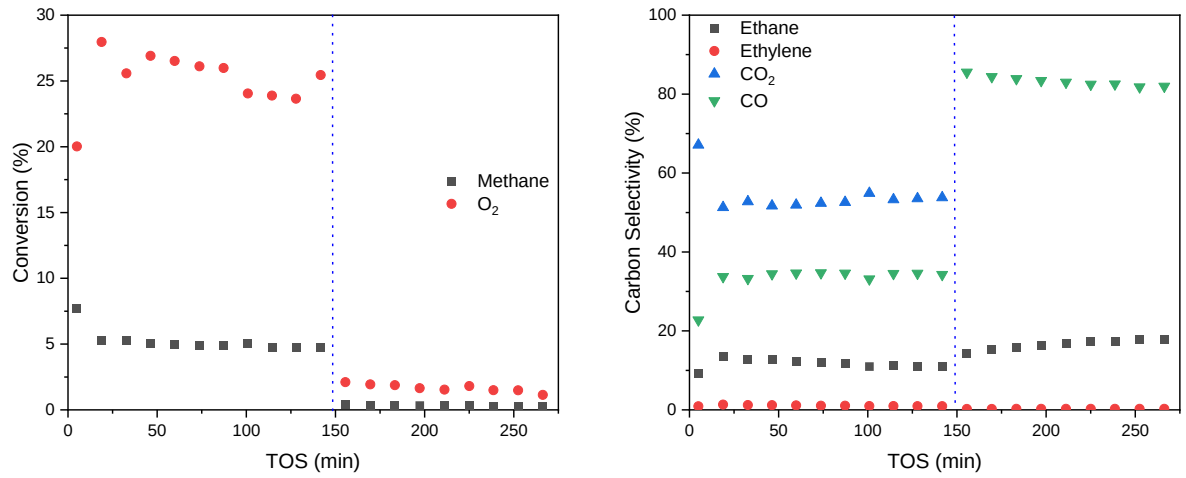

Figure 4.12. OCM performance of 50% ZnO/CaO without and with CO_2. 650 °C, 0.1 g catalyst, 20 mL/min total flow rate with P_{CH_4} = 0.2 atm, P_{O_2} = 0.04 atm, P_{N_2} = 0.76 atm. After 150 min on stream flow was changed to P_{CH_4} = 0.2 atm, P_{O_2} = 0.02 atm, P_{CO_2} = 0.02 atm, P_{N_2} = 0.76 atm.

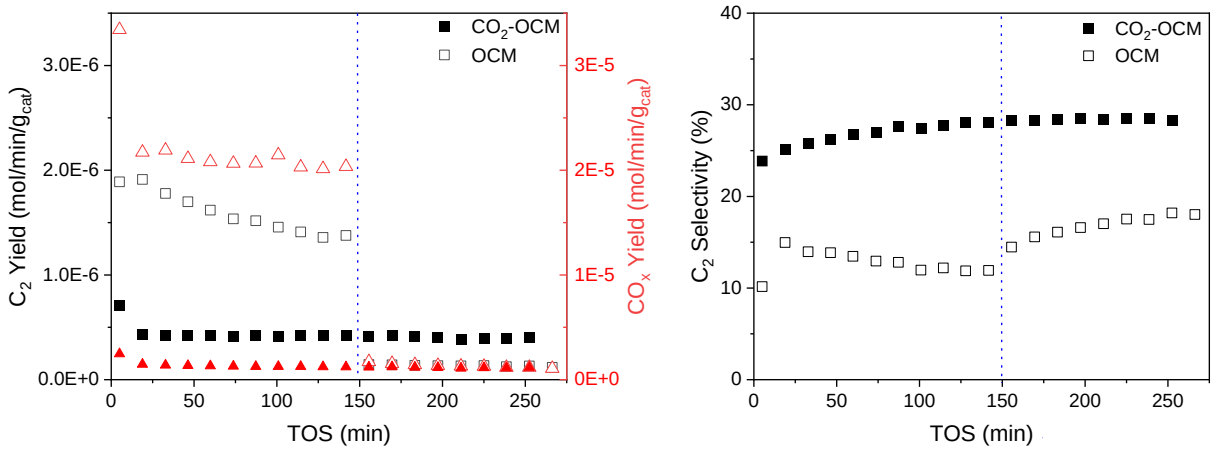

Figure 4.13. OCM performance of 50% ZnO/CaO without (hollow) and with CO_2 (filled) compared to CO_2-OCM performance.

Instead of using a fixed O_2/CO_2 ratio of 1, as shown above, we hypothesize that a lower composition of O_2 in the feed could reduce the overoxidation of hydrocarbons and improve C_2 product selectivity and yields. A range of O_2/CO_2 ratios from 0 to 0.8 were used in Figure 4.14. Introduction of a small amount of O_2 (O_2/CO_2 = 0.03) decreases CO yields, likely due to a decrease in the amount of CO_2 being reduced to CO during CO_2-OCM. CO yields further decrease a slightly higher O_2 concentrations O_2/CO_2 = 0.09 but then rise again when O_2/CO_2 = 0.8. The increase at a ratio close to 1 can be attributed to an increase in the extent of alkane oxidation occurring with higher O_2 concentrations. Addition of O_2 to CO_2-OCM increases the overall C_2 product yields. At O_2/CO_2 ratios ≥ 0.09, ethylene yields surpass those of ethane. The extent of ethane dehydrogenation increases in more oxidative reaction environments.[28] Conditions with O_2 present seem to result in more stable product signals with time on stream than under pure CO_2-OCM. Inability to quantify methane reforming product CO and oxidation product CO_2 prevents the determination of the reaction orders of O_2 or CO_2. The use of a low-Ca-loading catalyst and higher reaction temperatures to prevent stable carbonate formation limit the extent of comparisons between this data and Figures 4.12-13.

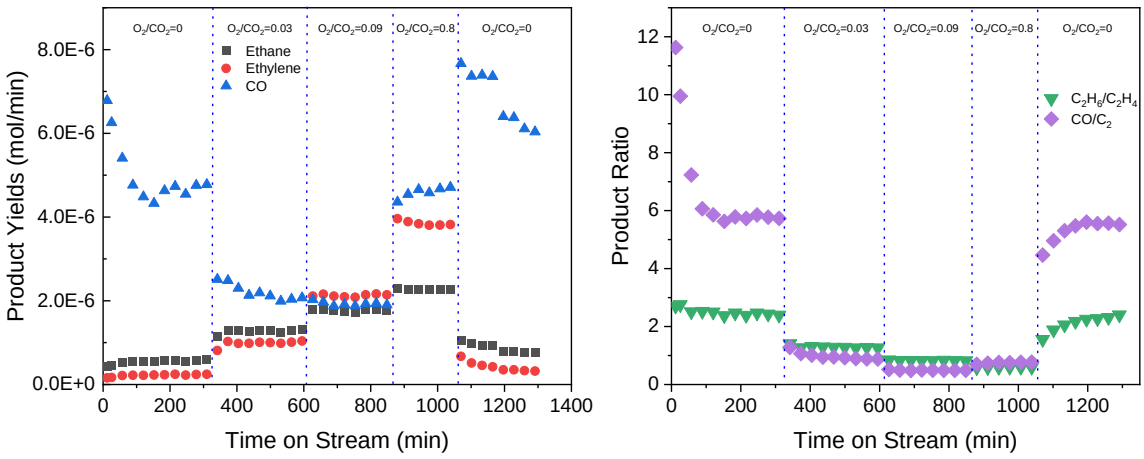

Figure 4.14. Effect of oxygen partial pressure on product distribution and yields during CO_2-OCM over 2% Ca/ZnO. 850 °C; 100 mg catalyst; 13.3 mL min^{-1} total gas flow rate with P_{CH_4} = 0.25 atm and balance nitrogen.

A CO_2-OCM "light-off" curve was developed by increasing the reaction temperature while flowing the typical reactant gas stream to assess catalytic performance as a function of temperature over 2% Ca/ZnO, shown in Figure 4.15. No conversion was detected in absence of a catalyst. Non-zero methane conversion was first measured at 700 °C. This coincides with the temperature where calcium carbonate decomposes, potentially supporting the inhibition of methane activation by adsorbed CO_2, as reported.[29] Low-temperature methane conversion is moderately selective to C_2 product formation but increasing temperature in the range of 700-800 °C promotes CO formation via methane reforming. At temperatures above 800 °C, methane coupling begins to outcompete methane reforming. This may be due to the higher enthalpy of reaction of CO_2-OCM than methane reforming.[30] The rate of ethane dehydrogenation is observed to increase with temperature.

Using a similar procedure to that in Figure 4.15 but with a standard OCM reactant feed, methane conversion was first observed over both Ca/ZnO and Li/MgO at 600 °C – a temperature lower than the light-off of CO_2-OCM – in Figure 4.16. At this temperature, higher methane and O_2 conversions are observed over Ca/ZnO than Li/MgO. Lower C_2 product selectivity is observed over Ca/ZnO than during CO_2-OCM and compared to Li/MgO, a well-recognized OCM catalyst. Alkanes could be more susceptible to subsequent oxidation over the Ca/ZnO catalyst for a number of reasons; notably, Ca/ZnO could more strongly bind hydrocarbon intermediates to the catalyst surface where further C-H activation occurs, or a lower concentration of generated methyl radical in the gas phase could lead to a higher probability of reaction with gaseous O_2. It is not possible at this time to conclusively state why lower C_2 product selectivity is observed here. Like CO_2-OCM, the extent of ethane dehydrogenation increases with temperature over both catalysts.

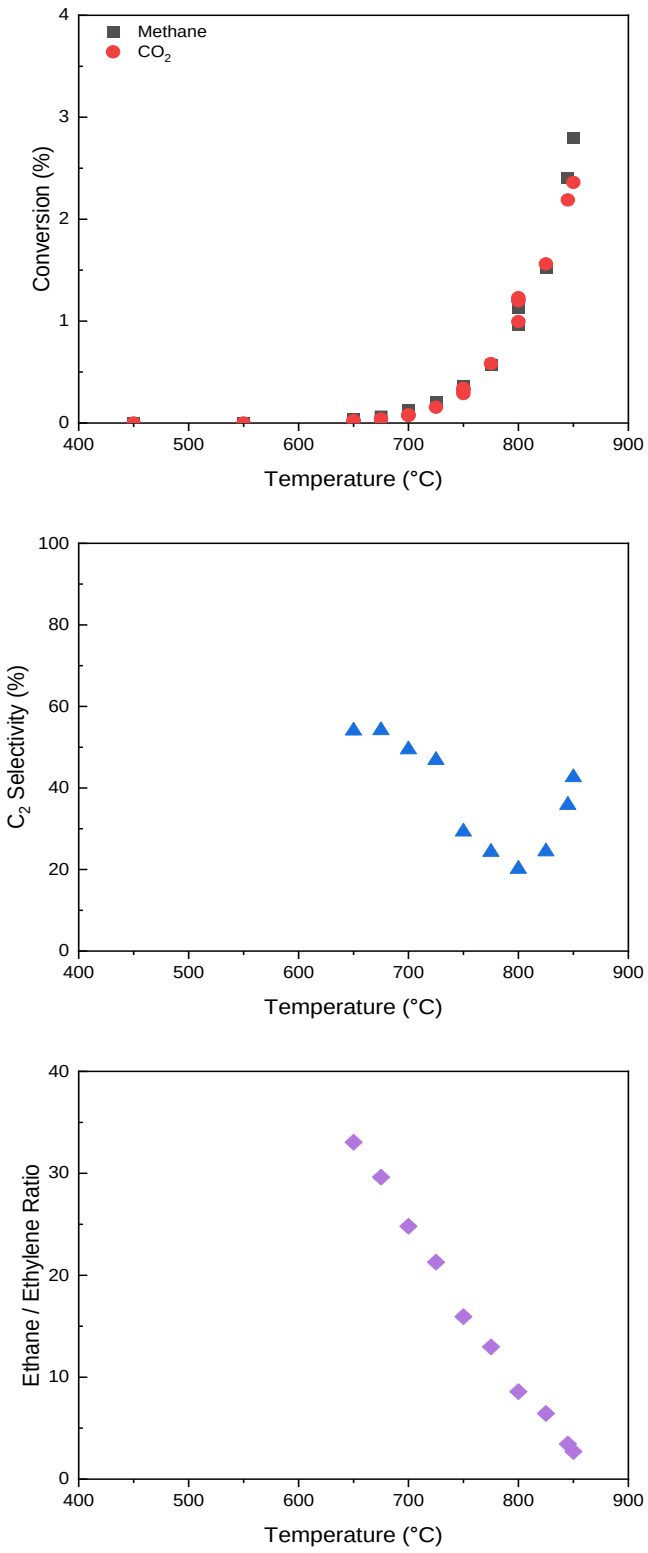

Figure 4.15. Effect of temperature ramp during CO_2-OCM over 2% Ca/ZnO. 100 mg catalyst; 13.3 mL min^{-1} total gas flow rate with P_{CH_4} = 0.25 atm, P_{CO_2} = 0.5 atm, P_{N_2} = 0.25 atm, ramp rate of 2 °C/min. Held for 30 min at each temperature prior to data collection.

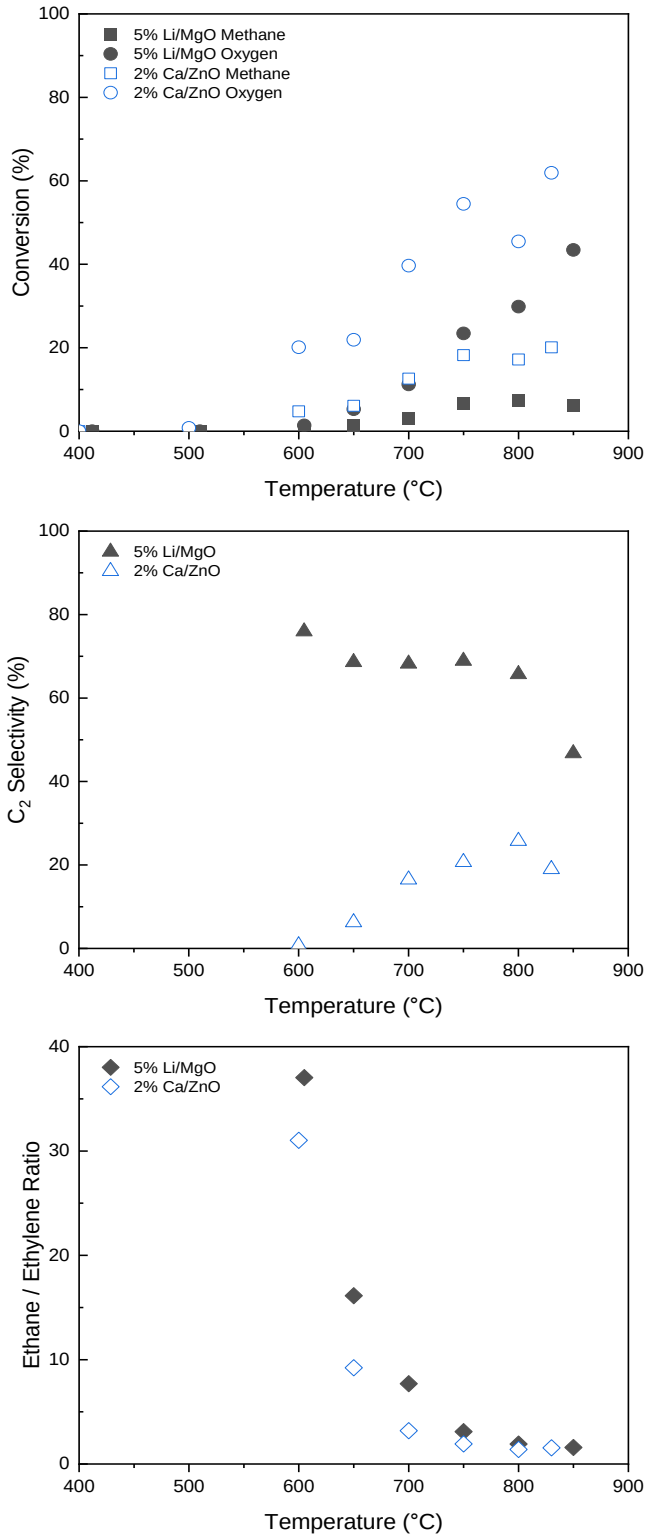

Figure 4.16. Effect of temperature ramp during OCM. 100 mg catalyst; 20 mL min^{-1} total gas flow rate with P_{CH_4} = 0.2 atm, P_{O_2} = 0.04 atm, P_{N_2} = 0.76 atm, ramp rate of 2 °C/min. Held for 30 min at each temperature prior to data collection. *In situ* calcination at 850 °C (ramp rate of 5 °C/min) for 10 min in 5% O_2 prior to reaction.

The natural log of methane conversions and product yields measured during the CO_2-OCM and OCM temperature ramps (Figures 4.15-16) were plotted against temperature to determine activation energies over 2% Ca/ZnO. During the CO_2-OCM temperature ramp, methane conversion remained below 2%, suggesting the reactor was in a differential regime. Here in Figure 4.17a, the activation energy measured for ethane formation was 173 ± 18.2 kJ/mol whereas that for CO formation via methane reforming was 200 ± 4.5 kJ/mol, where the error values are from deviations from the linear fit of the data. These values are very similar, but the activation energy of ethane formation is statistically lower than that of CO formation, supporting the observation that Ca/ZnO is a selective CO_2-OCM catalyst. The activation energy is also consistent with that measured for N_2O-OCM over 1% Ca/ZnO.

During the OCM temperature ramp, the reactor quickly left a differential regime since higher methane conversions were achieved at lower temperatures. The data from the 2 lowest temperatures where conversion was below 5%, highlighted in green in Figure 4.17b, were used to calculate the activation energies of ethane formation to be 170 kJ/mol, CO formation to be 148 kJ/mol, and CO_2 formation to be 206 kJ/mol. This is consistent with the observation that partial methane combustion to CO and methane coupling are favored at lower temperatures, but higher temperature favors complete oxidation. Comparing activation energies between the two reactions demonstrates that C_2 product formation may more readily occur during OCM, but there is also higher chance of oxidation to CO_x.

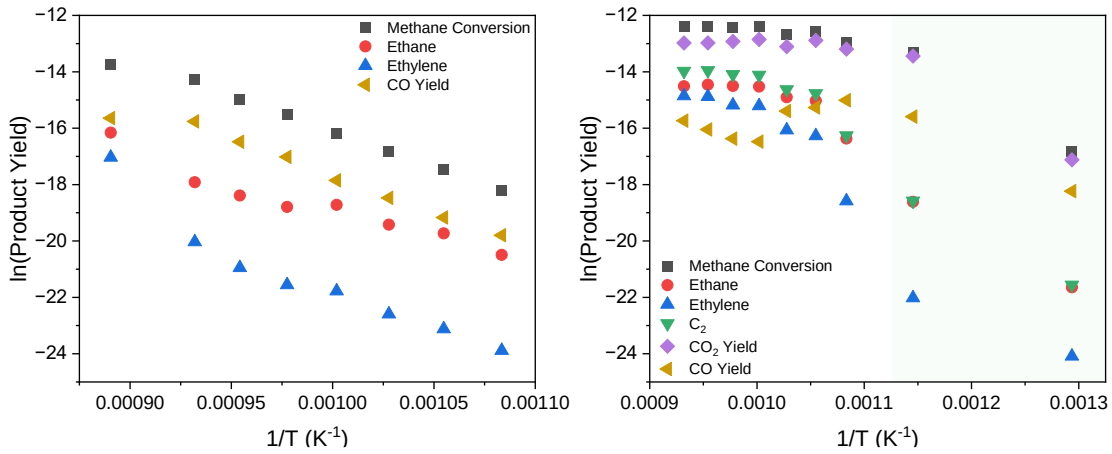

Figure 4.17. Arrhenius plots derived from temperature ramps during CO_2-OCM (left) and OCM (right) over 2% Ca/ZnO where product yield is measure in mol/s/g_{cat}.

A 1 wt% Pd/MgO catalyst has been reported to effectively catalyze methanol oxidation to oxygenated products, including the rarely observed methoxymethanol.[12] Due to its ability to activate C_1 species, the catalyst was evaluated for its OCM activity, shown in Figure 4.18. A significantly lower methane conversion light-off temperature of 350 °C was observed, compared to the Ca/ZnO catalysts. However, only oxidation products – CO and CO_2 – were observed in abundance. At temperatures lower than 500 °C, a very small amount of C_2 products were observed, but the rate of C_2 product formation quickly drops to near-zero as temperature and conversion increase. Isothermal conversion of methane at 650 °C produces an increasing concentration of CO_x products and decreasing concentration of C_2 products with time on stream. At these high temperatures and conversions, the C-H activation of C_2 products becomes more facile.[31]

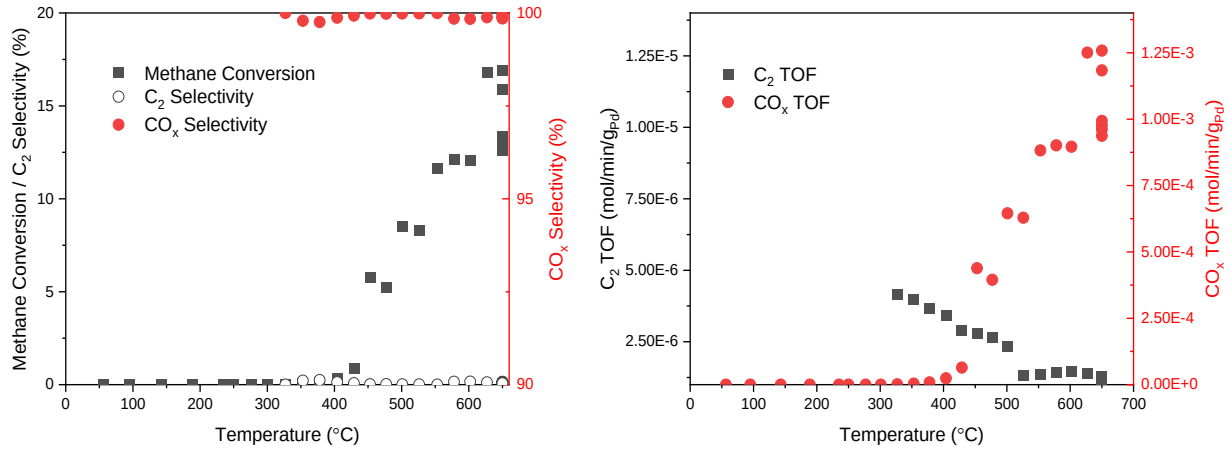

Figure 4.18. Effect of temperature ramp during OCM over 1% Pd/MgO. 0.1 g catalyst; 10 mL min^{-1} total gas flow rate with P_{CH_4} = 0.2 atm, P_{O_2} = 0.04 atm, P_{N_2} = 0.76 atm, ramp rate of 2 °C/min. Held for 30 min at each temperature prior to data collection. *In situ* calcination at 400 °C (ramp rate of 5 °C/min) for 2 h in air prior to reaction.

The OCM performances of other MgO-supported metals were also evaluated using the well-characterized 0.05 wt% Pt/MgO, where Pt is known to exist as isolated cations in the subsurface layer of MgO near a magnesium point-vacancy.[11] Initially, a CH_4/O_2 ratio of 5 was flowed over the catalyst, where higher methane conversion was observed over the Pt/MgO catalyst than 5% Li/MgO. A conversion of ~12% is comparable to that achieved by Pd/MgO in Figure 4.18. Interestingly, similar conversions were achieved with 20 times lower noble metal loading. At 100 minutes of time on stream, the reactant flowrate was doubled with a CH_4/O_2 ratio of 2.5. This change in reactant flows dramatically increased the methane conversion over Pt/MgO, but little change was observed over Li/MgO. At 200 minutes on stream, the reactor temperature was gradually cooled to 350 °C to determine if the Pt/MgO catalyst was catalytically active at low temperatures, like had been reported for Pd/CeO_2.[32] No activity below 500 °C was observed.

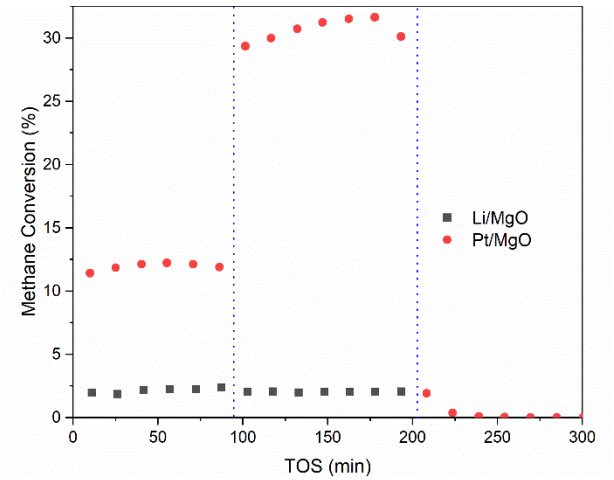

Figure 4.19. Methane conversion of MgO-supported catalysts during OCM. Initial conditions: 0.2 g catalyst; 650 °C; 20 mL min^{-1} total gas flow rate with P_{CH_4} = 0.2 atm, P_{O_2} = 0.04 atm, P_{N_2} = 0.76 atm. At 100 min flow was changed to 40 mL min^{-1} total gas flow rate with P_{CH_4} = 0.1 atm, P_{O_2} = 0.04 atm, P_{N_2} = 0.86 atm. At 200 min the temperature began cooling to 350 °C.

The product yields and selectivities of OCM over Li/MgO and Pt/MgO, above, are shown in Figure 4.20, where selectivity is defined on a carbon-basis. Over Pt/MgO, all methane was oxidized into CO_x species. An increase in the concentration of CO formed relative to CO_2 was observed at 100<t<200 minutes on stream, which is likely due to the increase in the reactant space velocity. Moderate ethane selectivity and yield were observed over Li/MgO. Increasing the space velocity and O_2 concentration resulted in a higher concentration of CO_x species and lower concentration of C_2 products due to oxidation.

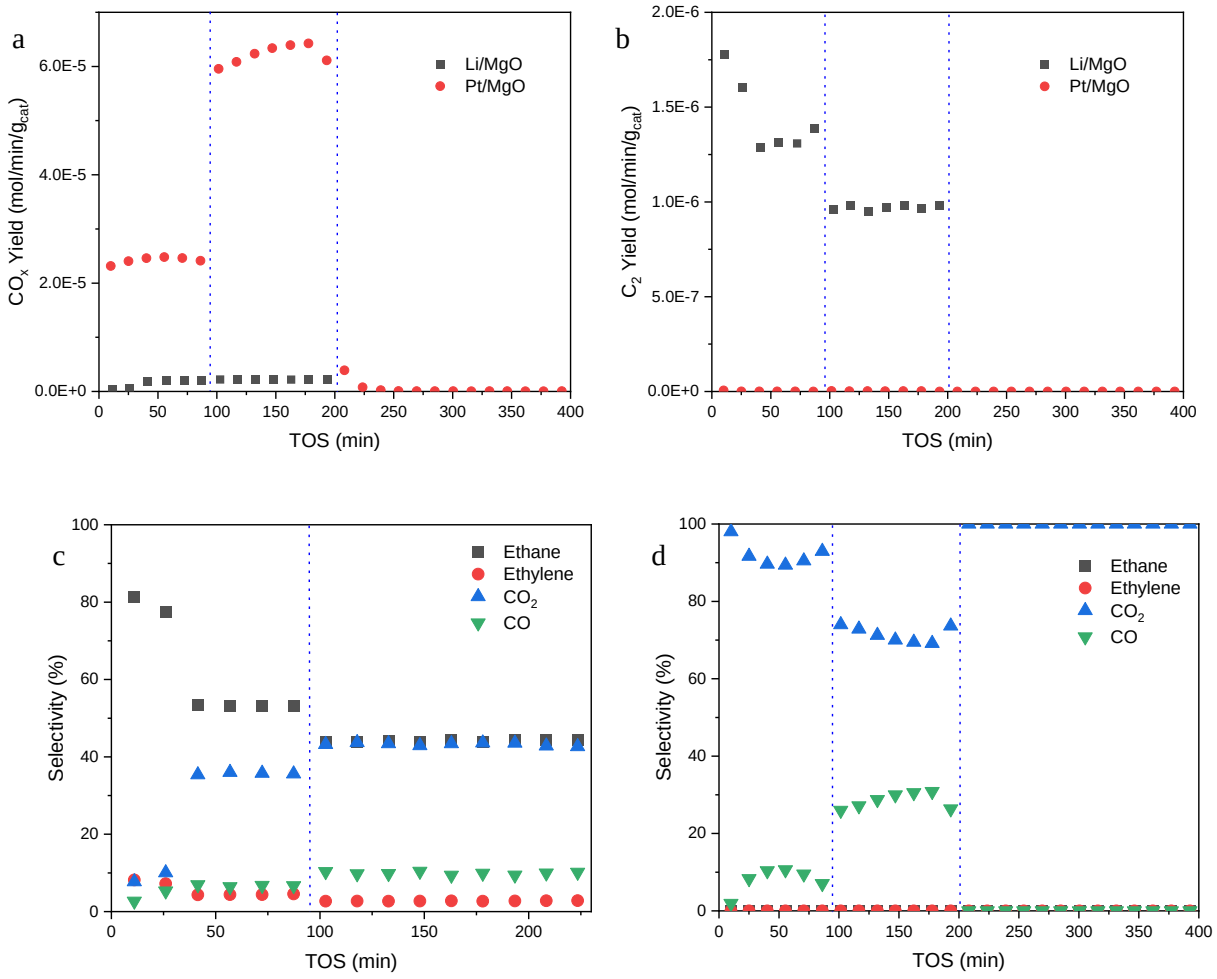

Figure 4.20. (a-b) Product yields of MgO-supported catalysts during OCM, and product selectivities over (c) 5% Li/MgO and (d) 0.05% Pt/MgO. Initial conditions: 0.2 g catalyst; 20 mL min^{-1} total gas flow rate with P_{CH_4} = 0.2 atm, P_{O_2} = 0.04 atm, P_{N_2} = 0.76 atm. At 100 min flow was changed to 40 mL min^{-1} total gas flow rate with P_{CH_4} = 0.1 atm, P_{O_2} = 0.04 atm, P_{N_2} = 0.86 atm. At 200 min the temperature began cooling to 350 °C.

Catalyst Characterization after CO_2 Adsorption and Reaction

The Ca/ZnO catalysts were thoroughly characterized in Chapters 2 and 3. Here, we present additional characterization results of the initial and final states after CO_2-OCM. The basicity of binary metal oxide CO_2-OCM catalysts strongly affects the catalytic performance.[33] CO_2-TPD was attempted to qualitatively characterize the types of basic sites by the number and shape of peaks observed, and quantitatively determine relative concentrations of each by peak areas. Figure 4.21 shows the mass loss and CO_2 mass spectrometer signal during CO_2-TPD over 35% Ca/ZnO and 2% Ca/ZnO. Over the 35% Ca/ZnO catalyst, one main peak at ~550 °C is observed. The presence of a singular peak with a slow rising edge at > 500 °C in the MS signal is consistent with Ca/ZnO catalysts.[21,34] This confirms the presence of strongly basic sites corresponding to the large CaO particles present. The temperature of CO_2 desorption is slightly higher than that observed in Figures 2.4 and 2.5 due to the faster ramp rate. No distinguishable features are observed in the mass loss or MS profiles over the 2% Ca/ZnO catalyst. The concentration of basic sites is too low to detect an appreciable signal. This constraint that prevented the characterization of the low Ca loading catalysts prompted the development of the IR-TPD method of characterization CO_2 desorption specifically at the catalyst surface.

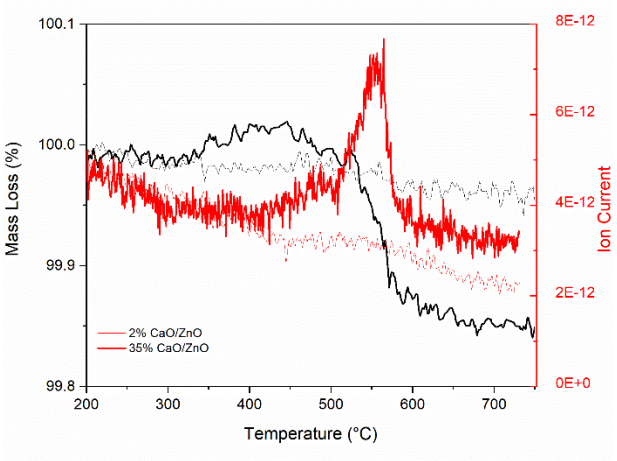

Figure 4.21. CO_2-TPD using TGA after CO_2 adsorption at room temperature, monitoring mass loss of sample and the MS signal for m/z = 44 corresponding to CO_2 while heating at 10 °C min^{-1}.

Ca L-edge XANES was reported for freshly calcined Ca/ZnO catalysts in Figure 2.3. Here, the Ca L-edge XANES spectra of the catalysts after undergoing CO_2-OCM are compared to the fresh catalysts in Figure 4.22. The changes in line shape after reaction – sharpened t_{2g} and the presence of two new pre-edge peaks around 347.3-348.3 eV – indicate the transformation of CaO to a $CaCO_3$ phase.[13,35] The e_g peaks are shifted to higher energy compared to the fresh catalysts in the high Ca loading catalysts, which is characteristic of $CaCO_3$. However, the peaks of the low Ca loading catalysts do not shift and now present at lower energy than the high Ca loading catalysts. This may be a result of the different density of states of the surface Ca atoms compared to those in the bulk phase, similar to that for the Ca K-edge simulations in Figure 3.5. XANES simulations like those in Chapter 3 would be required to definitively conclude this.

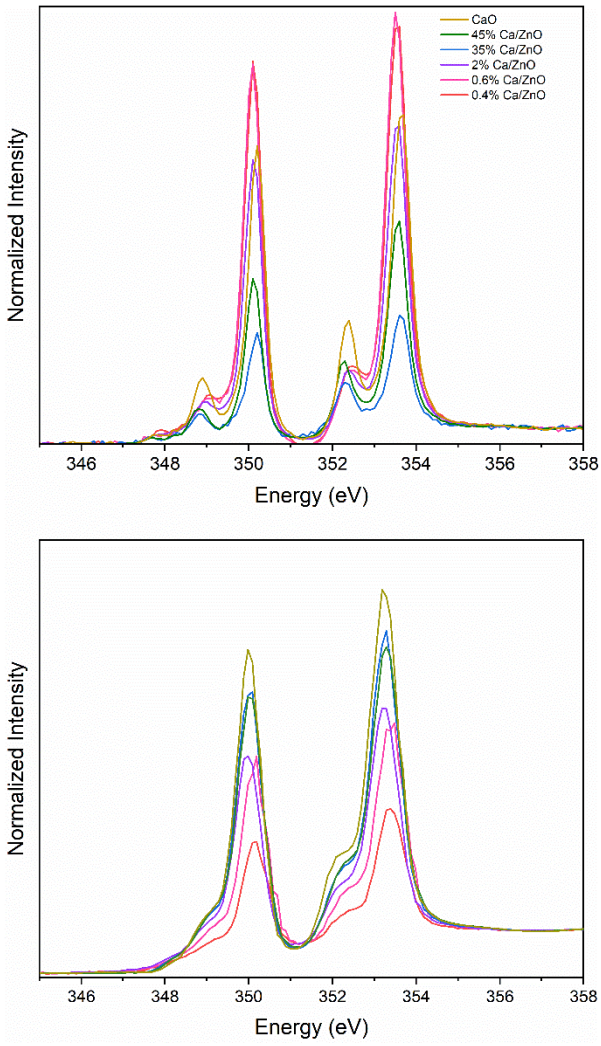

Figure 4.22. Ca L-edge XANES of Ca/ZnO catalysts (top) after CO_2-OCM and (bottom) before.

The transformation of CaO to $CaCO_3$ after CO_2-OCM is more easily demonstrated by the comparison of the 2% Ca/ZnO before and after reaction in Figure 4.23. The shift to higher energy and narrowing of the peaks becomes more noticeable. Using CTM4XAS simulation package, these changes associated with carbonation of the catalyst surface can be captured by increasing the crystal field splitting parameter 10Dq from 0.6 to 1.1. CaO and $CaCO_3$ both have 6-coordinate octahedral geometry.[36] Therefore, this change in crystal field splitting can be explained by the more oxidizing CO_3^{2-} ligand replacing the O^{2-} ligand. This is roughly consistent with reported calcium carbonate 10Dq value of 1.5. [37]

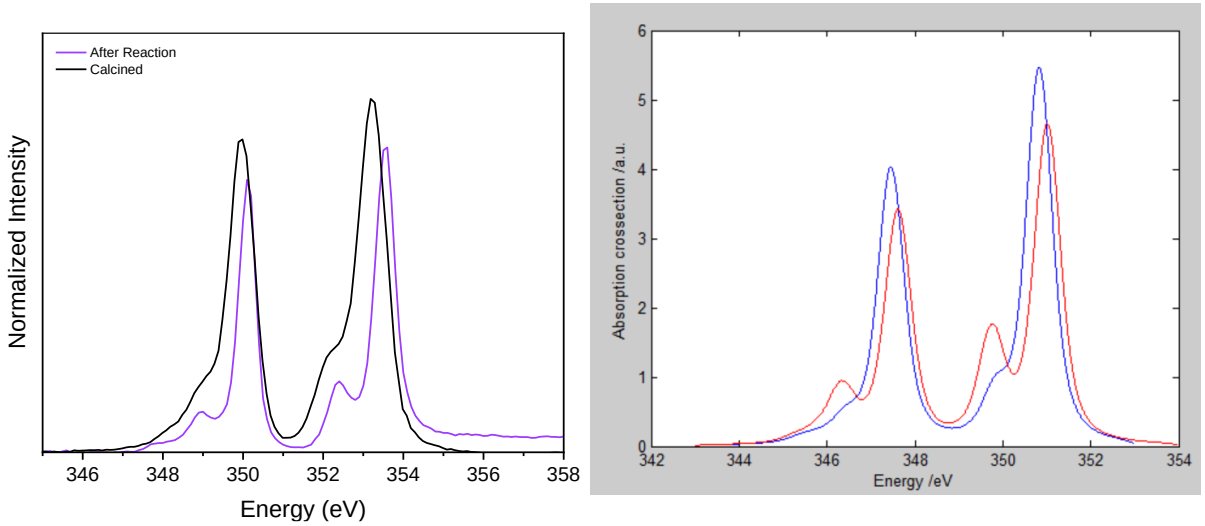

Figure 4.23. Comparison of Ca L-edge XANES spectra (left) before and after CO_2-OCM over 2% Ca/ZnO, and (right) simulated spectra with 10Dq values of 0.6 and 1.1 in blue and red, respectively.

XANES spectra of the O K-edge of the Ca/ZnO catalysts before and after CO_2-OCM are shown in Figure 4.24. Fresh catalysts with ≤ 2% Ca only exhibit spectral features consistent with pure ZnO. As Ca content increases, the spectra resemble a linear combination of ZnO and CaO. Since all 3d orbitals of ZnO are occupied, only peaks corresponding to oxygen 2p hybridization with Zn 4sp states are present.[38] After reaction, the ZnO spectrum does not change. The CaO spectra corresponds to that of $CaCO_3$,[13] consistent with Ca L-edge XANES results. Again, the spectra of the high Ca loading catalysts are a linear combination of ZnO and $CaCO_3$ spectra. Spectra of the low Ca loading catalysts still resemble that of ZnO, but the carbonate π^* peak around 534 eV[39] is present in even the 0.4% Ca/ZnO catalyst, suggesting even the CaO

clusters undergo some degree of carbonation during reaction. This is especially noticeable when comparing spectra of the catalysts before and after reaction (Figure 4.24c-d)

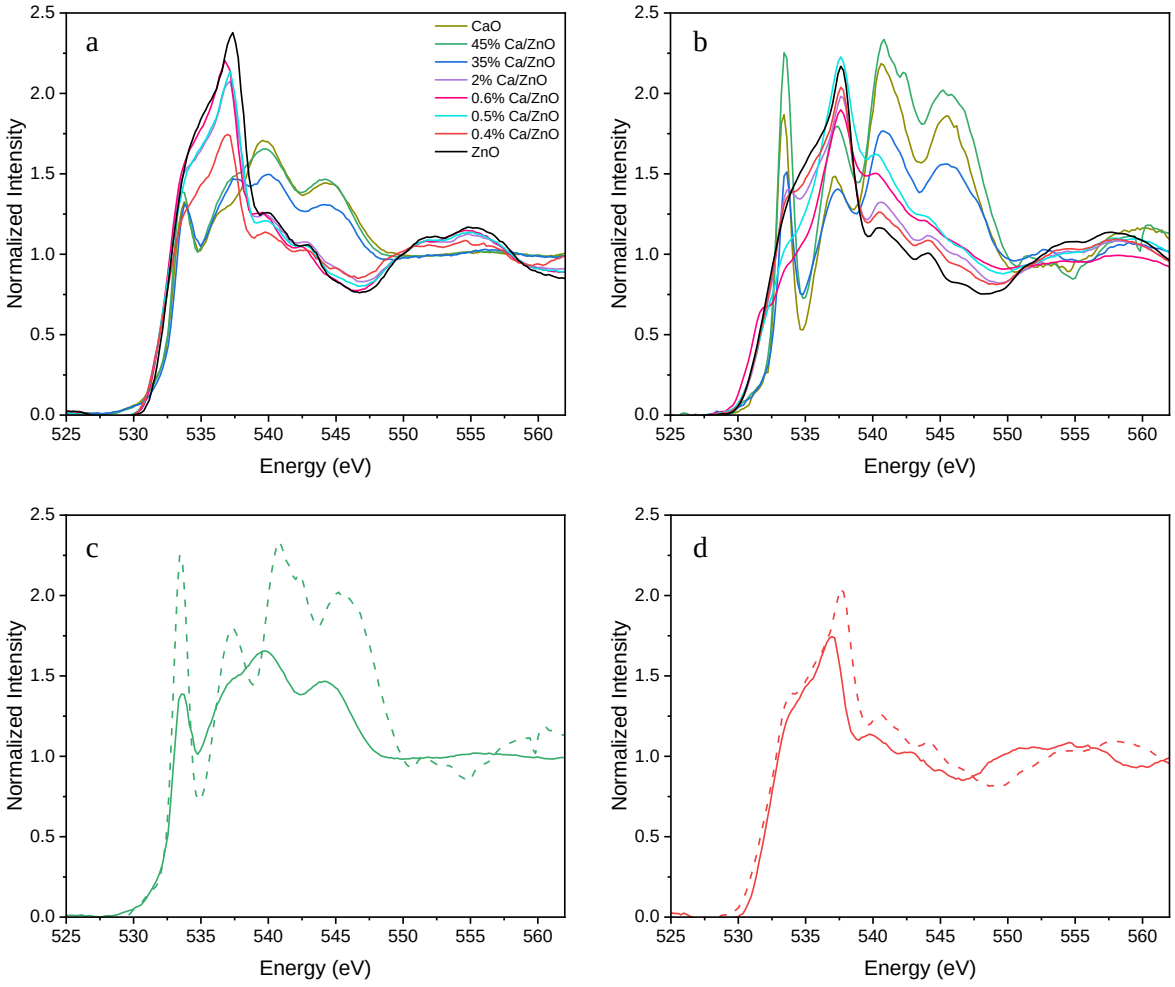

Figure 4.24. O K-edge XANES of Ca/ZnO catalysts (a) before and (b) after CO_2-OCM. Comparison of spectra before (solid) and after (dotted) CO_2-OCM for (c) 45% Ca/ZnO and (d) 0.4% Ca/ZnO.

SEM images of the 5% Li/MgO OCM catalyst used in Figures 4.19-20 inform if and how the average particle size and morphology change before and after calcination and reaction. Directly after synthesis and oven drying at 80 °C, the particles consist of ultra-thin sheets with a diameter on the order of a 1-2 μm densely packed into large aggregates. After calcination at 850 °C, the particles were no longer sheets but more cubic with a large deviation in size, ranging from 0.2 to 2 μm. Significantly more particle sintering occurred during OCM, increasing the average particle size and decreasing its surface area.

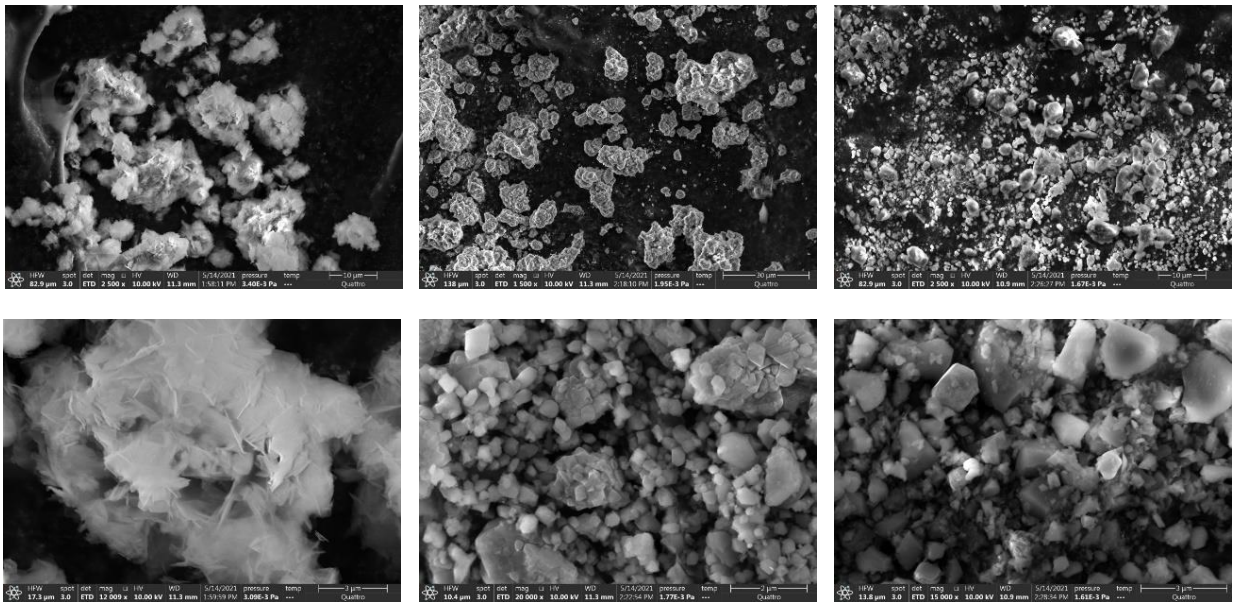

Figure 4.25. SEM images of 5% Li/MgO (left) as prepared after drying, (middle) after calcination, and (right) after OCM. Bottom row is at higher magnification than top.

Exploration of Morphology Dependence of CO_2-OCM over Ca/ZnO Catalysts

An interesting property of ZnO as a support is its easily tunable morphology.[40] Hexagonal ZnO preferentially grows along the c-axis during hydrothermal synthesis,[41] changing the aspect ratio (length/width) of particles with time. Capping agents like sodium citrate can preferentially bind to the (001) facet, preventing growth along the c-axis.[41] The catalytic performances of ZnO-supported catalysts have been demonstrated to be dependent on morphology.[42,43] Chapter 2 concludes that the interface between Ca and ZnO is critical for CO_2-OCM performance. The structure of ZnO at that interface may have an important impact on reactivity. Here, ZnO of varying aspect ratios – plates, rods, and commercial – were hydrothermally synthesized and used in 2% Ca wet impregnation. The CO_2-OCM performance of these catalysts are compared in Figure 4.26. The catalyst mass-normalized product yields over the rod and commercial morphologies are identical. The C_2 product yield over the plate morphology was also similar to the others, but its CO yield was drastically less. The plate-shaped catalysts achieved a much higher selectivity toward C_2 products.

The catalysts have different surface areas due to their different morphologies which impact product yields. The surface area of the ZnO rods was measured to be 21.0 ± 0.4 m^2/g, and that of the commercial ZnO was 7.3 ± 0.1 m^2/g. The surface area of the ZnO plates was not measured. The product yields were then normalized by exposed catalyst surface area rather than mass (Figure 4.26b). Rod-shaped catalysts have significantly lower activity for both CO and C_2 production than the commercial ZnO catalyst. The lower activity could be attributed to the higher density of the exposed (100) facet. It is a non-polar surface, electronically balanced between O^{2-} and Zn^{2+} species,[44] which may lead to less reactivity. Contrarily, the (001) facet dominant in the plate-shaped catalyst may be the reason for higher C_2 product selectivity. It is currently unknown to what extent the catalytic activity of the ZnO surface is controlled and the morphology is affecting the structure of the active Ca/ZnO interface. It has been demonstrated that polar surfaces of ZnO can create strong metal-support interactions between the (002) facet of ZnO and cationic Cu, [42] where ZnO morphology affects its reforming activity.[45] The variation in facets in the commercial ZnO catalyst may result in more dispersed CaO nanoparticles than on ZnO rods, which would have improved CO_2-OCM performance, as demonstrated in Chapters 2 and 3. Further characterization of the catalysts after calcium deposition and after reaction could elucidate any differences in active site structure over different morphologies.

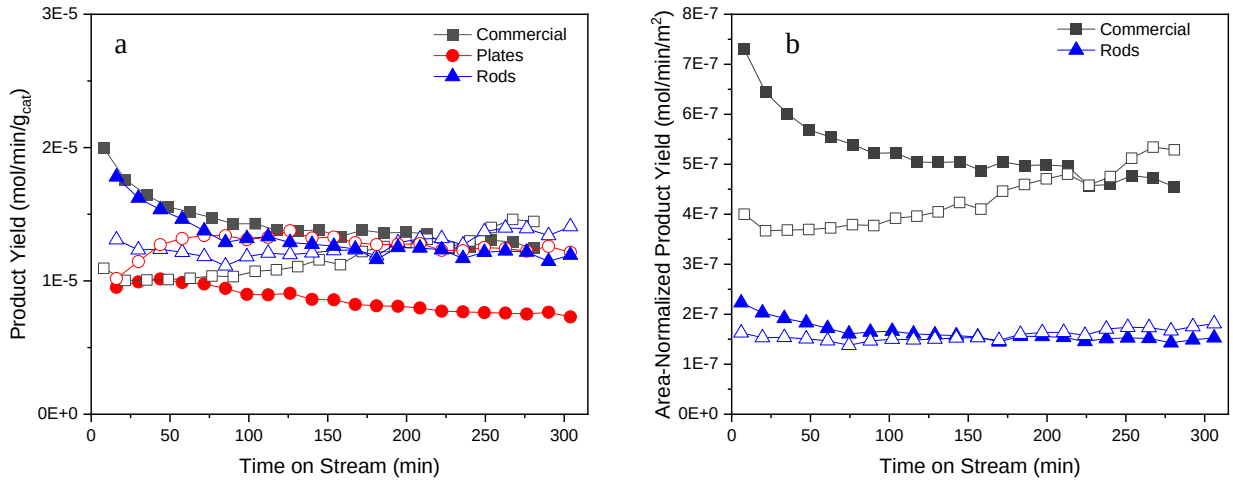

Figure 4.26. CO_2-OCM performance of 2% Ca/ZnO with varying ZnO morphologies (a) before and (b) after normalizing CO (filled) and C_2 (hollow) product yields by catalyst surface areas. 850 °C; 100 mg catalyst; 13.3 mL min^{-1} total gas flow rate with P_{CH_4} = 0.25 atm, P_{CO_2} = 0.5 atm, P_{N_2} = 0.25 atm.

SEM images of the 2% Ca/ZnO catalysts with varying morphologies after CO_2-OCM are shown in Figure 4.27. The plates mostly maintain their hexagonal structure but become rounder and larger along the c-axis, making them less plate-like. The rods also become more rounded and decrease in length, decreasing the particle aspect ratio. Catalysts made with commercial ZnO significantly sinter into much larger, rounded particles. They maintain having a lower surface area than the rods after reaction. The rounding of the catalysts edges may indicate a higher reactivity of undercoordinated atoms.

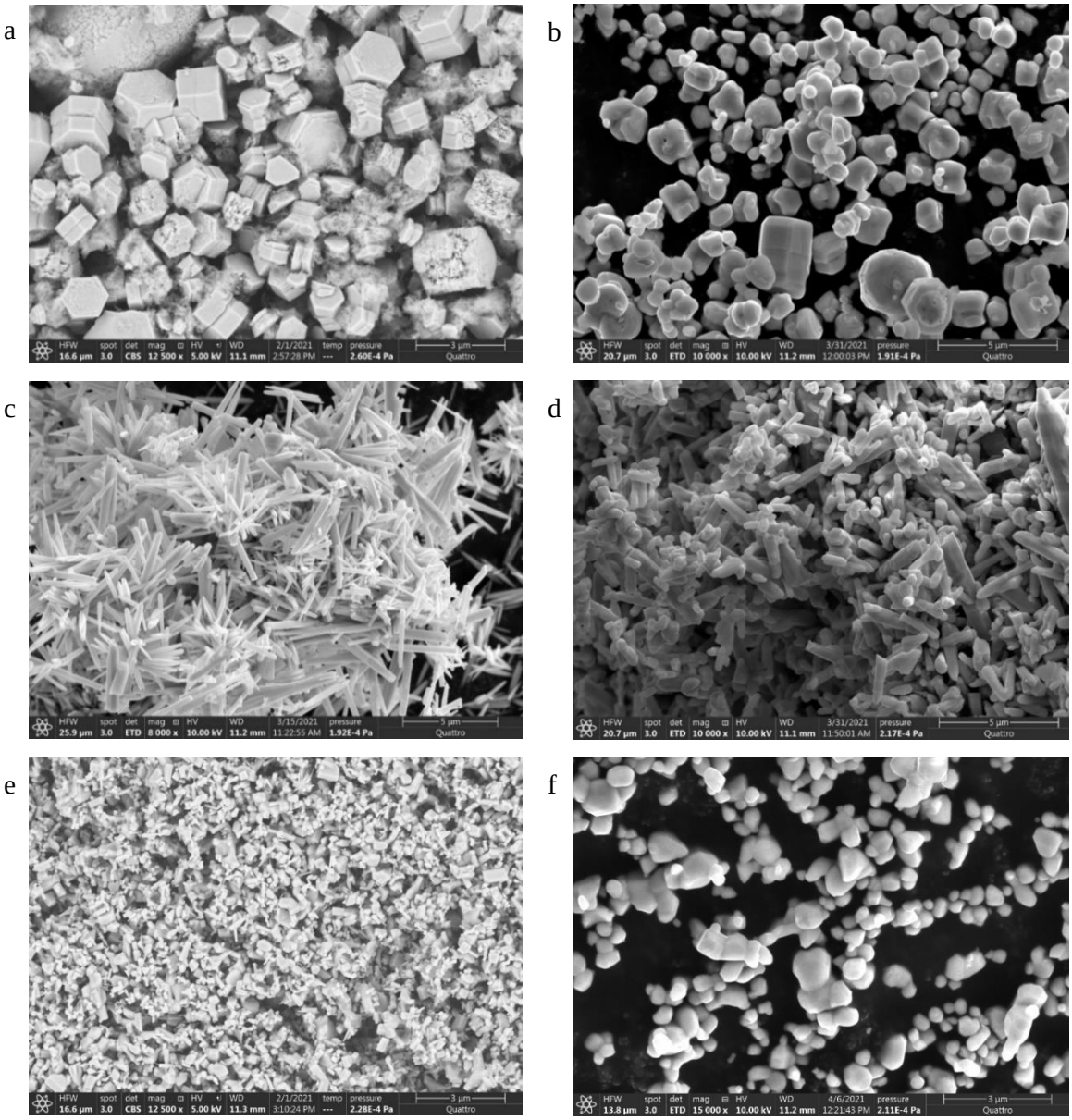

Figure 4.27. SEM images of hydrothermally synthesized ZnO with morphologies of (a) plates, (c) rods, and (e) the commercially available ZnO; (b,d,f) after wet impregnation of 2% Ca and CO_2-OCM.

Exploration of Ethane Reactivity over Methane Coupling Catalysts

Ethane, the primary product of methane coupling reactions, undergoes oxidative dehydrogenation during the reaction to form ethylene. Specialized techniques like VUV-PIMS[46] and TAP[31] allow for the *in situ* study of the ethane dehydrogenation reaction. Here, a Ca/ZnO catalyst was evaluated for its ability to catalyze ethane dehydrogenation with CO_2 (CO_2-EDH). The activity of 0.1 g of 0.6% Ca/ZnO was contrasted to that of 2.8 g solid inert Al_2O_3. The rate of ethylene production over the Ca/ZnO catalyst was on the same order of magnitude as the solid inert, indicating that the catalyst is not highly active for EDH. More methane was produced over the catalyst experiment, indicating that hydrocarbon cracking is more prevalent. However, this could simply be due to the homogenous gas-phase reaction at this temperature.[47]

Experimental limitations on reactant flowrates prevented a simulation of EDH consistent with CO_2-OCM conditions. A better metric of the extent of dehydrogenation occurring is the ethylene-to-ethane ratio exiting the reactor. Less than 1 of every 2 ethane molecules dehydrogenates to ethylene during CO_2-OCM, while 3 of 4 ethane molecules dehydrogenate during CO_2-EDH. The discrepancy in ethylene-to-ethane ratio during the two reactions is most probably caused by a significantly larger partial pressure of ethane, 0.02 atm, during EDH compared to what is produced during CO_2-OCM, 0.001 atm. The extend of dehydrogenation that occurs suggests that a combination of surface-mediated and gas-phase EDH is likely occurring during CO_2-OCM, with no way of deconvoluting these two pathways currently. The effect of ethane partial pressure likely plays a large role in the rate of dehydrogenation.

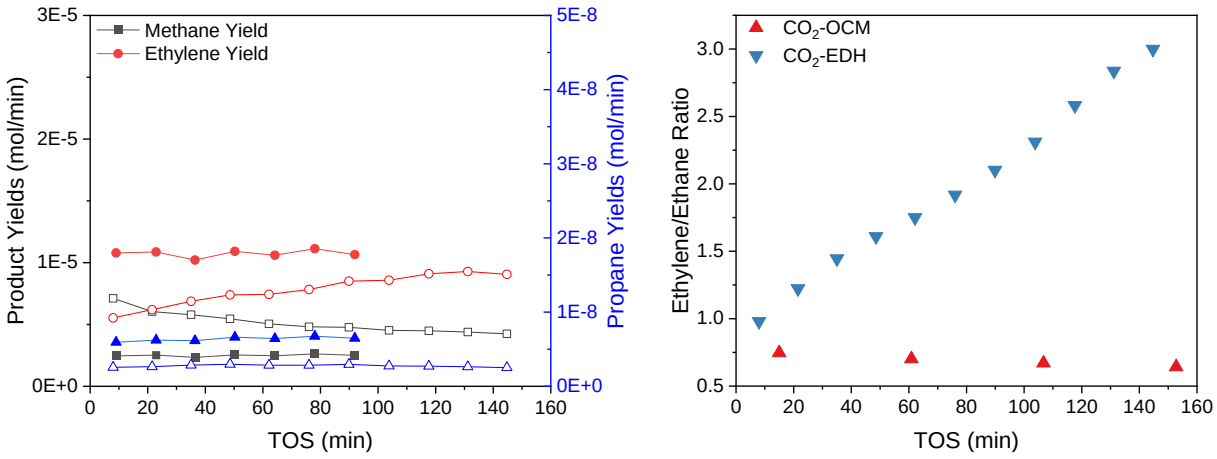

Figure 4.28. (Left) Product yields of CO_2-EDH over 0.1 g of 0.6% Ca/ZnO (hollow) and 2.8 g alumina (filled). 13.3 mL/min total flow, $P_{C_2H_6}$ = 0.02 atm, P_{CO_2} = 0.5 atm, P_{N_2} = 0.48 atm, 850 °C. Lines are included to guide the eye. (Right) Comparison of ethylene/ethane ratio during CO_2-DH and CO_2-OCM.

C_3 species are generated during CO_2-EDH and N_2O-OCM (Figures 4.28 and 3.6), which forms by further coupling of C_2 species. There are two coupling routes to form C_3 products: methyl radicals further couple with existing C_2 species in the gas phase, or C_4 species generated from C_2 oligomerization crack into methane and C_3 products. Methane had been reported to couple with C_2 species over zeolite-supported silver catalysts.[48,49] Attempts to reproduce these results with silver or other transition metals on ZSM-5 were unsuccessful. Instead, products were observed using a traditional methane coupling catalyst Li/MgO.[50] Very low product signals were detected at 650 °C due to the highly endothermic nature of this non-oxidative reaction.[51] However, at this temperature, the concentration of C_4 products was higher than that of C_3 products with no measurable methane conversion, tentatively supporting the initial generation of C_4 species from C_2 oligomerization. There is a minor increase in product signal detected with a higher Li content in the catalyst, likely due to the increase in F center active sites.[52] As temperature is increased and conversions increase, the concentration of C_3 products now exceed that of C_4 species, likely due to cracking which is more favorable at higher temperatures.[53] With data over a wider range of conversions, the relationship between product selectivity and conversion would more accurately be able to address this hypothesis. However, the presence of an oxidant could drastically affect the reaction network observed here.

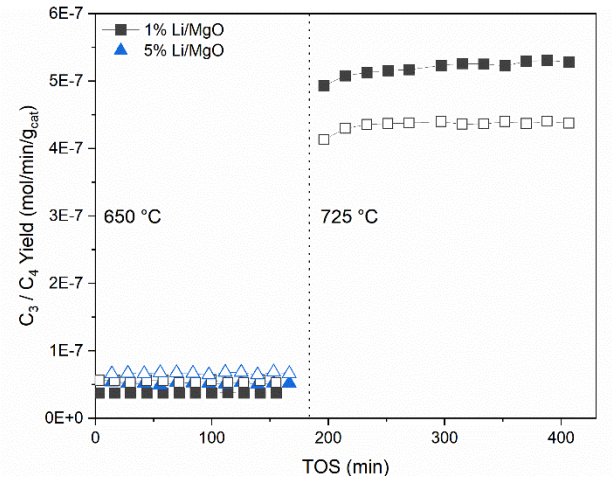

Figure 4.29. C_3 (filled) and C_4 (hollow) product yields from alkane coupling with methane and ethane over Li/MgO catalysts. 50 mg catalyst, 50 mL/min total flow, $P_{C_2H_6}$ = 0.1 atm, P_{CH_4} = 0.1 atm, P_{N_2} = 0.8 atm. Lines are included to guide the eye.

4.5 Conclusion

The work in this chapter probes the influence of both reaction conditions and physical properties of Ca/ZnO catalysts on reaction kinetics and product distributions over several related light alkane upgrading reactions – CO_2-OCM, N_2O-OCM, OCM, and ethane DH. Probing the kinetics of N_2O-OCM reveals a positive reaction order for C_2 and CO_x product formation on N_2O composition and a dependence on active site structure. Similar experiments with CO_2-OCM yield a strong dependence of C_2 yields on CO_2 concentration in the feed. Over Ca/ZnO catalysts, the activation energy for ethane formation is lower than that for CO formation during CO_2-OCM, but the activation energy for ethane formation is higher than for methane oxidation during OCM at similar conditions. Ca L-edge XANES of Ca/ZnO catalyst before and after CO_2-OCM are contrasted to reveal calcium carbonate formation in all catalysts after reaction, including the low-Ca-loading catalyst where ultra-small one- or two-dimensional clusters were shown to exist. Varying ZnO morphologies – plates and rods – synthesized hydrothermally were used as the catalyst supports for 2 mol% Ca deposition. The CO_2-OCM performance of these catalysts was compared to catalysts with the commercially available ZnO. The 2% Ca on commercially available ZnO catalyzed high C_2 product yields, indicating the dependence of reactivity on exposed ZnO crystal facet. Performing CO_2-assisted ethane

dehydrogenation over 0.6% Ca/ZnO revealed that the reaction does take place, but the catalyst is not significantly active. Non-oxidative coupling of methane and cracking of C_{2+} products is negligible at similar conditions.

These results suggest that future investigation into these reaction systems should quantify the strong influence of stable intermediates, like carbonate, on reaction kinetics, and experimentally determine kinetic parameters for methane coupling that are independent of carbonate coverage. These kinetic parameters may be compared across different oxidants over the same catalytic active site. These results provide preliminary insights to mechanism determination and the influence of active site structure on reaction kinetics for methane coupling reactions. The similarities and differences between CO_2-, N_2O-, and O_2-assisted methane coupling can inform future catalyst and reactor design for optimizing methane upgrading with greenhouse gases.

4.6 References

(1) Ortiz-Bravo, C. A.; Chagas, C. A.; Toniolo, F. S. Oxidative Coupling of Methane (OCM): An Overview of the Challenges and Opportunities for Developing New Technologies. J Nat Gas Sci Eng 2021, 96, 104254.

(2) Aika, K. I.; Nishiyama, T. Utilisation of CO2 in the Oxidative Coupling of Methane over PbO-MgO and PbO-CaO. J. Chem. Soc., Chem. Commun. 1988, No. 1, 70–71.

(3) Wang, D.; Xu, M.; Shi, C.; Lunsford, J. H. Effect of Carbon Dioxide on the Selectivities Obtained during the Partial Oxidation of Methane and Ethane over Li^+/MgO Catalysts. Catal Letters 1993, 18 (4), 323–328.

(4) Hutchings, G. J.; Scurrell, M. S.; Woodhouse, J. R. Partial Oxidation of Methane over Samarium and Lanthanum Oxides: A Study of the Reaction Mechanism. Catal Today 1989, 4 (3–4), 371–381.

(5) Roguleva, V. G.; Nikiphorova, M. A.; Maksimov, N. G.; Anshits, A. G. Oxidative Coupling of Methane over Li/CaO Catalysts Using O_2 and N_2O as Oxidants. Catal Today 1992, 13 (2), 219–226.

(6) Driscoll, D. J.; Martir, W.; Wang, J. X.; Lunsford, J. H. Formation of Gas-Phase Methyl Radicals Over MgO. J Am Chem Soc 1985, 107 (1), 58–63.

(7) Filardi, L. R.; Yang, F.; Guo, J.; Kronawitter, C. X.; Runnebaum, R. C. Surface Basicity Controls C–C Coupling Rates during Carbon Dioxide-Assisted Methane Coupling over Bifunctional Ca/ZnO Catalysts. Physical Chemistry Chemical Physics 2023, 25 (14), 9859–9867.

(8) Mirghiasi, Z.; Bakhtiari, F.; Darezereshki, E.; Esmaeilzadeh, E. Preparation and Characterization of CaO Nanoparticles from $Ca(OH)_2$ by Direct Thermal Decomposition Method. J. Ind. Eng. Chem. 2014, 20 (1), 113–117.

(9) Das, S.; Dutta, K.; Pramanik, A. Morphology Control of ZnO with Citrate: A Time and Concentration Dependent Mechanistic Insight. CrystEngComm 2013, 15 (32), 6349–6358.

(10) Ito, T.; Wang, J.-X.; Lin, C.-H.; Lunsford, J. H. Oxidative Dimerization of Methane over a Lithium-Promoted Magnesium Oxide Catalyst. J. Am. Chem. Soc 1985, 107, 5062–5068.

(11) Chen, Y.; Rana, R.; Sours, T.; Vila, F. D.; Cao, S.; Blum, T.; Hong, J.; Hoffman, A. S.; Fang, C. Y.; Huang, Z.; Shang, C.; Wang, C.; Zeng, J.; Chi, M.; Kronawitter, C. X.; Bare, S. R.; Gates, B. C.; Kulkarni, A. R. A Theory-Guided X-Ray Absorption Spectroscopy Approach for Identifying Active Sites in Atomically Dispersed Transition-Metal Catalysts. J Am Chem Soc 2021, 143 (48), 20144–20156.

(12) Gurses, S. M.; Price, T.; Zhang, A.; Frank, J. H.; Hansen, N.; Osborn, D. L.; Kulkarni, A.; Kronawitter, C. X. Near-Surface Gas-Phase Methoxymethanol Is Generated by Methanol Oxidation over Pd-Based Catalysts. Journal of Physical Chemistry Letters 2021, 12 (46), 11252–11258.

(13) Patel, M.; Aswath, P. B. Morphology, Structure and Chemistry of Extracted Diesel Soot: Part II: X-Ray Absorption near Edge Structure (XANES) Spectroscopy and High Resolution Transmission Electron Microscopy. Tribol. Int. 2012, 52, 17–28.

(14) Chen, S. C.; Sung, K. Y.; Tzeng, W. Y.; Wu, K. H.; Juang, J. Y.; Uen, T. M.; Luo, C. W.; Lin, J. Y.; Kobayashi, T.; Kuo, H. C. Microstructure and Magnetic Properties of Oxidized Titanium Nitride Thin Films in Situ Grown by Pulsed Laser Deposition. J Phys D Appl Phys 2013, 46 (7), 075002.

(15) Yamamoto, H.; Chu, H. Y.; Xu, M.; Shi, C.; Lunsford, J. H. Oxidative Coupling of Methane over a Li^+/MgO Catalyst Using N_2O as an Oxidant. J Catal 1993, 142 (1), 325–336.

(16) Snis, A.; Strömberg, D.; Panas, I. N_2O Adsorption and Decomposition at a CaO(100) Surface, Studied by Means of Theory. Surf Sci 1993, 292 (3), 317–324.

(17) Zhang, H.; Wang, W.; Li, L.; Liu, J. Starch-Assisted Synthesis and Characterization of Layered Calcium Hydroxide Particles. J Inorg Organomet Polym Mater 2018, 28 (6), 2399–2406.

(18) Da Silveira Petruci, J. F.; Wilk, A.; Cardoso, A. A.; Mizaikoff, B. A Hyphenated Preconcentrator-Infrared-Hollow-Waveguide Sensor System for N_2O Sensing. Sci Rep 2018, 8 (1).

(19) Philipp, R.; Fujimoto, K. FTIR Spectroscopic Study of CO_2 Adsorption/Desorptlon on MgO/CaO Catalysts. J. Phys. Chem. 1992, 96 (22), 9035–9038.

(20) Low, M. J. D.; Yang, R. T. Reactions of Gaseous Pollutants with Solids: V. Infrared Study of the Sorption of NO on CaO. J Catal 1974, 34 (3), 479–489.

(21) Wang, Y.; Ohtsuka, Y. CaO-ZnO Catalyst for Selective Conversion of Methane to C_2 Hydrocarbons Using Carbon Dioxide as the Oxidant. J. Catal. 2000, 192 (1), 252–255.

(22) Wang, Y.; Takahashi, Y.; Ohtsuka, Y. Carbon Dioxide as Oxidant for the Conversion of Methane to Ethane and Ethylene Using Modified CeO_2 Catalysts. J. Catal. 1999, 186 (1), 160–168.

(23) Nguyen, T. D.; Zheng, W.; Celik, F. E.; Tsilomelekis, G. CO2-Assisted Ethane Oxidative Dehydrogenation over MoO_x Catalysts Supported on Reducible CeO_2–TiO_2. Catal Sci Technol 2021, 11 (17), 5791–5801.

(24) Bown, R. M.; Joyce, M.; Zhang, Q.; Reina, T. R.; Duyar, M. S. Identifying Commercial Opportunities for the Reverse Water Gas Shift Reaction. Energy Technology 2021, 9 (11), 2100554.

(25) Tasioula, M.; de Clermont Gallerande, E.; Theofanidis, S. A.; Longo, A.; Lomachenko, K. A.; Sahle, C.; Lemonidou, A. A. Tandem CO_2 Valorization and Ethane Dehydrogenation: Elucidating the Nature of Highly Selective Iron Oxide Active Sites. ACS Catal 2023, 13 (4), 2176–2189.

(26) Guo, J.; Liu, H.; Li, D.; Wang, J.; Djitcheu, X.; He, D.; Zhang, Q. A Minireview on the Synthesis of Single Atom Catalysts. RSC Adv 2022, 12 (15), 9394.

(27) Lee, J. S.; Oyama, S. T. Comments on the Mechanism of Oxidative Coupling of Methane. Reaction Kinetics & Catalysis Letters 1990, 41 (2), 257–263.

(28) Wang, X. Ethane Dehydrogenation for Light Olefins Production Over Stable Catalyst, West Virginia University, Morgantown, 2022.

(29) Thum, L.; Rudolph, M.; Schomäcker, R.; Wang, Y.; Tarasov, A.; Trunschke, A.; Schlögl, R. Oxygen Activation in Oxidative Coupling of Methane on Calcium Oxide. Journal of Physical Chemistry C 2019, 123 (13), 8018–8026.

(30) Cai, X.; Hu, Y. H. Advances in Catalytic Conversion of Methane and Carbon Dioxide to Highly Valuable Products. Energy Sci Eng 2019, 7 (1), 4–29.

(31) Sourav, S.; Wang, Y.; Kiani, D.; Baltrusaitis, J.; Fushimi, R. R.; Wachs, I. E. New Mechanistic and Reaction Pathway Insights for Oxidative Coupling of Methane (OCM) over Supported Na_2WO_4/SiO_2 Catalysts. Angew. Chem Int. Ed. 2021, 60, 21502–21511.

(32) Kwon, G.; Shin, D.; Jeong, H.; Sahoo, S. K.; Lee, J.; Kim, G.; Choi, J.; Kim, D. H.; Han, J. W.; Lee, H. Oxidative Methane Conversion to Ethane on Highly Oxidized Pd/CeO_2 Catalysts Below 400 °C. ChemSusChem 2020, 13 (4), 677–681.

(33) Wang, Y.; Ohtsuka, Y. Mn-Based Binary Oxides as Catalysts for the Conversion of Methane to C_2 Hydrocarbons with Carbon Dioxide as Oxidant. Appl. Catal. A 2001, 219 (1–2), 183–193.

(34) Alba-Rubio, A. C.; Santamaría-González, J.; Mérida-Robles, J. M.; Moreno-Tost, R.; Martín-Alonso, D.; Jiménez-López, A.; Maireles-Torres, P. Heterogeneous Transesterification Processes by Using CaO Supported on Zinc Oxide as Basic Catalysts. Catal. Today 2010, 149, 281–287.

(35) Naftel, S. J.; Sham, T. K.; Yiu, Y. M.; Yates, B. W. Calcium L-Edge XANES Study of Some Calcium Compounds. J. Synchrotron Rad 2001, 8, 255–257.

(36) Martin-Diaconescu, V.; Gennari, M.; Gerey, B.; Tsui, E.; Kanady, J.; Tran, R.; Pécaut, J.; Maganas, D.; Krewald, V.; Gouré, E.; Duboc, C.; Yano, J.; Agapie, T.; Collomb, M.-N.; DeBeer, S. Ca K-Edge XAS as a Probe of Calcium Centers in Complex Systems. Inorg Chem 2015, 54 (4), 1283–1292.

(37) Calcium $L_{2,3}$-Edge XANES of Carbonates, Carbonate Apatite, and Oldhamite (CaS). American Mineralogist 2009, 94, 1235–1241.

(38) Guo, J. H.; Vayssieres, L.; Persson, C.; Ahuja, R.; Johansson, B.; Nordgren, J. Polarization-Dependent Soft-x-Ray Absorption of Highly Oriented ZnO Microrod. Journal of Physics: Condensed Matter 2002, 14 (28), 6969.

(39) Frati, F.; Hunault, M. O. J. Y.; De Groot, F. M. F. Oxygen K-Edge X-Ray Absorption Spectra. 2020.

(40) Kolodziejczak-Radzimska, A.; Jesionowski, T. Zinc Oxide-from Synthesis to Application: A Review. Materials 2014, 7 (4), 2833–2881.

(41) Tian, Z. R.; Voigt, J. A.; Liu, J.; Mckenzie, B.; Mcdermott, M. J. Biomimetic Arrays of Oriented Helical ZnO Nanorods and Columns. J Am Chem Soc 2002, 124 (44), 12954–12955.

(42) Liao, F.; Huang, Y.; Ge, J.; Zheng, W.; Tedsree, K.; Collier, P.; Hong, X.; Tsang, S. C. Morphology-Dependent Interactions of ZnO with Cu Nanoparticles at the Materials' Interface in Selective Hydrogenation of CO_2 to CH_3OH. Angew. Chem. Int. Ed. 2011, 50 (9), 2162–2165.

(43) Zhang, H.; Sun, J.; Dagle, V. L.; Halevi, B.; Datye, A. K.; Wang, Y. Influence of ZnO Facets on Pd/ZnO Catalysts for Methanol Steam Reforming. ACS Catal 2014, 4 (7), 2379–2386.

(44) Mora-Fonz, D.; Lazauskas, T.; Farrow, M. R.; Catlow, C. R. A.; Woodley, S. M.; Sokol, A. A. Why Are Polar Surfaces of ZnO Stable? Chemistry of Materials 2017, 29 (12), 5306–5320.

(45) Karim, A. M.; Conant, T.; Datye, A. K. Controlling ZnO Morphology for Improved Methanol Steam Reforming Reactivity. Physical Chemistry Chemical Physics 2008, 10 (36), 5584–5590.

(46) Luo, L.; You, R.; Liu, Y.; Yang, J.; Zhu, Y.; Wen, W.; Pan, Y.; Qi, F.; Huang, W. Gas-Phase Reaction Network of Li/MgO-Catalyzed Oxidative Coupling of Methane and Oxidative Dehydrogenation of Ethane. ACS Catal 2019, 9 (3), 2514–2520.

(47) Heracleous, E.; Lemonidou, A. A. Homogeneous and Heterogeneous Pathways of Ethane Oxidative and Non-Oxidative Dehydrogenation Studied by Temperature-Programmed Reaction. Appl Catal A Gen 2004, 269 (1–2), 123–135.

(48) Baba, T.; Sawada, H. Conversion of Methane into Higher Hydrocarbons in the Presence of Ethylene over H-ZSM-5 Loaded with Silver Cations. Physical Chemistry Chemical Physics 2002, 4 (15), 3919–3923.

(49) Hsieh, M.-F.; Zhou, Y.; Thirumalai, H.; Grabow, L. C.; Rimer, J. D. Silver-Promoted Dehydroaromatization of Ethylene over ZSM-5 Catalysts. ChemCatChem 2017, 9 (9), 1675–1682.

(50) Lunsford, J. H.; Qiu, P.; Rosynek, M. P.; Yu, Z. Catalytic Conversion of Methane and Ethylene to Propylene. Journal of Physical Chemistry B 1998, 102 (1), 167–173.

(51) Wang, D.; Lunsford, J. H.; Rosynek, M. P. Catalytic Conversion of Methane to Benzene over Mo/ZSM-5. Top Catal 1996, 3 (3–4), 289–297.

(52) Wu, M.-C.; Truong, C. M.; Coulter, K.; Goodman, D. W. Role of F Centers in the Oxidative Coupling of Methane to Ethane over Li-Promoted MgO Catalysts. J Am Chem Soc 1992, 114 (19), 7565–7567.

(53) Alfke, G.; Irion, W. W.; Neuwirth, O. S. Oil Refining. In Ullmann's Encyclopedia of Industrial Chemistry; John Wiley & Sons, Ltd, 2007.

Chapter 5. Perspective

The scientific challenge of simultaneous methane upgrading with other greenhouse gases is accelerating the study of alternative oxidant-assisted OCM, like CO_2- and N_2O-OCM, which have been studied here. Most articles on this subject were published prior to the year 2000 and the rise of modern materials characterization techniques. Many of such articles focus on catalyst discovery and evaluation of previously unused materials for these reactions but lack characterization results that could elucidate identifying information of active site structure.

We were motivated by this gap in knowledge to provide a detailed characterization of a catalyst system that had demonstrated remarkable methane coupling selectivity. The published work of Chapter 2 sought to characterize the Ca site structures of Ca/ZnO catalysts over a range of Ca composition and correlate the structure to catalyst performance. However, there were many challenges to characterize the low-Ca-loading catalysts. The Ca species were too dispersed to be observed with XRD. Low Z-contrast between Ca and Zn, along with high dispersion, made imaging of Ca with electron microscopy not possible. However, results from a suite of techniques – TEM, XRD, XPS, L-edge XANES, and CO_2-IR-TPD as described in Chapters 1 and 2 – corroborated that the Ca sites on catalysts with < 2 mol% Ca were highly dispersed on ZnO, leading to a higher population of Ca-ZnO interface sites with unique electronic and geometric properties that enhanced the CO_2-assisted methane coupling performance.

The work of Chapter 3 confirms the high degree of Ca dispersion. The complementary theoretical XANES simulations provided critical evidence to determine the specific Ca site structures. It was found that the Ca sites exist as ultra-small one- or two-dimensional linear or planar oxide clusters. A pre-edge feature unique to the low-Ca-loading catalysts was determined to arise from the Ca 1s to 4p electronic transition of under-coordinated Ca surface atoms. With a better understanding of the Ca site structure, we can now learn specifically how changes in this site influence methane coupling reactivity.

At the same time, the Ca/ZnO catalysts and other similar materials were also evaluated for their catalytic potential to upgrade light hydrocarbons in similar reactions, like OCM and ethane

dehydrogenation. The effect of reaction conditions, such as temperature and reactant composition, of CO_2-OCM, N_2O-OCM, and OCM on reaction kinetics and product distribution was measured over a wide range of conditions and catalyst materials. Physical properties of the Ca/ZnO catalysts – composition of the support oxide, Ca dispersion, ZnO morphology – were varied by varying the synthesis method, and the influence of these properties on CO_2-OCM performance was studied. This work is summarized in Chapter 4. These experiments provide preliminary data that have potential to inspire future studies of soft-oxidant assisted methane coupling catalyst properties and reaction conditions.

The field of soft-oxidant assisted methane coupling is still young, relative to OCM. There are many avenues of exploration into mechanism determination and the influence of active site structure on reaction kinetics worth studying. The work in this dissertation took a first step into answering these research questions and aimed to revive interest in this field to address both environmental and energy concerns.